Validation of HOAPS latent heat fluxes against parameterizations applied to *RV Polarstern* data for 1995-1997

Master-Arbeit

im **Masterstudiengang (M.Sc.) Climate Physics**

der Mathematisch-Naturwissenschaftlichen Fakultät

der Christian-Albrechts-Universität zu Kiel

vorgelegt von

Julian Kinzel

(838010)

Erstgutachter: Prof. Dr. Douglas Maraun

Zweitgutachter: Dr. rer. nat. Karl Bumke

Kiel, im Juli 2013

Abstract

Latent heat fluxes (LHF) represent a crucial component of the global energy cycle, as they, next to sensible heat fluxes (SHF), compensate for the imbalance between incoming and outgoing radiation fluxes. As LHF provide one of the upper boundary conditions for the oceanic component of coupled atmosphere-ocean circulation models, it is desirable to rely on one consistent LHF data source with sufficient spatial and temporal resolution to reduce inaccuracies within the models' boundary conditions and hence their output. Remotely sensed LHF, particularly the Hamburg Ocean Atmosphere Parameters and Fluxes from Satellite Data (*HOAPS*) climatology, are considered to fulfil this criterion, as they provide long-term records of accurate flux estimates with adequate spatial detail. However, the validity of HOAPS LHF needs to be investigated to identify strengths and weaknesses and thus assess its potential of reliably representing an essential part of the global freshwater cycle.

Within this study, a validation of HOAPS-3.0 - based LHF at pixel-level resolution between 1995-1997 is performed over the Atlantic basin, comprising $78°$S - $82°$N. A recently at Geomar (Kiel) developed aerodynamic bulk flux algorithm termed Oceanet is applied to hourly bulk measurements obtained during 19 Atlantic cruises of *RV Polarstern*. Its LHF output serves as the in-situ validation data source, which is supplemented by ERA-Interim reanalysis data. By means of the nearest-neighbour approach, a collocation of HOAPS- to Oceanet- and ERA-Interim data is carried out, constrained by temporal and spatial threshold shifts of three hours and 60 km, respectively.

Bias analyses suggest that HOAPS LHF are on average significantly underestimated compared to Oceanet and ERA-Interim ($-8\ W/m^2$, -12%), confirming previous findings. A sub-division into latitudinal bands resolves absolute biases exceeding $-20\ W/m^2$ (-21%, Oceanet) and $-25\ W/m^2$ (-26%, ERA-Interim) within the tropics.

Investigations of bulk input parameters directly impacting LHF, namely wind speeds $\vec{u}$ and sea-air specific humidity differences $q_s - q_a$, reveal that the observed negative LHF biases within the HOAPS record are mainly associated with an overrepresentation of q_a and hence a negative bias of $q_s - q_a$ ($20°$S - $60°$N). Latitudinal averages identify q_a biases exceeding $1\ g/kg$ within the subtropical northern hemisphere. To the contrary, misrepresentations of $\vec{u}$ among HOAPS in comparison to the validation data sources exhibit less priority. Southern hemispheric extratropics represent an exception, in as much as positive LHF biases are associated with a concurrent overestimation of HOAPS-based $\vec{u}$.

As the minor differences between the HOAPS- and Oceanet-based transfer coefficients C_e lie within the uncertainty range inherent to bulk flux parameterizations, it is suggested that the significant LHF deviations for the most part arise from deviations among the bulk input variables. Away from coastal waters, where especially $\vec{u}$ is fraught with uncertainty, it is presumed that HOAPS-based surface air temperature (SAT) estimates largely contribute to this deficiency, as relative humidities and air-sea temperature differences are prescribed to be 80% and 1K, respectively, which may represent an area-wide tropical bias source.

Zusammenfassung

Latente Wärmeflüsse (LHF) stellen eine entscheidende Komponente im globalen Energiekreislauf dar, da sie neben sensiblen Wärmeflüssen (SHF) einen Großteil des Ungleichgewichts zwischen kurz- und langwelligen Strahlungsflüssen kompensieren. Als eine Randbedingung der Ozeankomponente gekoppelter Klimamodelle ist es wünschenswert, sich auf einen einheitlichen LHF Datensatz mit hinreichender räumlicher und zeitlicher Auflösung stützen zu können und somit Ungenauigkeiten der Randbedingungen und folglich der Modellergebnisse zu minimieren. Fernerkundungsbasierte LHF, insbesondere die der 'Hamburg Ocean Atmosphere Parameters and Fluxes from Satellite Data' (*HOAPS*) Klimatologie, erfüllen diese Voraussetzung, da sie zeitlich hochaufgelöst sind und das Potential besitzen, präzise Langzeitaufnahmen globaler Flüsse zu liefern. Dennoch ist eine Validierung der HOAPS LHF notwendig, um sowohl Stärken als auch Schwächen des Datensatzes aufzuzeigen und somit dessen Leistungsvermögen einzuschätzen, einen essenziellen Bestandteil des globalen Frischwasserzyklus' zuverlässig zu beobachten.

In dieser Arbeit werden die auf Pixel-Ebene aufgelösten HOAPS-3.0 LHF zwischen 1995-1997 über dem Atlantik ($78°$S - $82°$N) validiert. Als Validierungsdatenquelle dient zum einen ein stündlich aufgelöster, 19 Fahrten der *FS Polarstern* umfassender LHF Datensatz, der auf einer kürzlich am Geomar (Kiel) entwickelten Flussparameterisierung (Oceanet) basiert. Zum anderen dienen ERA-Interim Reanalysedaten als weitere Validierungsbasis. Die ausgeführte Kollokierung der HOAPS-, Oceanet- und ERA-Interim DatensÃtze basiert auf einer maximalen zeitlichen und räumlichen Verschiebung von drei Stunden bzw. 60 km.

Analysen der systematischen Abweichungen deuten auf eine signifikante Unterschätzung der HOAPS LHF im Vergleich zu Oceanet und ERA Interim hin ($-8\ W/m^2$, -12%), was die Ergebnisse früherer Studien bestätigt. Eine Unterteilung in Breitengradzonen zeigt absolute Abweichungen in den Tropen, die $-20\ W/m^2$ (-21%, Oceanet) bzw. $-25\ W/m^2$ (-26%, ERA-Interim) überschreiten.

Untersuchungen der die LHF beeinflussenden meteorologischen Eingabeparameter, d.h. Windgeschwindigkeiten ($\vec{u}$) und Differenzen der spezifischen Feuchten zwischen Ozean / Atmosphäre ($q_s - q_a$) deuten auf signifikante positive q_a Anomalien und folglich negative $q_s - q_a$ Anomalien als Ursache der negativen HOAPS LHF Abweichungen hin ($20°$S - $60°$N). Diese Anomalien überschreiten in den nördlichen Subtropen $1\ g/kg$. Im Gegensatz dazu spielen Abweichungen von $\vec{u}$ eine untergeordnete Rolle in der Analyse der systematischen Abweichungen. Die mittleren Breiten der Südhemisphäre stellen insofern eine Ausnahme dar, als dass positive HOAPS LHF Anomalien mit gleichzeitig erhöhten HOAPS $\vec{u}$ einhergehen.

Da der minimale Unterschied der HOAPS- und Oceanet basierenden Austauschkoeffizienten C_e im Unsicherheitsbereich der zugrundeliegenden Parameterisierungen liegt, sind die signifikanten HOAPS LHF Abweichungen größtenteils auf die Unterschiede der meteorologischen Eingangsparameter zurückzuführen. Abseits der Küste, wo insbesondere $\vec{u}$ fehlerbehaftet ist, sind möglicherweise die HOAPS Oberflächentemperaturen (SAT) für einen entscheidenden Teil der in den Tropen beobachteten LHF Differenzen verantwortlich, da die zugrundeliegenden relativen Feuchten und Temperaturdifferenzen

zwischen Ozean / Atmosphäre mit 80% bzw. 1K als konstant angenommen werden.

Contents

1 Introduction and Motivation

The heat transfer between ocean and atmosphere consists of four flux components, namely short-wave- and long-wave radiation (radiative fluxes SWR and LWR) as well as sensible- and latent heat fluxes (turbulent fluxes SHF and LHF) (*Bourras* (2006)). Whereas the first element transfers heat from the atmosphere to the ocean, the latter three contribute to the energy exchange from the ocean to the atmosphere, as is illustrated by the annual mean global energy budget in *Fig. 1.1*. As LHF (part of 'Evapotranspiration' in *Fig. 1.1*) and SHF ('Thermals' in *Fig. 1.1*) act as the primary connections between both fluids on all scales, compensating for energy losses due to radiation fluxes (*Schulz et al.* (1997)), both play a key role in impacting short- and long-term variability of the ocean-atmosphere- and thus of the climate system (*Chang and Grossman* (1999)).

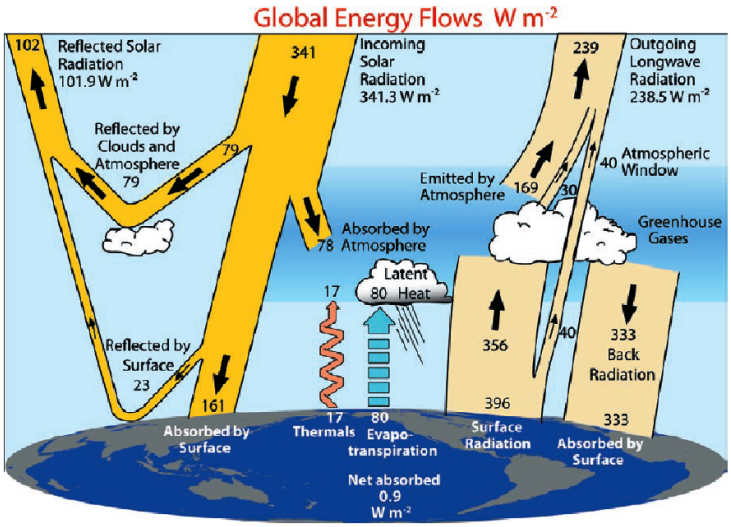

Fig. 1.1: Global annual mean Earth's energy budget $[W/m^2]$ for the period between 03 / 2000 to 05 / 2004. The broad arrows indicate the schematic flow of energy in proportion to their importance. 'Incoming Solar Radiation' and 'Outgoing Longwave Radiation' correspond to SWR and LWR in the text, respectively. Adapted from *Trenberth et al.* (2009).

Owing to its large amplitude in comparison to SHF, LHF considerably influences the oceanic heat budget and thus represents a vital source in terms of altering the atmospheric circulation and the overall hydrological cycle (*Schulz et al.* (1997), *Chou et al.* (2004)). As its spatial as well as interannual / seasonal LHF variability is extensive (*Chou et al.* (2004)), the accurate representation of LHF within the energy redistributing process cannot be overstressed.

The prominent role inherent to LHF in context of global climate finds expression in coupled atmosphere-ocean general circulation models (AOGCM's), in as much as they serve as upper boundary conditions (BC) for the OGCM component (*Zeng et al.* (1998)). As LHF, along with both SHF and momentum fluxes, act to alter sea surface temperatures (SST) (*Liu et al.* (2011)), serving as the lower BC for the AGCM, the improvement of model output crucially depends on the accuracy of LHF representation (*Zeng et al.* (1998), *Chou et al.* (2003)). Biased LHF, which ultimately affect global evaporation estimates[1], distort the hydrological balance inherent to the climate system, which triggers shifts of both atmospheric and oceanic circulation[2].

[1] $\approx$ 86% of global evaporation occurs over the global ocean basins (*Baumgartner and Reichel* (1977)).

[2] Wrong evaporation estimates alter oceanic salinity budgets and thus execute direct impact on the strength of the thermohaline circulation.

Numerous studies have underpinned the importance of measuring surface LHF as well as their changes to improve the understanding of the coupled climate system and feedbacks therein (*Curry et al.* (2004)). Amongst others, these coupled interactions include uncertainties associated with the implemented cloud physics (*Kubota et al.* (2003)). The uncertainties are directly linked to vertical humidity exchanges and thus LHF (*Bourras* (2006)), which highlights the necessity to accurately quantify the interfacial LHF.

Liu et al. (2011) stress the significance of not only detecting, but also simulating variability inherent to the coupled system. According to the authors, decoding resulting biases as to their origin could considerably improve coupled GCM's and hence embedded energy cycles.

Three techniques exist to derive in-situ LHF estimates over global oceans. On the one hand, the direct eddy correlation (EC) method may be applied (e.g. *Foken* (2008)). Here, high-frequency measurements of wind speed and atmospheric scalar properties such as temperature are analyzed by means of sonic anemometers, which allow for determining the three-dimensional air flow at rates of up to 20Hz by means of three non-orthogonal axes. In addition, LI-COR gas analyzers[3] allow for concurrent high-frequency specific humidity recordings. Hence, the EC technique enables the precise determination of $\overline{w'x'}$ (as part of the LHF calculation, compare *Eq. 7* in *Section 3.1.3*), where the primes indicate deviations of the temporal mean, w represents the vertical velocity, and x may be replaced by temperature T or specific humidity q. However, several issues have to be accounted for during data processing, which comprise flow distortion effects (associated with the mounting brackets), contamination due to sea spray, and the correction of ship motion due to swell. *Wyngaard and Coté* (1990) recall the elevated sampling uncertainty in light wind regimes, contributing to the inherence of noise within the EC raw data.

On the other hand, the (indirect) inertial dissipation (ID) technique represents an additional approach to derive LHF estimates, utilising characteristics of the inertial subrange of atmospheric velocity and scalar turbulence spectra. A detailed description of the ID methodology is provided in *Edson et al.* (1991). Although its application has several advantages compared to the EC approach (to name but one, it is rather insensitive to the sensor orientation), *Grachev and Fairall* (1997) have demonstrated issues during strong swell, associated with the compulsive assumption of positive momentum fluxes. Considerable deviations among LHF estimates originating from the EC / ID method have been exposed by *Drennan et al.* (1999) during rough seas.

Aerodynamic bulk flux algorithms serve as an alternative third approach to yield in-situ LHF indirectly. Given the constraint of direct observations being technologically demanding and thus costly, these algorithms rely on bulk formulations, which parameterize LHF in terms of observed mean quantities (bulk variables) (e.g. *Fairall et al.* (2003), *Bentamy et al.* (2003)). The latter primarily comprise near-surface wind speed and -specific humidity ($\vec{u}$ and q_a, respectively) as well as SST. A variety of LHF bulk algorithms have been published to date, each of which are predicated on differing oceanic

[3] e.g. *http://www.licor.com*.

regimes and incorporate diverging parameterizations. Several studies have focused on the significant biases inherent to the different code versions (*Zeng et al.* (1998), *Brunke and Zeng* (2002), amongst others), which are in part owing to extremes of wind speed ranges (e.g. *Webster and Lukas* (1992), *Chang and Grossman* (1999)). However, a consensus has somewhat been reached among the scientific community that the COARE3.0 algorithm (*Fairall et al.* (2003), see *Section 3.1.2*) is least problematic in comparison to various other LHF parameterizations (e.g. *Brunke and Zeng* (2002)). Although this conclusion is debatable (as shown in *Bourras* (2006)), the COARE3.0 bulk flux algorithm was established involving several extratropical cruise legs (in contrast to most other, rather tropical codes), suggesting its applicability in a wide range of atmospheric and oceanic boundary conditions.

However, owing to large spatial and interannual variability as well as spatial and temporal undersampling, *Andersson et al.* (2011) elucidate that in-situ LHF measurements remain troublesome over the global oceans. Although the Comprehensive Ocean-Atmosphere Data Set (COADS, *Woodruff* (1987)) has collected the most extensive surface marine observation data base since 1854, serious issues associated with temporal / spatial coverage and uncertainty have been subject to discussion (*da Silva et al.* (1994)).

To a greater degree, confidable long-term global LHF datasets are of need to overcome these issues (*Chou et al.* (2004)), serving as a verification source for coupled AOGCM's (*Schulz et al.* (1997)).

Despite being long and homogeneous, *Winterfeldt et al.* (2010) point out that global atmospheric reanalyses do not fulfil the desired criteria either, owing to a lack of spatial detail. This especially applies to remote regimes of the Southern Ocean, where assimilated observational data remains scarce.

In order to overcome the insufficient spatial and temporal coverage by ships and buoys over the ocean as well as shortcomings of reanalysis products, high-quality remote sensing techniques are of supplementary need.

The benefits resulting from surface flux estimates based on satellite observations have been first recognized within the 1980's. *Graßl et al.* (2000) and *Bentamy et al.* (2003), for example, highlight the potential of deriving relevant LHF bulk parameters via satellite retrievals with nearly global coverage, which eventually contributes to climate analysis, its variation, and the forecasting and monitoring of the hydrological cycle (*Grima et al.* (1999), *Andersson et al.* (2011)). *Bourras* (2006) conclude as well that space-borne measurements represent a promising technique in this context.

Several remotely sensed data products exist to date, which have been subject to intercomparison studies. Amongst others, these comprise the Goddard Satellite-based Surface Turbulent Fluxes (GSSTF) data set, the Japanese Ocean Flux Dataset (J-OFURO), the objectively analyzed air-sea fluxes (OAflux) as well as the flux dataset compiled by the Institut Français de Recherche pour l'Exploration de la Mer (IFREMER). Most of the listed data sources share the constraint of long-term inhomogeneity, in as much as contributing bulk parameters, on which LHF depends, partially originate from different instruments, which eventually introduces cross calibration uncertainties (*Andersson et al.* (2011)).

This issue does not apply to the 1987 initiated Hamburg Ocean Atmosphere Parameters and Fluxes from Satellite (HOAPS) dataset (*Andersson et al.* (2010)), as, apart from SST, the final LHF output solely relies on SSM/I measurements (Special Sensor Microwave/Imager Radiometers, compare *Section 2.2.1*). This allows for deriving the parameters, on which global ocean surface freshwater flux components crucially depend, consistently within one entirely satellite-based dataset (*Andersson et al.* (2011)).

The implementation of the HOAPS climatology has been tested among numerous intercomparison studies (*Kubota et al.* (2003) and *Winterfeldt et al.* (2010)). *Bourras* (2006) concludes that compared to three other satellited-based LHF outputs[4], HOAPS-2[5] is the most appropriate product to study turbulent fluxes over global oceans. Promising results have also been published within *Klepp et al.* (2008) and *Andersson et al.* (2011).

The vast potential of monitoring global LHF estimates relying on space-borne instruments serves as a motivation for the underlying work to validate a revised version of the encouraging HOAPS dataset, namely HOAPS-3 (*Andersson et al.* (2010)), the LHF estimates of which are based on the COARE3.0 bulk flux algorithm (*Fairall et al.* (2003), *Section 3.1.2*).

Whereas virtually all published validation studies involving HOAPS to date evaluate its performance by means of monthly or annual climatologies, the underlying study focuses on HOAPS data resolved in pixel-level resolution (compare *Section 2.2.1*). This approach permits the assessment of the HOAPS dataset's performance in a temporally and spatially local sense, which constitutes a fundamental basis among case studies involving HOAPS data.

In-situ- and reanalysis data will play a central role as validation data sources within the investigation period comprising 1995-1997. Whereas the former encompasses a multi-year observational time series obtained on *RV Polarstern* among 19 Atlantic cruises, the latter is represented by the ERA-Interim reanalysis product (*Dee et al.* (2011)). Both validation data sources aim to reveal strengths and weaknesses underlying the HOAPS data record and thus allow for assessing its acceptation in context of future studies focusing on global energy- and -flux budgets.

The validation procedure of HOAPS-based LHF within this work is structured as follows. Subsequent to an illustration of the Atlantic surface LHF climatology (*Section 1.1*), *Section 2* is dedicated to the introduction of the contributing data sets. The applied methodology is presented in *Section 3*, which allows for the statistical confrontation of HOAPS- and ship-based-/ ERA-Interim LHF output. Underlying bulk flux algorithms are introduced and respective deviations among the datasets are highlighted. Whereas *Section 4* incorporates the objective presentation of the validation results and focuses on the individual underlying bulk flux parameters, *Section 5* establishes a link to earlier

[4]GSSTF-2, J-OFURO, and BEL (Bourras-Eymard-Liu dataset).

[5]Electronic publication, available via *urn:nbn:de:tib-10.1594/WDCC/HOAPS2_PENTAD8*, e.g.

investigations and presents numerous explanations for essential observations made within *Section 4*. The underlying work is wound up among conclusions drawn in *Section 6*.

1.1 Climatology of Atlantic Surface LHF

Fig. 1.2 illustrates annual Atlantic LHF averages based on an interpolated version of the Comprehensive Ocean Atmosphere Data Set (COADS, *Woodruff* (1987), compare *Lindau* (2001)). It reveals that zonal-mean LHF maximise over the so-called 'oceanic deserts' around $15°$ N/S (trade wind regions). These maxima arise from high wind speeds coupled to large air-sea humidity differences (*Chou et al.* (2004)) and are more pronounced within the western part of the basin, owing to elevated SST. Their occurrence is more distinct on the respective winter hemispheres (*Yu et al.* (2011)) (not shown), which can be attributed to stronger prevailing wind speeds.

On average, LHF remain comparatively small over the equatorial oceans due to both weaker winds in the western part as well as damped SST in the eastern part related to equatorial upwelling (*Kubota et al.* (2003), *Chou et al.* (2004)). A regionally confined basin-scale hotspot of LHF exceeding absolute LHF of $200\ W/m^2$ is evident along the northern hemispheric western boundary current (especially during winter, not shown), associated with the warm oceanic currents of the Gulf Stream. Annual means of LHF in high latitudes remain small (below $50\ W/m^2$, according to amount) due to a poleward decrease of SST (*Chou et al.* (2004)) and the Clausius Clapeyron relation, linking temperature to maximal moisture contents.

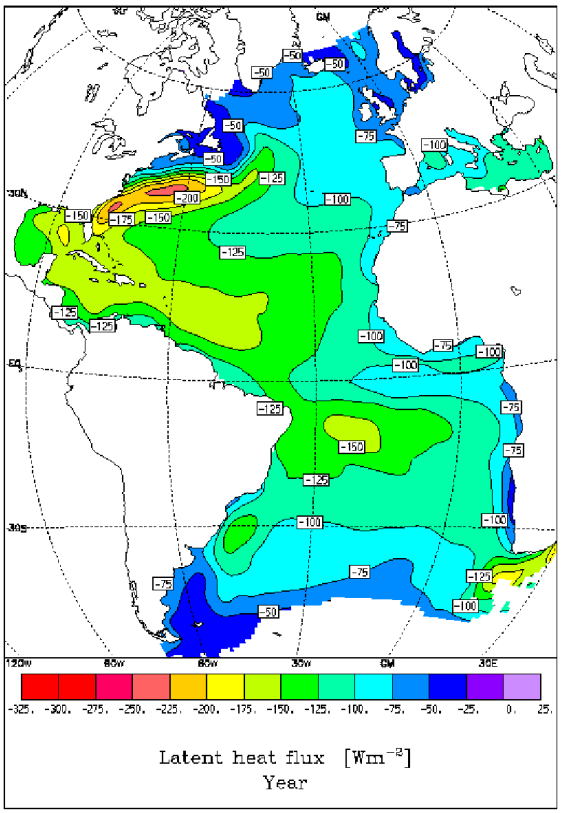

Fig. 1.2: Annual mean LHF over the Atlantic basin, derived from the Comprehensive Ocean Atmosphere Data Set (COADS). Negative fluxes represent an energy exchange from the ocean to the atmosphere. Monthly climatologies, which also incorporate further meteorological bulk parameters, can be obtained from *Lindau* (2001). Adapted from *Lindau* (2001).

A focus on southern hemispheric latitudes reveals a zonally broken symmetry in mid-latitudes, comparable to $40°$N. Largest LHF exceeding absolute values of $150\ W/m^2$ (and substantially higher values during late austral spring, not shown) are evident south of South Africa, where the warm Agulhas Current propagates (*Yu et al.* (2011)). On the contrary, small values are observed along the Antarctic continent, where SST remain low. The damped LHF along the coast of Argentina can be brought in connection with the cold Falkland current, which constitutes a branch of the Antarctic Circumpolar Current in the southern hemisphere, flowing northward along the east coast of Argentina to latitudes of $30° - 40°$S. Furthermore, a confined region of LHF maxima is resolved off Uruguay, associated

with the west Brazil-Malvinas confluence (*Liu et al.* (2011)). The latter peaks in late austral autumn (not shown) and represents a convergence region between $35^\circ - 45^\circ$S / $50^\circ - 70^\circ$W of the warm, poleward flowing Brazil Current and the cold, equatorward Falkland Current.

2 Data Sources and Data Processing

2.1 *RV Polarstern* In-Situ Data

Meteorological - and bulk-SST data of 19 cruises completed by *RV Polarstern* between 1995-05-01 and 1998-11-01 was downloaded from the PANGAEA database[6], allowing for a compilation of a multi-year in-situ dataset.

Cruise campaign, geographical area of focus, cruise dates as well as references to respective cruise reports are listed in *Table 1*.

As the focus of the present work lies on the Atlantic basin, data collected east of 35°E and north of 82°N is not further considered. *Fig. 2.1* illustrates the contributing cruise tracks of *RV Polarstern*. Highest cruise track densities are evidently located in the (sub-)polar regions of both hemispheres, whereas fewer measurements were obtained along the transit cruise tracks connecting Bremerhaven (Germany (GER), 53.54°N / 8.57°E) and Punta Arenas (Chile (CHI), 53.15°S / 70.92°W) / Cape Town (South Africa (RSA), 33.92°S / 18.42°E), respectively.

Continuous meteorological as well as oceanographic cruise data is provided in a ten-minute resolution, allowing for a time series comprising more than 133000 measurements in time within the period of investigation (at best for each parameter). Several of the geophysical parameters were extracted for further investigation and are shown in *Table 2*.

In case one or more of these variables was not measured at a given time, all other parameters among this time step are not considered in the proceeding analysis in order to avoid interpolation errors. This case repeatedly occurred in the polar regions of both hemispheres in connection with sampling difficulties in high-latitudinal extreme environmental conditions. Amongst others, this concerned lacks of SST measurements due to frequent sea ice abundances. Owing to the comprehensive data availability, this generous approach is justifiable.

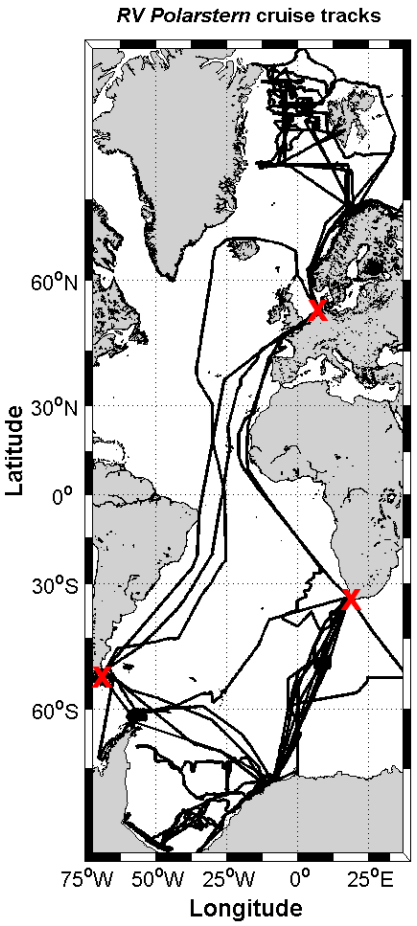

Fig. 2.1: Map of Atlantic sector showing the cruise tracks (black lines) of the *RV Polarstern* expeditions contributing to the present study (compare *Table 1*). Data obtained east of 35°E are omitted in order to restrict the subsequent analysis to the Atlantic basin. The red crosses indicate the locations of the transit cruise harbours (see text).

[6]PANGAEA represents an information system operated as an open access library, focusing on archiving, publishing, and distributing georeferenced data from earth system research. It is hosted by the Alfred Wegener Institute of Polar- and Marine Research (AWI), Bremerhaven, Germany.

As the only directly measured humidity parameter is given by the relative humidity (RH), ten-minute means of atmospheric specific humidities q_a were calculated following *Magnus* (1844):

$$q_{a,27m}\ \ [g/kg] = \frac{622 \cdot \left(c_1 \cdot exp\left(\frac{c_2 \cdot T_{27m}}{c_3 + T_{27m}}\right)\right)}{SLP_{27m}} \tag{1}$$

where T refers to the air temperature [$^{\circ}C$] and c_1,c_2, and c_3 are temperature-dependent coefficients, following an approach by *Buck* (1981)[7]. The subscripts indicate the height above sea level (ASL) [m], where the respective parameter was obtained. Specifically, SLP_{27m} denotes the correction of the sea level pressure (SLP) [hPa] to the pressure at sensor height, assuming a linear vertical pressure decrease of 1hPa / 8m. Within the lower troposphere, the latter assumption introduces negligible errors. A more accurate version of *Eq. 1* includes a correction term within the denominator ($-0.378e$), where e corresponds to the vapor pressure (e.g. *Singh and Singh* (2001)), the magnitude of which is considered as irrelevant in context of the q_a determination and is thus neglected here.

Additionally, the sea surface saturation specific humidity q_s was calculated from SLP and T at sensor height. *Kraus and Businger* (1994) demonstrate the relationship of surface saturated humidity over saline water ($q_s(S, SST)$) to that over freshwater (q_s) as a function of salinity S and SST:

$$\frac{q_s(S, SST)}{q_s(SST)} \approx 1 - 0.527 \cdot S. \tag{2}$$

Owing to the salinity dependence, a reduction of q_s of 2% over ocean water occurs for an average of $S = 0.035$. Minor biases associated with salinity variabilities within the Atlantic basin, especially in polar waters, are considered as negligible. Owing to this simplification, q_s is derived following

$$q_s\ \ [g/kg] = 0.98 \cdot 622 \cdot \frac{e_w(SST)}{SLP_{27m} - 0.378 \cdot e_w(SST)}, \tag{3}$$

where e_w depicts the saturation vapor pressure at the sea surface. As SST is not obtained at the direct interface, one refers to the bulk-SST [5m] in a first step, whereupon a continuous adjustment of SST and thus q_s to the interfacial value is performed throughout the bulk flux algorithm iteration (see *Section 3.1.3*).

Owing to the absence of incident longwave radiation measurements on *RV Polarstern*, which alters the net longwave radiation and thus the total heat input into the ocean, it was extracted from the ERA-Interim Reanalysis Archive (see *Section 2.3*) to also serve as an input to the bulk flux algorithms described in *Section 3.1.3 / 3.1.5*.

As the bulk aerodynamic flux codes are designed for one-hour means of bulk measurements, 60-minute arithmetic means of the parameters listed in *Table 2* as well as q_s and $q_{a,27m}$ were calculated.

[7]Numerous coefficients of c_1, c_2, and c_3 are used in literature. *Buck* (1981) demonstrates that his coefficients exhibit the greatest minimum accuracies of $\leq 0.06\%$ of q_a for meteorologically interesting temperature regimes of -80 °C - $+50$ °C when compared to other conventional approaches. For the underlying work, $c_1 = 6.1121$, $c_2 = 17.368$, and $c_3 = 238.88$ (0 °C$\leq$ T< +50 °C) or $c_2 = 17.966$ and $c_3 = 247.15$ (-40 °C$\leq$ T< 0°C) are used.

In case the averaging process involved merely $\leq$5 ten-minute observations within one hour, the hourly mean was rejected from further analysis to minimize errors associated with temporal interpolation.

Overall, 11458 hourly means of relevant geophysical parameters remain as a robust in-situ measurement basis, embodying a comprehensive data input to the bulk flux algorithms introduced in *Section 3.1.3* / *Section 3.1.5*.

Campaign	Area	Cruise Start / End	Cruise Report
ANT-XII/3	Weddell Sea	1995-01-05 / 1995-03-20	*Jokat and Oerter* (1997)
ANT-XII/5	Atlantic transit cruise	1995-05-15 / 1995-06-12	n.a.
ARK-XI/1∗	Laptev Sea	1995-07-07 / 1995-09-20	*Rachor* (1997)
ARK-XI/2	Greenland Sea	1995-09-21 / 1995-10-30	*Krause* (1996)
ANT-XIII/1	Atlantic transit cruise	1995-11-09 / 1995-12-03	*Bathmann et al.* (1997)
ANT-XIII/2	Weddell Sea	1995-12-04 / 1996-01-25	*Bathmann et al.* (1997)
ANT-XIII/3	Eastern Weddell Sea	1996-01-26 / 1996-03-16	*Arntz and Gutt* (1997)
ANT-XIII/4∗	South Atlantic	1996-03-17 / 1996-05-19	*Fahrbach and Gerdes* (1997)
ANT-XIII/5	Atlantic transit cruise	1996-05-19 / 1996-06-21	*Fahrbach and Gerdes* (1997)
ARK-XII∗	Arctic Ocean	1996-07-12 / 1996-09-23	*Augstein* (1997)
ANT-XIV/1	Atlantic transit cruise	1996-10-05 / 1996-11-09	n.a.
ANT-XIV/2	Antarctic Peninsula	1996-11-12 / 1997-01-01	n.a.
ANT-XIV/3	Weddell Sea	1997-01-04 / 1997-03-20	*Jokat and Oerter* (1998)
ANT-XIV/4	Atlantic transit cruise	1997-03-21 / 1997-04-26	*Fütterer* (1998)
ARK-XIII/1a	Norwegian Sea	1997-05-14 / 1997-05-24	*Spindler et al.* (1998)
ARK-XIII/1b	Norwegian Sea	1997-05-25 / 1997-06-23	*Spindler et al.* (1998)
ARK-XIII/2	Arctic Ocean	1997-06-24 / 1997-08-11	*Stein and Fahl* (1997)
ARK-XIII/3	Greenland Sea	1997-08-12 / 1997-09-30	*Krause* (1998)
ANT-XV/1	Atlantic transit cruise	1997-10-15 / 1997-11-07	n.a.
ANT-XV/2	South Sandwich Arc/ Bransfield Strait	1997-11-09 / 1998-01-12	n.a.

Table 1: Overview of *RV Polarstern* cruises contributing to an extensive in-situ dataset as one HOAPS LHF validation source. Asterisks in *Column 1* indicate that the respective cruise was subject to partial pre-processing data exclusion in order to restrict the analysis to the Atlantic basin. 'n.a.' = 'not available'. More details on the individual cruises is given in the respective cruise reports, available via *http://www.pangaea.de/PHP/CruiseReports.php?b=Polarstern.*

2.2 Hamburg Ocean Atmosphere Parameters and Fluxes from Satellite (HOAPS) Dataset

The Hamburg Ocean Atmosphere Parameters and Fluxes from Satellite (HOAPS) dataset is an entirely satellite-based climatology of precipitation, evaporation, and freshwater budget, which was initially released in July 1987 (*HOAPS-1*) and contains data up to 2008 (*HOAPS-3.2*) (*Andersson et al.* (2010)). Apart from freshwater flux components and related turbulent heat fluxes, the longwave net flux and atmospheric state variables are additionally available. The HOAPS climatology comprises 15 geophysical products, all of which offer a complete spatial coverage between $87.5°$S - $87.5°$N, considering the constraint of solely being defined over the global ice free oceans. To date, HOAPS

Parameter	Unit	Characteristics (Reference: 1995-1997)
Air Temperature	$°C$	PT100; installed in a radiation-protected housing with no artificial ventilation;
Relative Humidity	$\%$	portside: hair hygrometer (1.100000.28, Thies, GER); starboard: LiCl dewpoint sensor (3100.0000 BG, Friedrichs, GER); installed at 27 m ASL on both sides of the main mast; windward sensor values recorded.
Atmospheric Pressure	hPa	electronic barometer (SETRA B 270, Friedrichs, GER); installed 16.3 m ASL; reduced to 0 m ASL.
Wind Speed	m/s	cup anemometer (SK565, Thies, GER); wind vane (SK566, Thies, GER); installed 39 m ASL on port- and starboard side on main mast; windward sensor values recorded.
Short-wave Downward Radiation	W/m^2	artificially ventilated pyranometer (CM11, *Kipp & Zonen*, NED); installed on crow's nest. Night-time values not set to zero for offset determination.
Bulk Sea Surface Temperature (SST)	$°C$	thermosalinograph SBE 21 & SBE 38 (Seabird, USA); underway measurement at ship's bow [depth: 5m].

Table 2: Bulk meteorological and oceanographic parameters measured on *RV Polarstern*, extracted from the PANGAEA database for preparation of an in-situ validation dataset.

represents the only available compilation of both precipitation and evaporation data for estimating the freshwater flux from one consistently derived global satellite product (*Andersson et al.* (2010)).

In light of its uniqueness, the validation of the HOAPS dataset is therefore of great interest. It aims to reveal strengths and weaknesses of the compilation and thus to assess its potential of being a valuable complement to non-uniformly spread in-situ data derived from ships and buoys.

Retrieved HOAPS parameters originate from two different data sources, which are introduced in the following.

2.2.1 Special Sensor Microwave/Imager (SSM/I) Radiometers

Most HOAPS variables are derived from Special Sensor Microwave/Imager (SSM/I) instruments, i.e. passive microwave radiometers, which are installed aboard the satellites of the United States Air Force Defense Meteorological Satellite Program[8] (DMSP).

Amongst other skills, these sensors are considered to be most advanced for remotely monitoring winds, atmospheric humidity, and rainfall (*Graßl et al.* (2000)). Between 1995-1997, four satellites were in operational mode (see *Table 3*) and performed sun-synchronous polar orbits in heights of $\approx$ 830 km (*Hollinger et al.* (1987)). *Fig. 2.2* illustrates the scan geometry of the instrument.

SSM/I radiometers measure emitted and reflected thermal radiation from the Earth's surface and the atmosphere in form of upwelling microwave brightness temperatures[9] (T_B) at four different fre-

[8]The program monitors meteorological, oceanographic, and solar-terrestrial physics for the United States Department of Defense and is run by the National Oceanic and Atmospheric Association (NOAA).

[9]The brightness temperature is the effective temperature of a blackbody radiating the same amount of energy per unit area at the same wavelength as the observed body. Its precision is given by 0.01 K.

Satellite ID	Approx. Equatorial Crossing 1995 [UTC]	Operational period
DMSP F-10	10:09 / 22:09	07/1991 - 12/1996
DMSP F-11	06:25 / 18:25	01/1992 - 12/1999
DMSP F-13	05:43 / 17:43	09/1995 - 12/2008
DMSP F-14	n.a. / n.a.	06/1997 - 07/2008

Table 3: DMSP satellites in operational mode between 1995-1997. All satellites had SSM/I installed on board, which serve as a basis for the HOAPS-3.0 dataset. AM equatorial crossing times refer to the descending node (crossing the equator north to south), whereas PM times are associated with the respective ascending node (vs.vs.) (*Andersson et al.* (2010)). 'n.a.' = 'not available'.

quencies. During its orbit around the Earth, it rotates continuously about an axis parallel to the local spacecraft vertical. Whereas both horizontal and vertical polarized signals are measured at 19.35 GHz, 37.0 GHz, and 85.5 GHz, the 22.2 GHz channel only considers the vertically polarized signal (*Graßl et al.* (2000)), allowing for seven frequency channels in total.

The lowest five frequency channels are sampled during every second rotation (so-called A-scans) of the instrument. Each scan delivers 64 uniformly spaced radiometric samples ($\triangleq$ 64-pixel resolution). The remaining two 85.5 GHz channels, on the other hand, have a resolution which is twice as high, as sampling is done during A- and B-scans. A fixed cold space reflector and a reference black body hot load are applied for continuous on-board calibration.

Antenna Temperature Tapes (ATT) from Remote Sensing Systems (RSS) and Temperature Data Records (TDR) taken from the National Environmental Satellite, Data, and Information System (NESDIS) are used as SSM/I input data for HOAPS. Pre-processed versions of these include navigated and calibrated antenna temperatures, which are subsequently converted to TB's following *Wentz* (1991) (*Andersson et al.* (2010)).

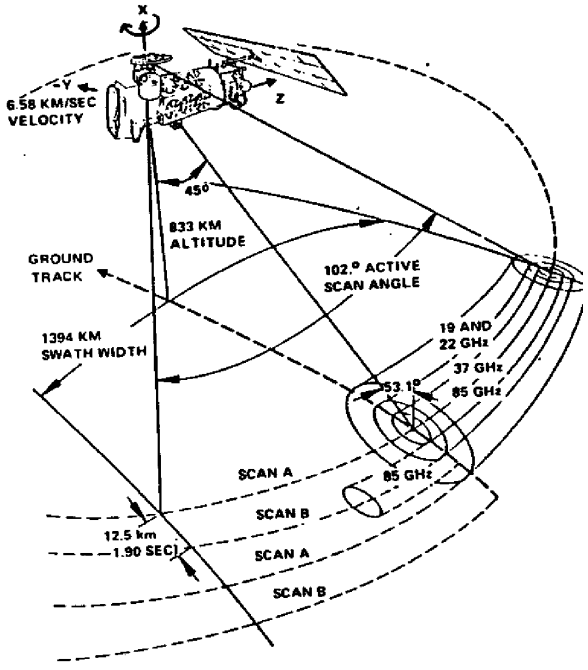

Fig. 2.2: Scan geometry of an SSM/I instrument aboard a DMSP satellite. See text for further descriptions. Adapted from *Hollinger et al.* (1987).

As illustrated in *Fig. 2.2*, the SSM/I is characterized by a conical scan pattern, where the antenna beam intersects the Earth's surface at an incidence angle of $53.1°$ and the swath width (the width of the surface area 'seen' by the instrument) spans $\approx$ 1400 km. This setup ensures a constant viewing geometry across the scan to simplify the distinction between surface and atmospheric contributions to the measurements (*Dee et al.* (2011)). Apart from an latitudinal dependence of the satellite, the

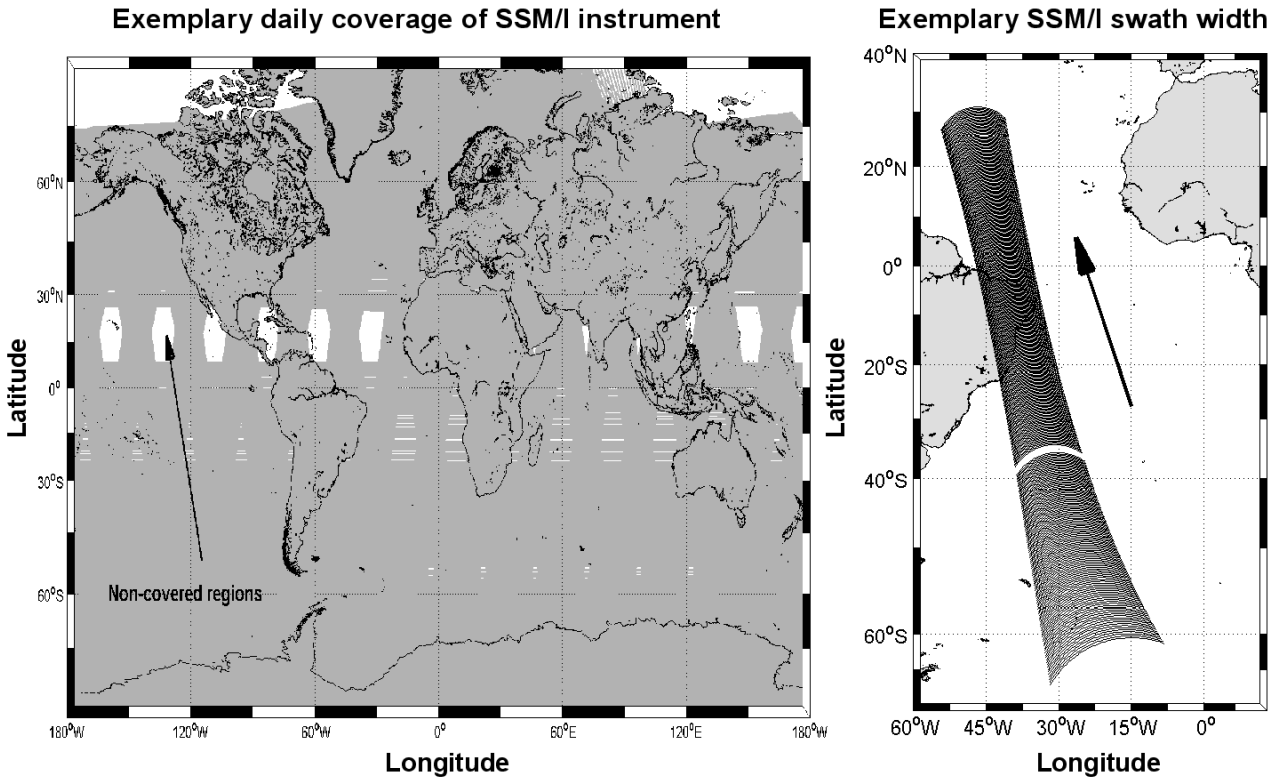

Fig. 2.3: Left: Example of the areal coverage of one SSM/I instrument mounted on top of F-10 on 1995-01-05. Geographical regions north (south) of $87.5°$N ($87.5°$S) are not covered. Gray regions indicate sampled areas, whereas white colour implies that F-10 did not scan the respective domain on that day, which tends to be restricted to the subtropics. Within a few days, those isolated regions are sampled as well, as all DMSP satellite orbits perform east-west shifts.
Right: Swath width propagation of SSM/I instrument mounted on F-10, on 1995-01-05 between 00:24 UTC and 00:50 UTC. The black arrow indicates the direction of satellite movement.

channel footprints vary with channel energy, ranging from elliptic 43x69 km^2 (cross-track / along-track) (19.35 GHz channel) to rather circular 13x15 km^2 (85.5 GHz channel).

Each instrument completes one orbit within 102 minutes, implying that $\approx$ 14 orbits per day are performed (*Andersson et al.* (2010)). This allows for 82% of global coverage between $87.5°$S - $87.5°$N within 24 hours. Remaining gaps in the subtropics are closed within a few days due to the east-west shift of the DMSP satellite orbits. As the temporal drift of equatorial crossing times of each satellite does not vary more than three hours within several years, their orbits can be considered as very stable (*Andersson et al.* (2010)). *Fig. 2.3* (left) exemplarily shows the surface coverage of one SSM/I satellite-based instrument within 24 hours, whereas *Fig. 2.3* (right) shows the concurrent spatial advance of the swath width within a time frame of ≈ 25 minutes.

HOAPS gridded data products are available in several versions, depending on whether they are applied for case studies, comparison experiments or climatological aspects. Within this work, the HOAPS-S dataset of HOAPS-3.0 (*HOAPS*, as of now) (*Andersson et al.* (2010)) is validated, which comprises all retrieved physical parameters between January 1995 and December 1997 in their original SSM/I scan-oriented pixel-level resolution (as high as $\approx$ 1 scan / 4 sec) for each satellite. *Table 4* gives an overview of the HOAPS geophysical parameters and features, which are of relevance for

this work. Respective retrieval algorithms are briefly discussed below. A more detailed discussion is supplied by *Andersson et al.* (2010) and references therein.

Parameter	**Unit**	**Data Source**	**Reference/Information to Retrieval Algorithm**
Absolute wind speed at 10m ($\vec{u}_{10m}$)	m/s	SSM/I	*Krasnopolsky et al.* (1995)
Specific Air Humidity ($q_{a,10m}$)	g/kg	SSM/I	*Bentamy et al.* (2003)
Sea Surface Saturation Specific Humidity (q_s)	g/kg	SSM/I	*Magnus* (1844)
Surface Air Temperature (SAT)	K	SSM/I	*Liu et al.* (1994)
Latent Heat Flux (LHF)	W/m^2	SSM/I	*Fairall et al.* (1996)
Sea Surface Temperature (SST)	K	AVHRR	*Casey* (2004), *Kilpatrick et al.* (2001)

Table 4: Physical parameters within HOAPS, which are used within this study. Whereas SST data is based on AVHRR measurements (compare *Section 2.2.2*), all other parameters are retrieved based on SSM/I technology. See text for brief discussions of the respective retrieval algorithms.

- **Near-surface wind speed,** $\vec{u}_{10m}$: As wind friction on the ocean alters the emissivity of its surface in the microwave spectrum, the wind speed retrieval is considered as being indirect. Surface wind speed data within HOAPS-3.0 is based on a network approach[10] (*Krasnopolsky et al.* (1995)), which links the near-surface (10 m ASL) wind speeds in a non-linear manner to SSM/I-based T_B, taking different cloud amounts into account (*Andersson et al.* (2010)). Applied to a verification dataset, the HOAPS neural network wind speed algorithm holds a low bias of $-0.02\ m/s$ and a standard deviation of $1.5\ m/s$, which can be evaluated as a considerable improvement compared to former algorithms (see e.g. *Schlüssel and Luthardt* (1991) (based on non-linear regression) and *Stogryn et al.* (1994) (developed an earlier version of neural network approach)).

- **Near-surface specific humidity (10 m ASL),** $q_{a,10m}$: Several authors have been investigating the estimation of q_a using SSM/I. *Liu* (1986), e.g, revealed a linear relationship between q_a and integrated water vapour content, the latter being inferable from SSM/I-based T_B. In this context, *Schulz et al.* (1993) provided an inverse model based on linear regression, directly relating q_a to T_B, which was upgraded by *Schlüssel et al.* (1995).

  Specific humidity data incorporated in HOAPS is based on a study by *Bentamy et al.* (2003), who apply a modified version (in terms of adjusted regression coefficients) of the Schulz Model on the basis of a training dataset of collocated ship-based ($\hat{=}$ observed) and satellite-based ($\hat{=}$ remotely sensed) q_a obtained between 1996 and 1997. An average bias reduction of 15% and a mean squared error of $1.4\ g/kg$ was registered. Despite model improvements, biases of up to $0.25\ g/kg$ over the North Atlantic remain during summer, associated with large absolute

[10]These types of networks act as nonlinear data-driven approaches, which are capable of modelling relationships between input (T_B) and output (near-surface wind) without the need of an a-priori relationship between both. More details on the neural network methodology may be taken from *Krasnopolsky et al.* (1995).

specific humidities (*Andersson et al.* (2010)).

- **Sea surface saturation specific humidity,** q_s: Applying the Magnus Formula (*Magnus* (1844)), the saturation specific humidity at the sea surface may be derived. To account for the salinity effect within the HOAPS data record, the output is scaled with a factor of 0.98 (compare *Eq. 3*).

- **Surface air temperature**, SAT: As a direct measurement of SAT is not possible, the latter is estimated from satellite-based SST- and q_a measurements. HOAPS SAT are derived following *Liu et al.* (1994), a constant RH of 80%[11] is assumed for the satellite-derived q_a, arguing that introduced errors during strongly stable atmospheric boundary layer conditions are second-rank in context of latent heat flux derivations. Additionally, a constant temperature difference of 1K between sea surface and surface air is presumed (*Wells and King-Hele* (1990)).

- **Latent heat flux**, LHF: The LHF within HOAPS is parameterized applying the COARE2.6a bulk flux algorithm (*Bradley et al.* (2000)). Apart from minor modifications associated with SST cool skin and warm layer physics, which are not embedded in the HOAPS data product, it corresponds to the version COARE3.0 (*Fairall et al.* (2003), compare updated algorithm description in Section *3.1.3*). Most input parameters to the bulk flux algorithm originate from SSM/I measurements. Exceptions apply to SAT, transfer coefficients C_e as well as SST (see *Section 2.2.2*)).

2.2.2 Advanced Very High Resolution Radiometers (AVHRR's)

It is well-known that space-based multichannel infrared radiometers operating in cloud-free conditions provide the most reliable global SST datasets (e.g. *Barton* (1995)).

Since 1981, the Advanced Very High Resolution Radiometers (AVHRR's) are flown on board of four polar-orbiting NOAA satellites in altitudes ranging between 830-870 km (*Kilpatrick et al.* (2001), compare *Table 5*) and measure SST in the infrared (IR) range within three channels. As longwave radiation emitted from the surface is partially damped by the atmosphere before reaching the satellite sensor, a multichannel setup is necessary with channels located between $3.5 - 3.9\ \mu m$ and $10.0 - 12.5\ \mu m$. Within these ranges, the ocean surface exhibits a high emissivity and SST can thus be accurately estimated in cloud-free cases.

To exclusively rely on satellite data for the computation of the HOAPS-3.0-based LHF, SST data is extracted from the Oceans Pathfinder Version 5.0 SST dataset (*Casey* (2004)), which represents a reanalysis of the AVHRR data stream developed by the NOAA National Oceanographic Data Center (NODC) and Miami's Rosenstiel School of Marine and Atmospheric Science (RSMAS) and exhibits

[11] The arithmetic mean RH of *RV Polarstern*-based hourly means equals to 83.3% $\pm$ 11.7%. This is fairly close to the underlying assumption of 80% of *Liu et al.* (1994). However, the standard deviation indicates that the assumption may locally be considerably violated, introducing systematic errors into the HOAPS SAT retrieval and hence impacting atmospheric stability and eventually LHF.

Satellite ID	Approx. Equatorial Crossing (UTC)	Operational period	Average drifting rate
NOAA-9	09:09 / 21:09	01/1985 - 03/1995	+3.4 min / month
NOAA-11	05:17 / 17:17	09/1985 - 03/1995	+3.0 min / month
NOAA-14	01:33 / 13:33	12/1994 - 05/2007	+3.4 min / month

Table 5: NOAA satellites having operated between 1995-1997. AVHRR installed on board of the satellites deliver a robust data basis for the Oceans Pathfinder Version 5.0 SST dataset. AM equatorial crossing times refer to the descending node (crossing the equator north to south), whereas PM times are associated with the respective ascending node (vs.vs). Crossing time reference period: January 1995. See *Kilpatrick et al.* (2001) for a comprehensive description of the Pathfinder Algorithm.

a pixel-resolution of approximately 4 km. Based on the non-linear SST algorithm (NLSST[12]), SST estimates rely on the following equation:

$$SST_{SAT} = a + bT_4 + c(T_4 - T_5)SST_{guess} + d(T_4 - T_5)[sec(\Theta) - 1] \quad (4)$$

SST_{SAT} in ***Eq. 4*** denotes the satellite-derived SST estimate, T_4 and T_5 represent T_B in the $10.8\ \mu m$ and $11.4\ \mu m$ bands, respectively. SST_{guess} refers to a first-guess[13] SST and Θ to the satellite zenith angle. a, b, c, and d are the Pathfinder algorithm coefficients determined by a regression of collocated remotely-sensed ocean skin IR T_B and in-situ buoy data (*Kilpatrick et al.* (2001)).

All pixels are subject to several quality checks (see *Kilpatrick et al.* (2001)), which allocate quality flags ranging from 0 (poor) to 7 (very good), aiming to avoid a contribution of suspect pixels. This quality assessment omits values flagged 0-3 during further processing, which ensures that only high-quality pixels contribute to the final SST data product. Low-quality estimates often occur in regions of persistent cloud coverage (such as the Intertropical Convergence Zone (ITCZ) and polar regions during winter) (*Graßl et al.* (2000)), which supports the theory that bias range of the AVHRR measurements crucially depends on the applied aerosol and cloud detection schemes (compare *Reynolds* (1993) for a comprehensive error analysis in this regard).

As a minimum of two AVHRR instruments provide data at the same time and respective swath widths encompass extensive 2500 km, global coverage is reached twice a day. Similar to SSM/I data record density, several observations at any given spot on Earth, associated with multiple orbits, occur most frequently in higher latitudes. As long as quality indices fulfil a predefined standard, the Pathfinder algorithm combines these multiple observations to form an average, implying that the actual time of observation of any given pixel is not known.

[12] former version of the operational NOAA algorithm, see *Walton et al.* (1998a).

[13] first-guess SST are derived from the optimally interpolated weekly National Centers for Environmental Prediction (NCEP) SST analysis based on global buoy- and ship data as well as on NOAA AVHRR SST data developed by *Reynolds and Smith* (1994).

Subsequent to quality checks, AVHRR day- and night-time observations are averaged to daily mean SST maps with a resolution of $0.25°$. Regions exhibiting poor data coverage experience spatial and temporal interpolation. In a final step, data is remapped to SSM/I pixel-scan resolution. This results in SST fields as would be seen by the SSM/I and therefore leads to an internally consistent dataset.

A cold bias of 0.1K (day-time) up to 0.3K (night-time) compared to in-situ SST has been discovered (*Reynolds et al.* (2002)). These processing errors are most likely induced by cloud flagging procedures and the SST algorithm itself.

Overall, results of error analyses performed by *Kilpatrick et al.* (2001) suggest a global accuracy of the Pathfinder Algorithm 5.0 of $0.02 \pm 0.5°$C.

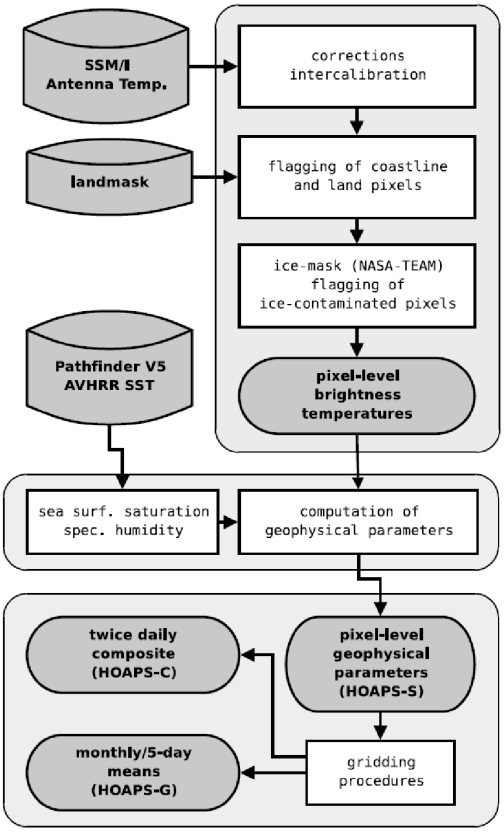

Fig. 2.4: Flow chart illustrating the data processing chain in HOAPS-3.0 from SSM/I antenna temperatures to final physical parameters. Adapted from *Andersson et al.* (2010).

A summarizing illustration of the individual raw data processing steps is provided in *Fig. 2.4* in form of a flow chart. As can be seen, SSM/I antenna temperatures are converted into internal T_B (according to *Wentz* (1991)) by means of instrument-related corrections, internal-sensor calibration as well as a filtering of poor-quality data pixel. Subsequently, T_B as well as AVHRR-based SST are pooled to compute geophysical parameters. The native SSM/I resolution (HOAPS-S) represents the final relevant step within the processing chain considered in the underlying work.

2.3 ERA-Interim Reanalysis

Apart from LHF estimates resulting from the application of bulk flux algorithms, it is desirable to resort to multivariate, spatially complete and coherent records of global geophysical parameters to validate the satellite-based HOAPS dataset. In the underlying work, these records are provided by the ERA-Interim reanalysis product (*Dee et al.* (2011)) initiated in 2006, which represents the latest global atmospheric reanalysis created by the European Centre for Medium-Range Weather Forecasts (ECMWF).

It covers the data-rich time period from 1979 to early 2013 and is continuously updated on a monthly basis in near-real time. Primarily, it serves not only as a transition between ECMWF's former reanalysis version ERA-40 (1957-2002, *Uppala et al.* (2005)) and a next-generation extended reanalysis in process of planning, but aims to improve several vital shortcomings associated with

ERA-40. These involve a more accurate representation of the hydrological cycle[14], the stratospheric circulation as well as the handling of data selection, quality control, bias corrections, and changes in the observing system (*Dee et al.* (2011)).

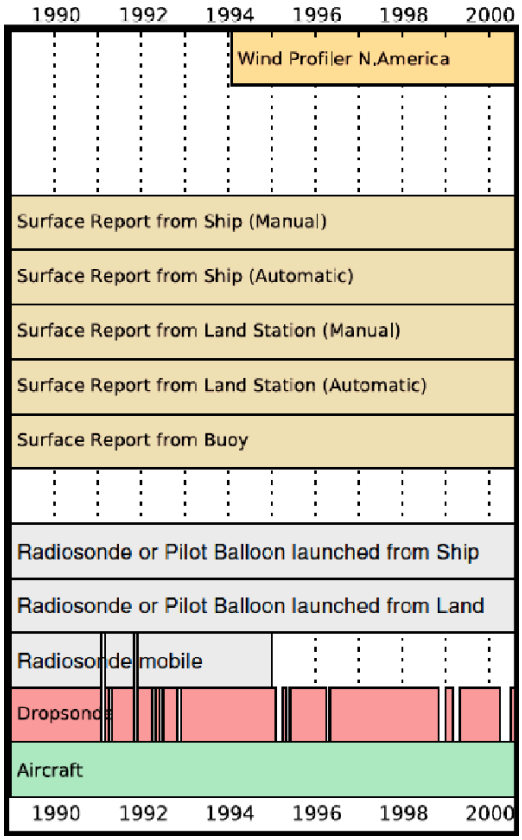

Fig. 2.5: Timeline of conventional observations assimilated in the ERA-Interim reanalysis between 1989-2000. Adapted and modified from *Dee et al.* (2011).

The ERA-Interim reanalysis is produced by means of a sequential data assimilation scheme, which advances forward in time using 12-hourly analysis cycles (*Dee et al.* (2011)). An implemented forecast model estimates the evolving state of the global atmosphere and surface, referring to available observations of various types and multiple sources as well as forecast output from the former time step. Near-surface parameters are then derived subsequently to upper-air atmospheric fields, both of which serve as a basis for initializing a short-range model forecast producing prior state estimates of need for the successive time step.

The unique combination of observations, analyses, and assimilating forecast model enables an extrapolation from locally observed information on parameters to nearby locations as well as their evolution in time.

Whereas upper-air atmospheric analysis is based on the assimilation system's core component, the four-dimensional variational analysis (4D-Var, compare *Courtier et al.* (1994)), 6-hourly estimates of surface parameters are derived subsequently via optimal interpolation based on Monin-Obhukov Similarity (MOS-) Theory (*Dee et al.* (2011), compare *Section 3.1.1*) by combining land-based synoptic observations with background estimates extracted from the latest atmospheric analysis (*Douville et al.* (1998)).

Observations assimilated in ERA-Interim exceed 10^6/day within the time period considered and are to a great extend composed of satellite data originating from, amongst others, polar-orbiting- and geostationary sounders and imagers as well as scatterometers delivering wind data. Additionally, conventional observing systems are accounted for, encompassing data obtained from radiosondes, pilot balloons, aircraft, wind profilers, ships, drifting buoys as well as land stations. Quality controls, the criteria of which are stated in blacklists, are performed in form of so-called background- and variational quality control checks (*Andersson and Järvinen* (1999)), aiming to identify non-credible data and preclude it from the reanalysis.

[14]Model physics within ERA-40 revealed a damped activity of the convection scheme, leading to a frequent atmospheric instability and consequently to enhanced precipitation activity. Resulting forecast errors have been considerably reduced within ERA-Interim by means of a sophisticated humidity parameterization (compare *Hólm* (2003)).

Finally, the short-range forecast, constituting the final part of the ECMWF reanalysis compilation loop, is produced with the Integrated Forecasting System (ITS) (*ECMWF* (2006)), which comprises a forecast model with three fully coupled components representing the atmosphere, the land surface as well as ocean waves. The atmospheric forecast model used for ERA-Interim is characterized by a 30 minute time step and a spectral T255 horizontal resolution, which corresponds to roughly uniform 79 km spacing for surface- and other grid point fields (*Berrisford et al.* (2011)). 60 vertical model levels, ranging from the surface to pressures of 0.1 hPa, represent the model's third dimension, which is identical to the version of ERA-40. SST and sea ice concentrations (SIC), which constitute parts of the forecast model's boundary conditions, are adapted from ERA-40[15] and eventually interpolated to the desired grid. The wave-model component embedded within ITS is based on the wave modelling (WAM-) approach (*Komen et al.* (1994)) and has a horizontal resolution of 110 km.

Parameter	**Unit**	**Field Type**	**Availability (UTC) of instantaneous values**	**Observational Data Sources**
u_{10m}	m/s	instant.	3, 6, 9, 12, 15, 18, 21, 24	scatterometer (ERS-1, ERS-2, QuikSCAT), AMV data (Meteosat, GOES, GMS, MTSAT), ship reports, buoys, SSM/I
v_{10m}	m/s	instant.	3, 6, 9, 12, 15, 18, 21, 24	compare sources of $u_{10\mathrm{m}}$
SAT_{2m}	K	instant.	3, 6, 9, 12, 15, 18, 21, 24	ship reports, buoys
SST	K	instant.	3, 6, 9, 12, 15, 18, 21, 24	AVHRR, ships, buoys
$T_{d,2m}$	K	instant.	3,6,9,12,15,18,21,24	ships, drifting buoys
ILR_{10m}	W/m^2s	accumul.	1:30, 4:30, 7:30, 10:30, 13:30, 16:30, 19:30, 22:30	HIRS / SSU, SSM/I
LHF_{10m}	W/m^2s	accumul.	1:30, 4:30, 7:30, 10:30, 13:30, 16:30, 19:30, 22:30	MOS-Theory, compare *Section 3.1.1*

Table 6: Overview of geophysical parameters downloaded from the ECMWF ERA-Interim forecast data archive. Subscripts denote the height ASL, where the individual parameters are defined. All fields are given in three-hourly resolution and are available on a regular 0.75° x 0.75° grid. Compare *Uppala et al.* (2005) for more detailed information on observations assimilated in ERA-Interim.
Abbreviations: instant.: instantaneous (see text); accumul.: accumulated (see text); ERS: European Remote Sensing Satellite; QuikSCAT: Quick scatterometer; AMV: Atmospheric Motion Vector; GOES: Geostationary Operational Environmental Satellite; GMS: Geostationary Meteorological Satellite; MTSAT: Multifunctional Transport Satellite; HIRS: High-Resolution Infrared Sounder; SSU: Stratospheric Sounding Unit.

For validation purposes of HOAPS pixel-scan resolution data, several geophysical parameters have been extracted from the open-access ECMWF Data Server[16]. Those exclusively consist of surface forecast fields ranging from January 1995 to January 1998, which are initiated at 00 UTC and 12 UTC and comprise global forecasts in a temporal resolution of three hours. Compared to the surface analysis fields, the forecast's data temporal resolution is twice as large, which makes its use attractive

[15]Between 1981-2002, SST was extracted from the weekly NOAA/NCEP 2D-Var dataset (compare *Reynolds et al.* (2002)) and relied on a sea ice analysis, which was developed jointly for the use in ERA-40 (*Rayner* (2002)).
[16]*http://data-portal.ecmwf.int/data/d/interim_daily*.

for validation studies. *Table 6* provides an overview of ERA-Interim-based geophysical parameters analysed within this study.

All datasets originating from ERA-Interim within this work incorporate grid point data values, implying that they are not averaged area-wise but are rather valid at the exact location of the grid points. The grid itself is regular with a $0.75°$ x $0.75°$ resolution.

Forecast data is either given in form of instantaneous or accumulated fields. The former output originates from an analysis and is based on a forecast step of three hours. Conversely, parameters of the latter kind are accumulated from the beginning of the forecast. Amongst others, these comprises surface fluxes like the incident longwave radiation (ILR, supplements in-situ data, as it is needed to apply the bulk flux algorithms described in *Section 3.1.3* / *Section 3.1.5*) as well as LHF. To obtain the average between two forecast steps, the grid point-wise difference of both single fields was retrieved and multiplied by the inverse of the forecast step.

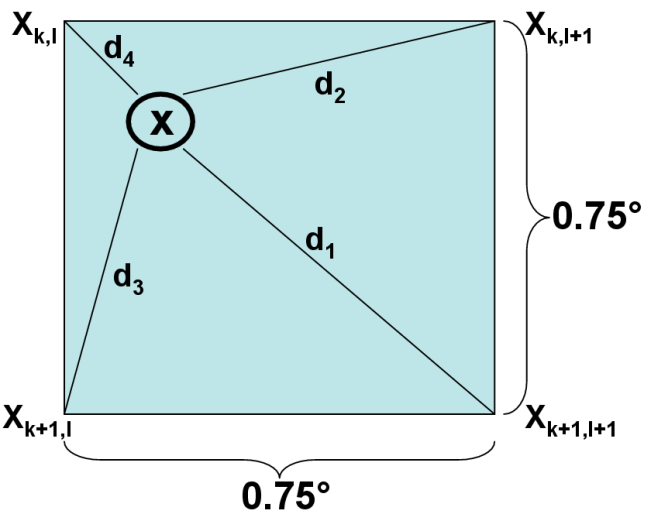

Fig. 2.6: Sketch of weighted four-point averaging procedure to match ERA-Interim reanalysis data (defined at grid points, represented by the four edges of the box) to the ship's concurrent geographical location (indicated by encircled 'x'). d_x ($x \in [1-4]$) represents the great circle distance to the individual grid point. The matching ERA-Interim value at the encircled 'x' is calculated as a blend of the four corner values, weighted by the inverse of their distance to the ship's concurrent position.

As forecast fields of $q_{a,10m}$ on a three-hourly basis are not available in the ERA-Interim data archive, it was calculated separately. Given that RH cannot be considered as a conserved quantity in different heights within the boundary layer, the adjustment from ERA-based $q_{a,2m}$ to $q_{a,10m}$ is performed on the basis of atmospheric stability considerations (see *Section 3.1.3* and *Section 3.1.5*), assuming *RV Polarstern* data to represent the ground truth[17]. The average q_a decrease from 2 m to 10 m ASL is given by $0.036\ g/kg$, corresponding to $\approx$ 0.6%. Although this modification may appear negligible, the full range of $q_{a,2m} - q_{a,10m}$ encompasses $-0.47\ g/kg$ to $+0.33\ g/kg$, associated with several % of relative deviation compared to $q_{a,2m}$. As will be discussed later, this considerably influences the resulting LHF, which underlines the importance of applying a stability-dependent q_a adjustment.

Absolute wind speed fields (10 m ASL) were calculated by applying Pythagoras' theorem to the zonal and meridional wind components.

Subsequently, all parameters listed in *Table 6* were matched to every available hourly mean of

[17]Based on *RV Polarstern* data, both $q_{a,2m}$ and $q_{a,10m}$ are derived independently by means of the Oceanet bulk flux algorithm (compare *Section 3.1.5*). Assuming the algorithm to correctly assess the ambient stratification, the resulting $q_{a,2m} - q_{a,10m}$ is transferred to the ERA-based $q_{a,2m}$ data to finally yield hourly ERA estimates of $q_{a,10m}$.

RV Polarstern data, in as much as reanalysis data closest in time and space to the respective in-situ record was located. Considering the ERA-Interim field associated with the smallest temporal deviation from a *RV Polarstern* measurement, the ship's concurrent geographical position was extracted to perform a weighted four-point averaging procedure based on ratios of great circle distances[18] (see sketch in *Fig. 2.6*). In the case of accumulated fields, the respective instantaneous values correspond to the center of the time step interval (compare *Table 6*, *Column 4*), owing to the fact that two ERA-Interim fields may be equally close in time to the matching in-situ measurement. In the latter case, the arithmetic mean of both weighted four-point averages is considered as the most accurate match of reanalysis data to the ship's records. Ultimately, match-ups of ERA-Interim (*ERA*, as of now) geophysical parameters are available in a one-hourly resolution, which facilitates the HOAPS validation, as results involving both in-situ and reanalysis data may be confronted easier.

[18]The great-circle distance D represents the shortest distance [$^\circ$] between two points on the surface of a sphere, measured along a path on its surface. In case a and b are latitudes [$^\circ$] and $|c|$ the absolute value of the longitudinal difference between the respective coordinates, D can be inferred via $cos(D) = (sin(a) \cdot sin(b)) + (cos(a) \cdot cos(b) \cdot cos(|c|))$.

3 Methodology

3.1 Monin-Obukhov Similarity Theory and Bulk Flux Algorithm Applications

3.1.1 Monin-Obukhov Similarity (MOS-) Theory

All bulk flux algorithms underlying this work follow the standard surface Monin-Obhukov Similarity (MOS-) Theory (*Monin and Obukhov* (1954)), which can be applied to yield surface LHF on the basis of bulk meteorological measurements. The similarity hypothesis assumes that in a horizontally homogeneous, quasi-stationary surface layer (so-called constant flux layer), the mean flow and turbulence characteristics are solely functions of four independent parameters (*Arya* (2001)), namely the height z above the surface[19], the surface drag τ_0/ρ, the surface kinematic heat flux $H_0/\rho c_p$, and the buoyancy variable g/T_0. Molecular exchanges are considered to be insignificant and the influence of boundary layer height, surface roughness as well as geostrophic winds is fully accounted for in τ_0/ρ.

Three fundamental dimensions are introduced (length L, velocity U, and temperature T), the dimensionless combination of which is independent and expressed by a universal function of a stability parameter $\zeta = \frac{z}{L}$. ζ represents the ratio of buoyancy and shear effects, where z corresponds to the reference height and the length scale L represents the Obukhov Length, i.e. the characteristic height scale of the sublayer of dynamic turbulence (*Obukhov* (1946)) (compare *Eq. 6c* further down and e.g. *Liu et al.* (1979)).

The similarity prediction now states, that any mean flow or averaged turbulence quantity, normalized by a combination of these scales, is a unique function of ζ.

By means of bulk meteorological- and SST data, the application of the MOS-Theory thus enables the expression of non-dimensional vertical profiles of wind shear- (m), temperature- (h), and moisture (q) gradients in terms of stability-dependent gradient functions ϕ_m, ϕ_h, and ϕ_q:

$$\frac{\kappa z}{u_*}\overline{\frac{du}{dz}} = \phi_m(\zeta) \tag{5a}$$

$$\frac{\kappa z}{\Theta_*}\overline{\frac{d\Theta}{dz}} = \phi_h(\zeta) \tag{5b}$$

$$\frac{\kappa z}{q_*}\overline{\frac{dq}{dz}} = \phi_q(\zeta), \tag{5c}$$

[19] typically the sensor height or normed to 10 m ASL.

where

$$\Theta_* = -\frac{\overline{w'\Theta'}}{u_*} \tag{6a}$$

$$q_* = -\frac{\overline{w'q'}}{u_*} \tag{6b}$$

$$\begin{aligned}\zeta &= \frac{z}{L} \\ &= z \cdot \left[\frac{(T_v u_*)^2}{g\kappa\Theta_*}\right]^{-1} \\ &= z \cdot \left[\frac{(T(1+0.61q)u_*)^2}{g\kappa(T_*(q-0.61q)+0.61Tq_*)}\right]^{-1}.\end{aligned} \tag{6c}$$

u_*, Θ_*, and q_* represent momentum-, temperature-, and moisture scales. $\overline{u}$, $\overline{\Theta}$, and $\overline{q}$ correspond to the horizontal mean wind speed, potential temperature, and specific humidity, respectively. T_v and κ denote the virtual potential temperature and the von Kármán constant[20]. $\overline{w'\Theta'}$ and $\overline{w'q'}$ describe the surface kinematic heat- and moisture fluxes.

Solving the stability-dependent integral versions of ϕ_x, i.e. Ψ_x[21], allows to iteratively determine the transfer coefficient C_e (compare *Eq. 8* further down) and eventually the scaling parameters u_* and q_*, which allow for deriving LHF in an asymptotic approach via *Eq. 7* (compare further down).

A description of the COARE3.0 bulk flux algorithm (*Fairall et al.* (2003)), which also constitutes the basis for HOAPS LHF, is provided in *Section 3.1.3*. Modifications among the Oceanet- and ERA flux algorithms are briefly pointed out in *Section 3.1.4* and *Section 3.1.5*.

3.1.2 Scientific Basis of the Bulk Flux Algorithm COARE3.0

As the interfacial fluxes between ocean and atmosphere to the Earth's climate are crucial in terms of energy balance considerations and the role of the tropics therein vital, the Tropical Ocean-Global Atmosphere (TOGA) Program, being a component of the World Climate Research Program, was initiated in 1985 and led to the Coupled Ocean-Atmosphere Response Experiment (COARE, *Webster and Lukas* (1992)). On the basis of measured bulk variables, the latter's primary aim was to estimate the air-sea fluxes by applying a bulk flux algorithm and yield a maximum uncertainty of $10\ W/m^2$ in the total surface energy budget of the ocean (*Fairall et al.* (1996)).

[20] κ describes the logarithmic velocity profile of a turbulent atmospheric flow within the boundary layer, given the no-slip condition at the direct interface. The exact value of κ has been subject to considerable debate, but 0.4 represents the most widely accepted value (e.g. *Hogstrom* (1988)).

[21] x may be replaced by m, h, and q. The similarity MOS profile functions Ψ_m, Ψ_h, and Ψ_q differ, depending on whether prevailing atmospheric stratifications are stable ($\zeta > 0$) or unstable ($\zeta < 0$). As similarity between water vapor and heat transfer is assumed, it follows that $\Psi_h = \Psi_q$.

The COARE bulk flux scheme started to develop from 1990 onwards with a pilot cruise in the western Pacific (*Young et al.* (1992)) and continued with three, mostly station-based cruise legs of *RV Moana* between 11/1992 - 02/1993, to which the algorithm was tuned to. Originally, the focus was restricted to the light wind region of the Western Pacific in the so-called COARE region (2°S / 156°W), where 50-minute averages of bulk meteorological measurements and concurrent direct flux measurements were obtained.

Cruise name	Dates	Hours	Vessel	Lat	Lon	Reference
TIWE	21 Nov–13 Dec 1991	460	*Moana Wave*	0°	140°W	Chertock et al. (1993)
ASTEX	6–28 Jun 1992	390	*M. Baldrige*	30°N	25°W	White et al. (1995)
COARE-1	11 Nov–3 Dec 1992	589	*Moana Wave*	2°S	156°E	Fairall et al. (1996)
COARE-2	17 Dec 1992–11 Jan 1993	648	*Moana Wave*	2°S	156°E	Fairall et al. (1996)
COARE-3	28 Jan–16 Feb 1993	385	*Moana Wave*	2°S	156°E	Fairall et al. (1996)
SCOPE	17–28 Sep 1993	305	*FLIP*	33°N	118°W	Edson and Fairall (1998)
FASTEX	23 Dec 1996–24 Jan 1997	730	*Knorr*	45°N	10°–60°W	Hare et al. (1999)
JASMINE	5–31 May 1999	654	*Ron Brown*	8°N	89°E	Fairall et al. (2000)
NAURU99	15 Jun–18 Jul 199	794	*Ron Brown*	0.5°S	167°E	Fairall et al. (2001)
KWAJEX	28 Jul–12 Sep 1999	875	*Ron Brown*	8°N	167.5°E	None
Moorings	14 Sep–21 Oct 1999	746	*Ron Brown*	52°N	140°W	None
PACSF99	11 Nov–2 Dec 1999	640	*Ron Brown*	±10°N	100°W	None

Fig. 3.1: Summary of cruises involving air-sea flux- and bulk meteorological measurements, which serve as a basis for COARE3.0 outlined in *Section 3.1.3*. Abbreviations: Tropical Instability Wave Experiment (TIWE), Atlantic Stratocumulus Transition Experiment (ASTEX), Coupled Ocean-Atmosphere Response Experiment (COARE), San Clemente Ocean Probing Experiment (SCOPE), Fronts and Atlantic Storms (FASTEX), Joint Air-Sea Monsoon Experiment (JASMINE), Nauru '99 Experiment (NAURU99), Tropical Rainfall Measuring Mission (TRMM)/Kwajalein Experiment (KWAJEX), Pan American Climate Studies fall 1999 study (PACSF99). Adapted from *Fairall et al.* (2003).

Whereas COARE2.5b (*Fairall et al.* (1996)) can be considered as an only slightly modified version of the Liu-Katsaros-Businger model (LKB) model approach (*Liu et al.* (1979)), the algorithm has continuously been improved (*Bradley et al.* (2000)), culminating in the most recent version, namely COARE3.0 (*Fairall et al.* (2003)). The latter is based on twelve cruises between 1991-1999, which covered latitudinal bands between 2°S - 52°N. In contrast to former versions, the data basis has thus been extended to strong wind- and cold water regimes and has been globalized, in as much as an extension of bulk- and direct turbulence measurements in the Atlantic- and Indian Ocean have been included (see *Fig. 3.1*). *Fairall et al.* (2003) therefore argue that its application in the mid-latitudes and even polar regions is justifiable. The database, on which COARE3.0 is founded, comprises a total number of 7216 hourly means of observations, 11% of which are subject to high wind speeds ($> 10\ m/s$) and 30% to extratropical latitudes (*Fairall et al.* (2003)).

The recent generalization of the algorithm for more global applications served as a motivation to apply COARE3.0 as one of two bulk flux algorithms to hourly means of *RV Polarstern* data within this work, the data density of which is concentrated on extratropical latitudes of the Atlantic Ocean (compare *Fig. 2.1*).

The freely available COARE3.0 bulk algorithm code (*Fairall* (2006), *Coare* as of now) was down-

loaded from the Earth System Research Laboratory (ESRL) homepage[22] and applied to hourly bulk meteorological measurements described in *Section 2.1*.

3.1.3 Mathematical Representation of Surface LHF within Coare / HOAPS

Following *Fairall et al.* (1996), the turbulent flux of latent heat is given by

$$H_l = \rho_a L_e \overline{w'q'} = -\rho_a L_e u_* q_*. \tag{7}$$

As shown, the derivation of H_l does not need to result from measurements of turbulent fluctuations via direct eddy covariance measurements (*Eq. 7*, center), but can also be expressed in terms of the MOS scaling parameters u_* and q_*.

In terms of bulk parameters, H_l in *Eq. 7* can alternatively be expressed by a proportionality constant known as the transfer coefficient for latent heat, C_e, i.e.

$$H_L = \rho_a L_e C_e S(q_s - q_a), \tag{8}$$

where S corresponds to the mean wind speed relative to the ocean's surface at height z, ρ_a represents the mean surface density of the atmosphere, and L_e denotes the SST-dependent latent heat of vaporisation. q_a and q_s depict near-surface and surface saturation specific humidities, respectively. C_e is stability-dependent and derived via its neutral ($\zeta = 0$) representation at 10 m ASL (compare *Eqs. 8-9* and *Eq. 13*). This so-called 'reduction', which removes the stability dependency and thus facilitates the intercomparison of measurements, analogously accounts for the transfer coefficients for sensible heat and momentum, namely C_h and C_d. As is indicated in *Eqs. 10-11*, these are involved in the LHF calculation as well.

C_e, C_h, and C_d can be decomposed into two individual components and may be written as analytical functions depending on ζ, namely

[22] *ftp://ftp1.esrl.noaa.gov/users/cfairall/wcrp_wgsf/computer_programs/cor3_0/*

$$
\begin{aligned}
C_e &= \sqrt{c_q c_d} \\
&= \left[\sqrt{c_{qn}}\left(1 - \frac{\sqrt{c_{qn}}}{a\kappa}\Psi_q(\zeta)\right)^{-1}\right] \cdot \left[\sqrt{c_{dn}}\left(1 - \frac{\sqrt{c_{dn}}}{\kappa}\Psi_m(\zeta)\right)^{-1}\right], \qquad (9)
\end{aligned}
$$

$$
\begin{aligned}
C_h &= \sqrt{c_T c_d} \\
&= \left[\sqrt{c_{hn}}\left(1 - \frac{\sqrt{c_{hn}}}{a\kappa}\Psi_h(\zeta)\right)^{-1}\right] \cdot \left[\sqrt{c_{dn}}\left(1 - \frac{\sqrt{c_{dn}}}{\kappa}\Psi_m(\zeta)\right)^{-1}\right], \qquad (10)
\end{aligned}
$$

$$
\begin{aligned}
C_d &= \sqrt{c_d c_d} \\
&= \left[c_{dn}\left(1 - \frac{\sqrt{c_{dn}}}{\kappa}\Psi_m(\zeta)\right)^{-2}\right]. \qquad (11)
\end{aligned}
$$

c_{qn}, c_{hn}, and c_{dn} refer to the reduced versions of C_e, C_h, and C_d, i.e. to the neutral[23] transfer coefficients for moisture, sensible heat, and momentum (compare ***Eq. 13*** below). κ is set to 0.4 and a accounts for the difference in scalar and velocity von Kármán constants. The scaling parameters may now be expressed according to

$$T_* = -\sqrt{c_T}(T_s - \Theta) \qquad (12a)$$

$$q_* = -\sqrt{c_q}(q_s - q) \qquad (12b)$$

$$u_*^2 = C_d S u = C_d S^2. \qquad (12c)$$

T_s and Θ specify sea surface temperature and air potential temperature, respectively. c_{hn}, c_{dn}, and c_{qn} can be related to the roughness lengths for temperature (z_{0T}), velocity (z_0), and humidity (z_{0q}), which correspond to the height, where the extrapolation of the logarithmic profiles of temperature, wind, and specific humidity intersect the surface values:

[23] the subscript n in ***Eq. 11*** denotes the neutral stability environment, i.e. $\zeta = 0$. Strongly unstable conditions are present if $\zeta << 1$, i.e. when mechanical turbulence due to wind shear dominates buoyancy effects. Vice versa for stable conditions, where $\zeta > 1$.

$$\sqrt{c_{qn}} = \frac{a\kappa}{log(z_r/z_{0q})} \tag{13a}$$

$$\sqrt{c_{dn}} = \frac{\kappa}{log(z_r/z_0)} \tag{13b}$$

$$\sqrt{c_{hn}} = \frac{a\kappa}{log(z_r/z_{0T})}. \tag{13c}$$

As suggested by *Smith* (1988), the velocity roughness length z_0 in *Eq. 13* is best approximated when combining versions of the LKB-model (*Liu et al.* (1979), first term on r.h.s. in *Eq. 14*) and *Charnock* (1955) (second term on r.h.s. in *Eq. 14*) :

$$z_0 = \alpha\frac{u_*^2}{g} + 0.11\frac{\nu}{u_*}. \tag{14}$$

ν depicts the kinematic viscosity ($1.5 \cdot 10^5 \frac{m^2}{s}$) and α represents the Charnock parameter, which incorporates a wind speed dependence in Coare and ranges between 0.011 and 0.017. Linking the roughness lengths and the scaling parameters, the surface and the flow regime can be expressed in terms of the roughness Reynolds number R_r, R_T, and R_q, namely

$$R_r = \frac{u_* z_0}{\nu} \tag{15a}$$

$$R_T = \frac{u_* z_{0T}}{\nu} \tag{15b}$$

$$R_q = \frac{u_* z_{0q}}{\nu}, \tag{15c}$$

Referring to coefficients published in *Liu et al.* (1979), R_T and R_q can be derived from R_r (not shown).

In unstable, near-neutral cases ($-1 < \zeta < 0$), the scalar profile functions Ψ_m, Ψ_h, and Ψ_q are treated as modified versions of *Businger et al.* (1971), which are given by *Paulson* (1970) (compare *Beljaars and Holtslag* (1991), *Eqs. 25-26* therein).

Additionally, the so-called free convection limit[24] (*Panofsky and Dutton* (1984)) is accounted for within a second version of the instable profile functions (compare *Grachev et al.* (2000), *Eq. 12* therein).

Coare adopts a blend between *Beljaars and Holtslag* (1991), *Eqs. 25-26* and *Grachev et al.* (2000), *Eq. 12* for $\zeta < 0$, the final form of which is published in *Fairall et al.* (1996) (*Eq. 26* therein).

[24]this asymptotic limit of the MOS-Theory incorporates the case of $\zeta \to -\infty$ and concurrent $U \neq 0$, where U is the mean wind speed.

In strongly stable environmental conditions ($\zeta > 1$), profile functions of *Beljaars and Holtslag* (1991) are applied, which are based on revised profile data obtained in extremely stable conditions. Their mathematical representation is given in *Beljaars and Holtslag* (1991), *Eq. 31* therein.

At this stage, the stability iteration loop is initiated. Instead of assuming a neutral stability (i.e. $\zeta = 0$), as was done in COARE2.5, a first guess of ζ in Coare is based on the bulk Richardson Number R_{ib}[25] (*Grachev and Fairall* (1997)), i.e.

$$\zeta = C_b R_{ib}(1 - BR_{ib})^{-1}, \tag{16}$$

with $B = 5$, $C_b = \kappa / c_{dn}^{0.5} \approx 10$ and $R_{ib} = \frac{-gz\Delta\Theta_\nu}{TU^2}$ with Θ_ν being the virtual potential temperature.

Eq. 16 allows for determining the scaling parameters in *Eq. 12*, followed by L and eventually the stability ζ (*Eq. 6c*), z_0 (*Eq. 14*), all scalar roughness Reynolds numbers (*Eqs. 15a-c*) and *Liu et al.* (1979)) and consequently the scalar roughness lengths z_0, z_{0T}, and z_{0q}. Subsequently, the neutral transfer coefficients in *Eq. 13* are determined, followed by the computation of the stability-dependent profile functions, the stability-dependent transfer coefficients (*Eqs. 9-11*) as well as revised scaling parameters from *Eq. 12*. Finally, the latent heat flux H_l is derived via *Eq. 7*.

Due to radiative and turbulent fluxes, the uppermost millimeter of the surface ocean layer is cooled by $0.2 - 0.5\ K$, representing the so-called cool-skin effect (*Saunders* (1967)). However, the bulk-SST measured on *RV Polarstern* are obtained from a depth of 5m, implying that the surface skin effect cannot be quantified directly.

Additionally, the uppermost meter of the ocean absorbs roughly 50% of the short-wave radiation (*Fairall et al.* (2003)), which may contribute to a diurnal, solar-induced warming on a local scale. This warm layer effect has to especially be accounted for within low-wind regimes, where measured bulk-SST and 'true' SST may differ by several Kelvin.

Both warm-layer and cool-skin effect represent bias sources in the LHF-estimation, if not accounted for in the flux algorithm. Thus, respective corrections to T_s and q_s and re-performances of the stability iteration loop are carried out subsequent to each iteration step, until convergence is reached.

3.1.4 Mathematical Representation of Surface LHF in ERA

The surface layer approximation within the ERA IFS is applied from the surface to the lowest model level (10 m ASL). Within this vertical range, turbulent fluxes are assumed to be constant with height and equal to the surface values.

[25] R_{ib} represents the ratio of thermally produced turbulence and turbulence driven by vertical shear. Convection tends to be free for large R_{ib} and vice versa in cases of forced convection.

The bulk flux algorithm constituting the basis of the ERA LHF closely resembles that of *Section 3.1.3*. Yet, a few noteworthy differences are emphasized in the following.

Whereas the Coare (HOAPS) and ERA algorithms apply *Eq. 14* to derive z_0, their Charnock parameter representation differs. In contrast to the wind speed dependency noted in *Section 3.1.3*, ERA-based LHF rely on a constant $\alpha = 0.018$. Furthermore, $z_{0q} \neq z_{0T}$, as suggested by *Beljaars* (1994). Their expressions are given by

$$z_{0T} = \alpha_T \cdot \frac{\nu}{u_*} = 0.40 \cdot \frac{\nu}{u_*} \tag{17a}$$

$$z_{0q} = \alpha_q \cdot \frac{\nu}{u_*} = 0.62 \cdot \frac{\nu}{u_*}. \tag{17b}$$

Finally, the universal profile functions Ψ_m, Ψ_h, and Ψ_q take on the same form during stable conditions, however differ for unstable stratifications. For the latter, the ERA algorithm does not incorporate the free convection limit and thus solely relies on the relationships proposed by *Businger et al.* (1971). In addition, underlying gradient functions ϕ_m and ϕ_h differ slightly among their coefficients a:

$$\phi_m(\zeta) = (1 - a\zeta)^{0.25} \tag{18a}$$

$$\phi_h(\zeta) = (1 - a\zeta)^{0.50} = \phi_q(\zeta). \tag{18b}$$

In *Section 3.1.3*, a equals to 15 (compare *Dyer* (1967)), whereas it takes on a value of 16 within the ERA-based code, following *Dyer* (1974) and *Hogstrom* (1988).

More details on the LHF implementation within ERA can be obtained from the ECMWF IFS (*ECMWF* (2006)).

3.1.5 Mathematical Representation of Surface LHF within Oceanet

Within the framework of OCEANET[26], which aimed to assess the energy exchange between ocean and atmosphere, direct turbulence measurements were carried out on *RV Polarstern* between 2008-2010 (compare *Table 7*). These four cruises provided the basis for establishing an independent bulk flux algorithm at Geomar (Kiel) similar to Coare (*Fairall et al.* (2003)), termed *Oceanet* as of now.

Apart from hourly observations of bulk variables (air temperature and humidity 32 m ASL, wind speed 39 m ASL, amongst others), the turbulence measurements were carried out by means of a sonic

[26]OCEANET - Autonomous measurement platforms for energy and material exchange between ocean and atmosphere. Compare *http://www.uni-leipzig.de/ strahlen/web/research/en_index.php?goto=oceanet* for further details.

Campaign	Departure / Arrival	Cruise Start / End	Cruise Report
ANT-XXIV/4	Punta Arenas - Bremerhaven	2008-04-18 / 2008-04-20	*Macke* (2009)
ANT-XXV/5	Punta Arenas - Bremerhaven	2009-04-11 / 2009-05-24	*Zenk and Naggar* (2010)
ANT-XXVI/1	Bremerhaven - Punta Arenas	2009-10-16 / 2009-11-25	*El Naggar and Macke* (2010)
ANT-XXVII/1	Bremerhaven - Cape Town	2010-10-25 / 2010-11-26	*Bumke* (2011)

Table 7: Overview of RV Polarstern Cruises within the framework of OCEANET. The four listed transect cruises served as a basis for developing the independent bulk flux algorithm *Oceanet* at Geomar (Kiel).

anemometer[27] and an absorption hygrometer[28], both of which were installed 32 m ASL.

The Oceanet bulk algorithm is predicated on flux estimates via the indirect inertial-dissipation (ID) method (compare e.g. *Edson et al.* (1991) for further details on the ID methodology).

In contrast to *Fairall et al.* (2003), the ocean skin temperature was determined following a simpler approach of *Hasse* (1971). A warm layer correction was not applied, arguing that the rate of ocean surface heating is a continuous process, which, at a given location, depends on often unknown surface radiation estimates several hours prior to the observation.

As in Coare, the Oceanet algorithm refers to the integrated stability functions of *Beljaars and Holtslag* (1991) (stable) as well as the blend for unstable conditions published in *Fairall et al.* (1996) (*Eq. 26* therein), depending on whether free convection is evident or not. Furthermore, the same wind speed dependent Charnock Parameter as is implemented in Coare is applied within Oceanet, as is $z_{0T} = z_{0q}$. The first guess of the turbulent fluxes is obtained via a modified bulk scheme after *Liu and Blanc* (1984).

The arithmetic mean of the wind speed dependent neutral transfer coefficients[29] at 10 m ASL, which directly impact the scaling parameters and thus LHF, were derived via a linear fitting procedure:

$$C_{e,10n} = (1.06 + 0.0118U_{10n}) \cdot 10^{-3} \tag{19a}$$

$$C_{h,10n} = (1.03 + 0.005U_{10n}) \cdot 10^{-3} \tag{19b}$$

$$C_{d,10n} = (0.86 + 0.062U_{10n}) \cdot 10^{-3}. \tag{19c}$$

U_{10n} denotes the reduced wind speed at 10 m ASL assuming neutral stability ($\zeta = 0$) and U refers to the absolute wind speed measured at 37 m ASL.

[27] Type USA-1, manufactured by METEK, Pinneberg, Germany. sampling rate: 30 Hz.
[28] Type M100, manufactured by Analytical Application, Boulder, USA. Sampling rate: 10 Hz.
[29] slightly different compared to Coare3.0

In the framework of validating Oceanet-based hourly LHF, a comparison to averages of directly measured fluxes gives a correlation coefficient of 0.95, a standard deviation of $\pm$ 20.2 W/m^2, and a bias of 3.9 W/m^2. The robustness of the algorithm has been confirmed in a separate statistical comparison to hourly Coare-based LHF output, based on the application of identical bulk input parameters (Bumke, pers. comm., May 2013). As with Coare, the Oceanet algorithm is applied to the hourly bulk meteorological measurements described in *Section 2.1*. A confrontation of Coare and Oceanet within this study is presented within *Section 4.1*.

3.2 Collocation Preparation - Decorrelation Scales

Two different approaches can in general be applied to compare satellite measurements to in-situ datasets for validation purposes. On the one hand, the observational data may be interpolated to match those originating from the satellite. On the other hand, one can approach the problem by means of finding those satellite recordings, which are closest in time (concurrent) and space (co-located) to the respective in-situ data. As the latter method, amongst others, does not only save computational energy, but also avoids smoothing of extremes (which are essential in the validation procedure), this so-called 'nearest neighbour' approach is chosen within this work and termed *collocation* as of now.

Due to the satellites' rapid propagation (6.58 km/s), the probability of applied SSM/I instruments to traverse *RV Polarstern* simultaneously to an hourly in-situ measurement remains very low. To nevertheless allow for matching HOAPS- to ship- (and ERA-) based records, the nearest neighbour attempt permits small spatial and temporal shifts between both data sources, respectively.

The question remains as to how the thresholds of these shifts should be specified. A too strict strategy (i.e. too small shifts) would reduce the available match-ups in a needless manner. A too generous approach, to the contrary, would concede collocated pairs, the underlying data of which may not be physically meaningful. The problem is further complicated, as only one research vessel is available, which propagates simultaneously in time and space. The latter inhibits the separate derivation of temporal and spatial shifts at the same instant.

The issues addressed above are solved by initially calculating *temporal* decorrelation timescales Γ (see *Eq. 22*) of the in-situ dataset, which serve as a basis for deriving the *spatial* decorrelation timescales Υ subsequently.

Assuming the discrete time series of hourly ship observations, X, to be generated by a stationary process, its autocorrelation solely depends on the time lag $\tau = t_2 - t_1$, where t_1 and t_2 correspond to arbitrary times. Accordingly, the autocovariance function is defined as

$$R(\tau) = cov(X_t, X_{t+\tau}) = E((X_t - \mu) \cdot (X_{t+\tau} - \mu)), \tag{20}$$

the normalization (by σ^2) of which leads to the autocorrelation function (ACF)

$$\rho(\tau) = \frac{R(\tau)}{R(0)} = \frac{R(\tau)}{\sigma^2}, \tag{21}$$

where $t = 0, \pm 1, \pm 2$, ... and μ represents the expected value of X.

The largest permitted temporal shift between ship- and HOAPS-based records is defined by Γ, which can be expressed as follows:

$$\Gamma = \int_0^\infty \rho(\tau) d\tau. \tag{22}$$

Definitions of Γ vary in literature; here, it is defined as the time lag after which a reduction of ρ to its e-folding value[30] has occurred. Depending on the geophysical parameter and the climate zone, Γ exhibits a considerable spread (*Strehz et al.* (2009)). As mid-latitudinal regions are characterized by frequent passages of frontal zones, associated with strong gradients in wind speed, specific humidity, and consequently also LHF, respective decorrelation time scales are expected to be small compared to (sub-)tropical regions.

To avoid too generous collocation requirements, *Eqs. 20-22* are applied to 24-hour sub time series obtained in the mid-latitudes between $40° - 60°$ N/S (compare *Fig. 3.2*). For reasons of simplicity, the outcome of Γ is applied to data within all latitudinal bands. As only $\approx 22\%$ of all measurements performed on *RV Polarstern* between 1995-1997 were obtained equatorwards of $40°$ N/S and owing to a general large data availability, this assumption is justified.

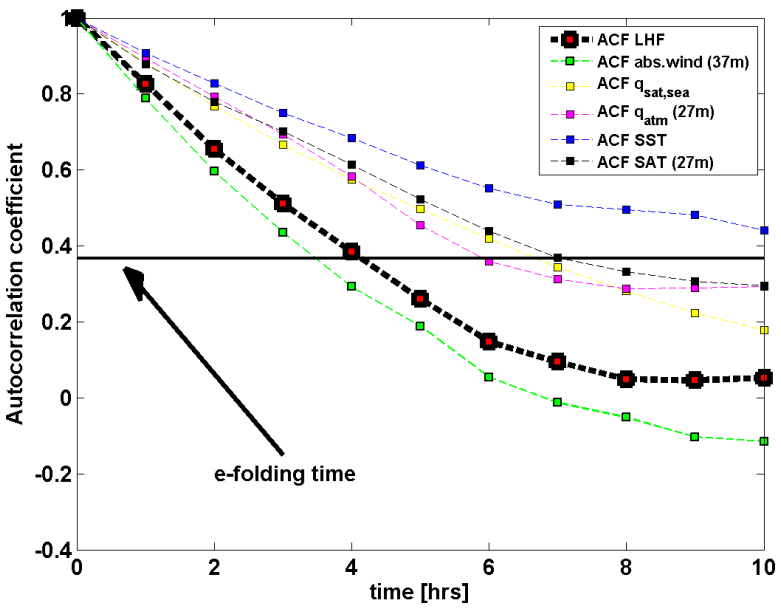

Fig. 3.2: $\rho(\tau)$ of several geophysical bulk parameters (thin, dashed lines), on which the latent heat flux (thick, dashed line) depends on. All ACFs represent arithmetic means composed of 23 subseries between $40°$-$60°$ N/S each of which are 24 hours long. A rather constant, relatively high ship speed underlies these subseries, allowing for an estimation of Υ later on. $q_{sat,sea}$ equals to q_s in the text. The black horizontal line indicates the e-folding value. Its intersection with the individual $\rho(\tau)$ contours allows for deriving the respective parameter-dependent Γ. Compare text for interpretation.

Fig. 3.2 illustrates ship-based $\rho(\tau)$ for several bulk input parameters (thin, dashed contours), on which LHF (thick, dashed contour) depends. All $\rho(\tau)$ fall off in an exponential manner, indicating a first-order Markov process (*Trenberth* (1985)). As can be seen, $\rho(\tau)$ associated with LHF falls below $1/e$ for $\Gamma = 4$ hours, owing to

[30] the time lag, at which the autocorrelation function has dropped to $1/e \approx 0.37$.

fairly large Γ of q_a and q_s (SST) and concurrent smallest Γ associated with absolute wind speeds $\vec{u}$.

In order to circumvent large collocation biases owing to an overestimation of the decorrelation time scale, the latter is defined to be $\Gamma = 3$ hours for *all* displayed parameters in ***Fig. 3.2***, following the absolute wind speed possessing the least temporal persistency of all.

Given Γ, Υ may be derived via simple velocity considerations. As the mean speed $\vec{v_p}$ of ***RV Polarstern*** during the sub time series shown in ***Fig. 3.2*** is given by $22\ km/h$, $\Upsilon = \Gamma \cdot \vec{v_p} = 66\ km$. Υ is rounded down to $60\ km$, bearing in mind that covered distances within three hours may be less during non-transit cruises.

Having set Γ = 3 hours and Υ = $60\ km$ allows for collocating ship- (and consequently also ERA-) to HOAPS-based geophysical parameters (compare ***Table 4***) following the nearest neighbour approach in a final step. Match-ups exceeding Γ and Υ are exclusively omitted.

3.3 Significance Analysis of Correlation Coefficient

In order to assess whether the relationship underlying a regression of two populations A and B is statistically significant, a significance analysis of the Pearson product-moment correlation coefficient ρ is performed (see e.g. ***Snedecor et al.*** (1989)).

ρ assesses the degree that quantitative variables A and B are linearly related in a sample. It is given by

$$\rho_{A,B} = \frac{cov(A,B)}{\sigma_A \cdot \sigma_B} = \frac{E\left[(A-\mu_A)\cdot(B-\mu_B)\right]}{\sigma_A \cdot \sigma_B}, \tag{23}$$

where μ_A and μ_B denote the expected values of A and B and σ_A, σ_B depict their variance, respectively.

Given the best-fit line of the regression analysis ($A = m \cdot B + c$), ρ may be derived from

$$\rho = \frac{m \cdot s_A}{s_B}, \tag{24}$$

in which s_A and s_B represent the standard deviations of the populations A and B. Assuming that no relationship between both time series exists (Nullhypothesis H_0), the test statistic takes on the following form:

$$t = \frac{\rho \cdot \sqrt{n-2}}{\sqrt{1-\rho^2}}, \tag{25}$$

where n specifies the length of A or B[31]. The probability value p is derived using a student's t-test

[31]To be exact, n is not the true physical length, but rather a reduced version of it due to effective degrees of freedom (D.O.F.) considerations. Compare ***Section 3.4.1*** for details.

table, assuming $n - 2$ degrees of freedom (D.O.F.). As no a-priori hypothesis is made as to the sign of the correlation, results are based on two-tailed p-values. In case the chosen significance level α (for 99%, $\alpha = 0.01$) exceeds p, H_0 is rejected and the alternative hypothesis is considered to be true, indicating a significant (to the 99% level) relationship between A and B.

If not further specified, significance tests involving ρ within *Section 4* are based on a 99% level.

There are three primary assumptions underlying the significance tests. These have been tested prior to their application.

1. A true physical relationship between the continuous populations A and B must exist.
2. A and B are drawn from populations that are bivariately normally distributed, implying that a non-linear relationship between A and B can be excluded. Whether this assumption is met was visually examined by means of scatterplots.
3. For any particular A, B is normally distributed about the line and the residual errors are mutually independent, implying that no pattern is resolved among the residuals. This prerequisite was also tested via scatterplots.

The significance of correlation coefficients presented in *Section 4* are based upon so-called *HOAPS 'events'*. An event considers all HOAPS pixels collocated to one (hourly-mean) ship observation, of which non-weighted averages are calculated. Oceanet- and ERA data, to the contrary, contribute with only one single value to each event[32]. The determination of the effective D.O.F. (*Section 3.4.1*) while deriving the test statistic (n in *Eq. 25*) is accounted for in all datasets and displayed as N_{eff} within most Tables in *Section 4*.

3.4 Bias Analysis

3.4.1 Effective Degrees of Freedom

As demonstrated in *Section 3.2*, hourly *RV Polarstern* data exhibits spatial and temporal persistency. This demanded the derivation of integral time- and length scales as thresholds prior to collocation, beyond which statistical dependency may be neglected.

However, decorrelation scales are not only crucial in context of collocation, but also become important when dealing with significances of biases. Serial correlation, as inherent to all parameters shown in *Fig. 3.2*, reduces the effective number of independent observations, i.e. the effective D.O.F. N_{eff} (*Chelton* (1983)). This implies that N_{eff} may be considerably smaller than the length of the time series, which eventually impacts the test statistic expressed by *Eq. 27*[33] (see further down).

[32] This is trivial, as respective data is given in a one hourly resolution.

[33] In *Eq. 27*, N corresponds to N_{eff} = N_{final}. N_{final} is defined in *Eq. 26*

The concept of N_{eff} applies to all datasets underlying this work, necessitating an additional decorrelation analysis of both HOAPS and ERA data within $40° - 60°$ N/S. For convenience, respective results apply to *all* geophysical parameters shown in *Table 4* and are presented in *Table 8*.

Data Source / Scale	Γ	Υ
Oceanet	3 hrs	60 km
HOAPS	7 sec	60 km
ERA	6 hrs	160 km

Table 8: Midlatitudinal ($40°$-$60°$ N/S) decorrelation time- and length scales (Γ and Υ, respectively), the derivation of which is of need prior to the analysis of bias significance. Compare *Section 3.2* for the derivation of Oceanet-based decorrelation scales. The HOAPS-based Γ represents an average of ten case studies. The corresponding Υ was determined subsequently, keeping in mind the speed of the SSM/I to be $6.58\ km/s$. ERA-based Γ and Υ result from eight case studies, each of which underlie the assumption of zonal propagation only.

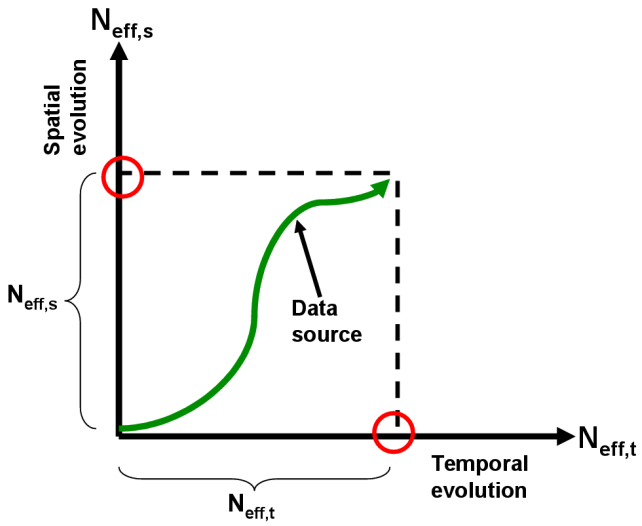

Fig. 3.3: Illustration of the time-space domain evolution characterizing underlying datasets of *RV Polarstern*, HOAPS, and ERA. The green arrow exemplarily represents the behaviour of *RV Polarstern* in time and space (can be replaced by straight arrows in case of HOAPS / ERA), whereas the red circles depict the resulting components of $N_{eff,t}$ and $N_{eff,s}$. The origin of co-ordinates represents the initial point of the time series, whereas the tip of the arrow depicts its respective end. See text for further details.

N_{eff} may be decomposed into two individual components, namely *temporal* and *spatial* N_{eff}.

Following an approach by *Leith* (1973), *Trenberth* (1985) argues that $N_{eff,t} = \frac{N\Delta t}{T_0}$, where $N_{eff,t}$ refers to the effective *temporal* D.O.F., N represents the length of the time series, Δt the sampling interval, and T_0 the effective time between independent samples[34]. *Bretherton et al.* (1999), on the other hand, considers the effective number of *spatial* D.O.F. in context of time-varying fields and recalls that $N = N_{eff,s} = \frac{N}{2L}$, where N denotes the amount of contiguous, equally spaced grid points, N the amount of respective independent values and $2L$ the distance between independent observations.

Here, an ultimate combination of both is chosen in the following form

$$N_{final} = N_{eff} = \sqrt{N_{eff,t}^2 + N_{eff,s}^2} \qquad (26)$$

Fig. 3.3 exemplarily visualizes *Eq. 26* in form of a two-dimensional time-space diagram, where the data source is considered to be *RV Polarstern*. Assuming a slightly varying ship speed in time, illustrated by the twisting green arrow, *RV Polarstern* covers an increasing distance with proceeding time, associated with an increase of $N_{eff,t}$ and $N_{eff,s}$. Presuming the current position of the ship to be at the

[34] This corresponds to the decorrelation time scale.

tip of the arrow, both $N_{eff,t}$ and $N_{eff,s}$ can be determined separately, as indicated by the red circles. Applying Pythagoras' Theorem allows for deriving the N_{final} (approximately corresponding to the length of the arrow), which exceeds both $N_{eff,t}$ and $N_{eff,s}$, but not their sum.

One could argue that a simple summation of $N_{eff,t}$ and $N_{eff,s}$ was more appropriate. The latter would contribute to a more generous significance testing, as N_{final} ($\hat{=}$ N=N_{eff} in *Eq. 27*) would be larger than indicated in *Eq. 26*. The difference of both approaches, however, is considered to have a minor impact on the bias results, which justifies the use of *Eq. 26* within bias considerations in *Section 4*.

3.4.2 Significance of Biases

The significance of biases, constituting a major component of *Section 4*, is mainly based on different data sources, necessitating the application of a two-sample t-test for paired differences. This choice is legitimate, as both datasets are independent from each other and their intrinsic dependency is accounted for by calculating individual effective D.O.F. (compare *Section 3.4.1*). For the sake of consistency, N in *Eq. 27* is associated with the *smaller* N_{eff}, in case their individual N_{eff} differ from each other. This approach is more restrictive, in as much as t in *Eq. 27* remains comparatively small, implying a less generous rejection of H_0.

Here, the Null-Hypothesis is given by $H_0 : \mu_A = \mu_B$, where μ_A and μ_B represent the expected values of the populations A and B, underlying the assumption of equal variances, i.e. $\sigma_A^2 = \sigma_B^2$. Assuming the mean of the paired differences, a, to be zero, the test statistic takes on the following form:

$$t = \frac{\overline{x_D} - a}{s_D/\sqrt{N}}, \tag{27}$$

where N are the effective D.O.F., x_D and s_D represent the mean difference of A and B and its standard deviation, respectively. Under the Null hypothesis, t is t-distributed with $N-1$ D.O.F. If not indicated separately, α is chosen to be 0.05, i.e. illustrated biases in *Section 4* are significant at the 95% level.

In context of significant biases between HOAPS and Oceanet illustrated in *Section 4*, individual grid boxes resolve arithmetic mean biases of HOAPS 'events' (see *Section 3.4.1* for an explanation). This also accounts for the bias plots involving ERA (compare *Appendix, A. 4* and *A. 5*).

4 Validation Results

4.1 Intercomparison of the Two Bulk Algorithm LHF Outputs

Prior to validating HOAPS LHF, both Coare- and Oceanet-based flux algorithm outputs are opposed to quantify similarities and regional weaknesses. Based on this confrontation, one of the algorithms is chosen as the sole in-situ validation data source within proceeding analyses.

Fig. 4.1 (left) illustrates a scatterplot of all available hourly Coare- and Oceanet-based LHF, where the red line represents the angle bisector associated with a correlation coefficient of 1. Overall, LHF pairs range between $-80\ W/m^2$ (negative LHF $\triangleq$ flux into the ocean, accounting for 9.6% of all pairs) and $485\ W/m^2$ (vice versa). Both LHF products agree exceptionally well, which also applies to the boundary ranges.

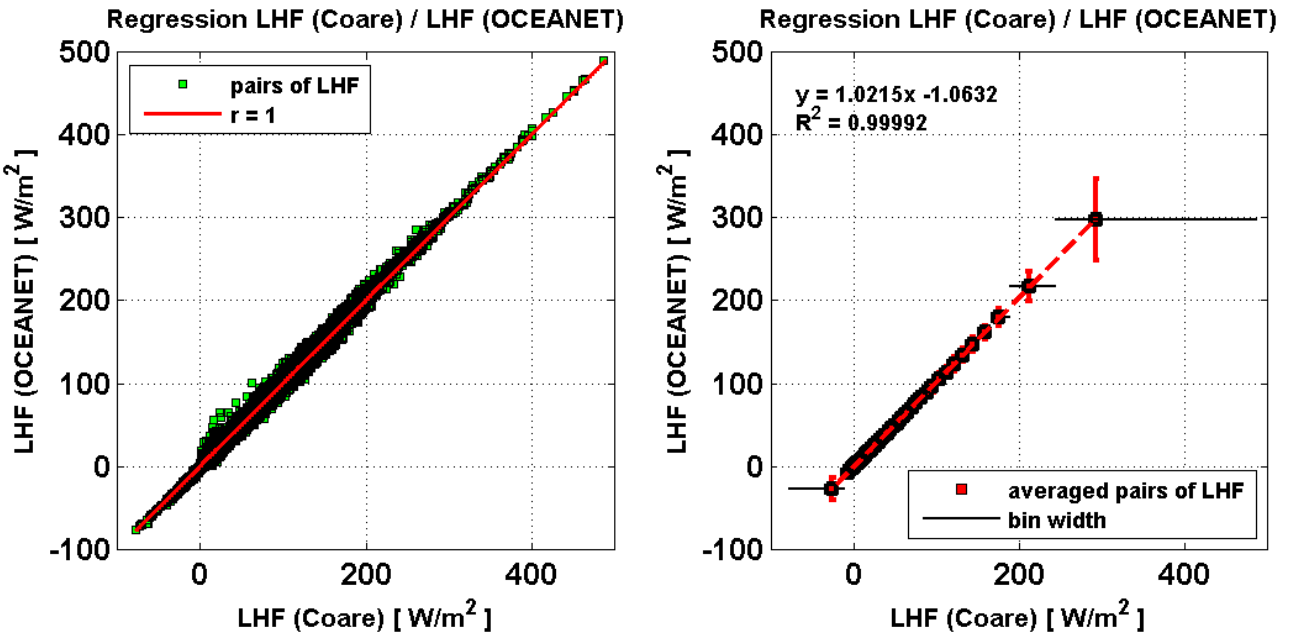

Fig. 4.1: Left: Scatterplot of all available pairs of hourly Coare (x-axis) - and Oceanet-based (y-axis) LHF. The red line represents the perfect correlation reference.
Right: Regression of bin-averaged LHF (medians) of hourly Coare (x-axis) - and Oceanet-based (y-axis) LHF. The red line represents the best fit and the vertical bars correspond to 1 std into each direction. R^2 represents the variance explained by the linear best-fit line. The black horizontal lines indicate the width of the bins, over which medians were calculated.

The slightly elevated spread for LHF between $0\ W/m^2$ and $200\ W/m^2$ can be attributed to the fact that $\approx 87\%$ of LHF lie within this range, which increases the probability of outliers.

Fig. 4.1 (right) visualizes a regression of both parameters, based on bin-averages, each of which are composed of 250 single pairs. These bin widths are fairly large in the region of extreme LHF, involving elevated standard deviations (std) associated with the arithmetic means. The striking relationship is confirmed by a correlation coefficient exceeding 0.99, which is statistically significant at the 99% level.

Table 9 includes results from a more extensive statistical approach, summarizing the confrontation of both flux products. A geographical differentiation is made to resolve unique features of individual latitudinal bands. Largest positive LHF, exceeding $100\ W/m^2$ on average, are confined to the (sub-)tropics of the southern Atlantic. As to be expected, LHF continuously decrease towards higher latitudes. The bias of both flux products does not exceed an absolute value of $3.5\ W/m^2$ (northern / southern (sub-)tropics) and respective relative deviations are restricted to 4%. On a global scale, the bias is not statistically significant at the 95% level. Compared to Coare output, Oceanet-based LHF remain slightly larger, which confirms previous findings (Bumke, pers. comm., May 2013).

$region$	$pairs$	N_{eff}	$\overline{LHF}_C$	$\widetilde{LHF}_C$	std_C	$\overline{LHF}_O$	$\widetilde{LHF}_O$	std_O	$corr$	$bias$	$dev.[\%]$	std_D	$RMSE$
78°S - 82°N	11458	8236	54.01	32.00	62.90	54.11	31.03	64.42	0.998*	-0.10	-0.19	4.98	4.99
60°S - 78°S	3375	2425	24.29	18.12	24.58	21.78	15.50	23.47	0.996*	2.51*	10.91	2.46	3.52
40°S - 60°S	2622	1792	36.97	18.07	58.68	36.95	17.84	59.58	0.999*	0.03	0.07	2.94	2.94
20°S - 40°S	1176	809	131.51	128.35	88.95	134.26	128.58	90.38	0.997*	-2.76*	-2.08	7.31	7.82
0° - 20°S	553	401	123.99	116.68	45.44	127.34	119.46	47.07	0.986*	-3.35*	-2.67	8.03	8.70
0° - 20°N	488	348	98.38	96.17	46.25	99.82	97.20	48.33	0.986*	-1.44*	-1.46	8.13	8.26
20°N - 40°N	513	362	82.88	81.74	37.21	86.28	83.98	37.87	0.979*	-3.41*	-4.03	7.77	8.48
40°N - 60°N	733	537	78.56	65.50	61.57	80.31	68.07	62.63	0.997*	-1.75*	-2.20	5.13	5.42
60°N - 82°N	1998	1626	34.30	20.85	39.91	34.74	21.57	40.00	0.998*	-0.44*	-1.26	2.72	2.76

Table 9: Summary of statistical indices comparing LHF originating from both Coare and Oceanet algorithm. The first row gives a global statistic, whereas the focus of all other rows lies on latitudinal bands to account for regional differences. The subscript C denotes 'Coare', O refers to 'Oceanet', and D to their LHF difference. Arithmetic means and medians are expressed by the overline and tilde, respectively. RMSE represents the root-mean-square error. Positive biases mirror larger Coare-based LHF compared to the Oceanet counterpart. Asterisks indicate statistical significance at the 95% level (bias) and 99% level (correlation coefficient). Significance testing of the correlation coefficient 'corr' and the bias is based on a paired-differences t-test, where the reduction of D.O.F. to N_{eff} (*Column 3*) is fully accounted for.

$region$	$pairs$	N_{eff}	$\overline{LHF}_C$	$\widetilde{LHF}_C$	std_C	$\overline{LHF}_O$	$\widetilde{LHF}_O$	std_O	$corr$	$bias$	$dev.[\%]$	std_D	$RMSE$
78°S - 82°N	3307	2348	99.97	92.35	67.24	102.47	94.68	68.65	0.995*	-2.50*	-2.47	7.01	7.53
60°S - 78°S	0	n.a.	n.a.	n.a.	n.a.	n.a.	n.a.	n.a.	n.a.	n.a.	n.a.	n.a.	n.a.
40°S - 60°S	393	291	61.29	44.85	66.60	62.21	44.21	67.82	0.999*	-0.92*	-1.49	3.40	3.52
20°S - 40°S	731	503	129.69	118.19	91.30	133.20	119.11	92.52	0.997*	-3.51*	-2.69	7.73	8.49
0°S - 20°S	553	401	123.98	116.68	45.44	127.34	119.46	47.07	0.986*	-3.35*	-2.67	8.03	8.70
0°N - 20°N	488	348	98.38	96.17	46.25	99.82	97.20	48.33	0.986*	-1.44*	-1.46	8.13	8.26
20°N - 40°N	513	362	82.88	81.74	37.21	86.28	83.98	37.87	0.979*	-3.41*	-4.03	7.77	8.48
40°N - 60°N	537	407	83.36	75.64	62.60	85.21	78.07	63.55	0.996*	-1.85*	-2.19	5.37	5.67
60°N - 82°N	92	90	85.25	80.84	53.49	85.77	80.27	55.15	0.999*	-0.52	-0.61	2.76	2.81

Table 10: As in *Table 9*, but restricted to the six Atlantic transit cruises (compare *Table 1*).

However, the relative bias is considerably larger in the southern (sub-)polar regions (it equals to a mean of $\approx 11\%$ relative deviation) and its absolute value is statistically significant, where Coare-based LHF tend to be systematically larger than respective Oceanet outputs. Whereas the comparatively

large relative offset is misleading due to small absolute LHF[35], the bias sign is rather exceptional, in as much as Oceanet-based LHF generally exceed those produced by Coare.

Table 10 provides identical statistical parameters, restricted to the six transit cruises (compare *Table 1*). Although this consideration reduces the hourly RV Polarstern dataset by 71%, remaining transit measurements were most likely obtained during a constant ship speed (which minimises contamination errors due to flow distortion) and excludes the (sub-)polar latitudes. As to be expected, mean fluxes are considerably larger during these cruise legs, as high-latitudinal, mostly low LHF are not accounted for. Bias analysis within this context reveals that Oceanet LHF are systematically larger than Coare fluxes, reinforcing the trend observed in *Table 9*. As no southern hemispheric subpolar data sampling occurred during the transits, the equivalent positive bias as seen in *Table 9* cannot be resolved, contributing to a basin-wide negative bias of $-2.5\ W/m^2$.

Fig. 4.2 (left) illustrates the arithmetic mean LHF along the cruise track, based on the Oceanet algorithm. Shadings correspond to grid box averages of a 1° x 1° resolution. As could already be extracted from *Table 9*, the LHF gradient between tropical and polar latitudes is well resolved and polar LHF remain damped. As has been observed by *Bentamy et al.* (2003), lowest LHF are found in the high northern latitudes during summer months, owing to the frequent occurrence of fog associated with warm air flowing northward over cold waters .

Furthermore, the striking flux maxima near 40°S, which locally exceed $440\ W/m^2$ (off Uruguay (west Brazil-Malvinas confluence) and South Africa (Agulhas retroflection)), are clearly visible (compare *Fig. 1.2*). Northern hemispheric maxima are located off the Norwegian Coast close to the Arctic Circle. Whereas *Table 9* lists biases and their significance associated with latitudinal bands, *Fig. 4.2* (right) shows the spatial distribution of significant LHF biases. Results of a paired differences t-test suggest that 34% of LHF biases between Coare- and Oceanet are significant at the 95% level. Blue shading north of 40°N is evident in more than 66% of grid boxes containing data, indicating larger Oceanet LHF compared to the Coare counterpart. Largest absolute biases are located northwest of South Africa (up to $-24\ W/m^2$). In contrast, as seen in *Table 9*, Coare-based fluxes are considerably larger off the Antarctic Continent than the Oceanet complement (as much as $16\ W/m^2$), giving rise to 46% of significant biases at the 95% level south of 60°S.

Despite regional significant biases between both flux algorithm outputs, linked to a persistent LHF over- or underestimation, percental deviations during all cruises (and transits only) are strongly limited (exception: southern subpolar region, see *Table 9*) and correlation coefficients are close to 1. Owing to persistently small std_D, *Eq. 27* suggests an increased probability of resolving significant biases. The latter is verified by the statistical significance of most latitudinal-mean biases (compare *Table 9* and *Table 10*). Given Oceanet-based LHF would thus allow for reliably predicting the spatial distribution and latitudinal averages of the Coare-match, for example.

Recalling this forecast potential and the overall outstanding agreement of Coare- and Oceanet

[35] On a global scale, the absolute bias south of 60°S is smallest compared to all other latitudinal bands.

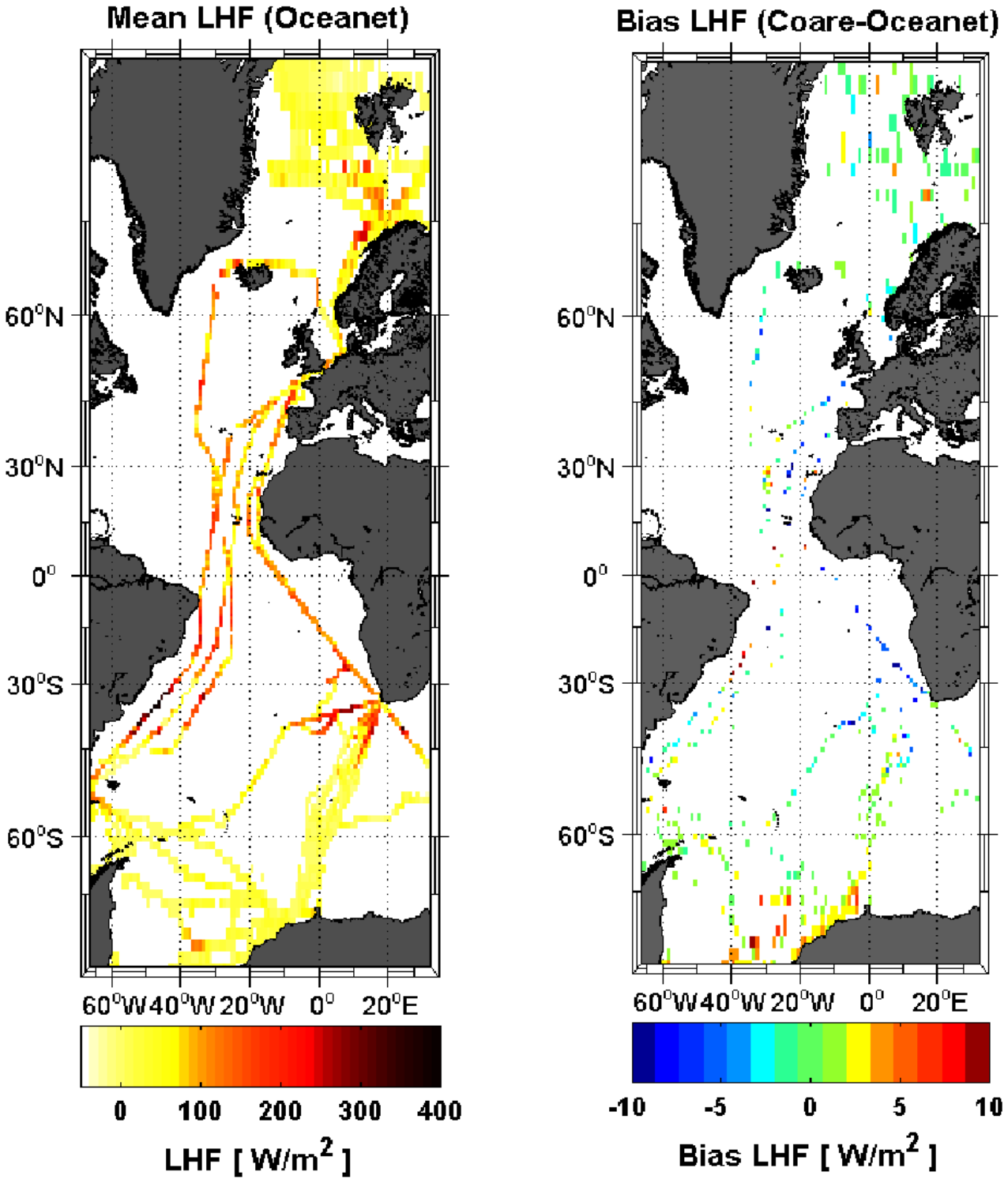

Fig. 4.2: **Left**: Illustration of the arithmetic means of Oceanet-LHF on a regular $1^\circ \times 1^\circ$ grid. Values range from $-70\ W/m^2$ in high latitudes to $480\ W/m^2$ locally off Uruguay and South Africa.
Right: Significant LHF biases (Coare - Oceanet), the magnitude of which is indicated by the shading.

LHF (despite the fact that both codes are based on independent measurements) allow for restricting the HOAPS LHF validation to only one algorithm-based flux product, as the simultaneous consideration of both does not introduce new information.

Within this work, the Oceanet LHF parameterization is chosen to constitute the comprehensive 'ground-truth' reference to the HOAPS time series and Coare fluxes are not considered within the following chapters.

4.2 Quantification of LHF Biases Between HOAPS, Oceanet, and ERA

Fig. 4.3 illustrates the latitudinal dependency of LHF based on all three flux data products, namely Oceanet, HOAPS, and ERA.

Mean minima below 20 W/m^2 are restricted to the southern hemispheric polar ocean, whereas a gradual increase of LHF occurs equatorwards on both hemispheres. The mid-latitudes, especially in the southern hemisphere, are characterized by pronounced LHF gradients, mirrored in largest standard deviations, which range between $80 - 90$ W/m^2. *Fig. 4.3* suggests that LHF maximise within the southern extratropics (20°-40°S), where data source-dependent means of $116 - 134$ W/m^2 occur within the transition zone to the mid-latitudes. Apart from minor exceptions, Oceanet LHF exceeding 300 W/m^2 or even 400 W/m^2 are located within this latitudinal band on both western and eastern side of the Atlantic basin (compare local hot spots southwest of RSA and off Uruguay, *Fig. 4.2*, left), which generally speaking also accounts for ERA- (*Appendix, Fig. A. 1*, bottom right) and HOAPS-based LHF (compare *Fig. 4.5*, top right).

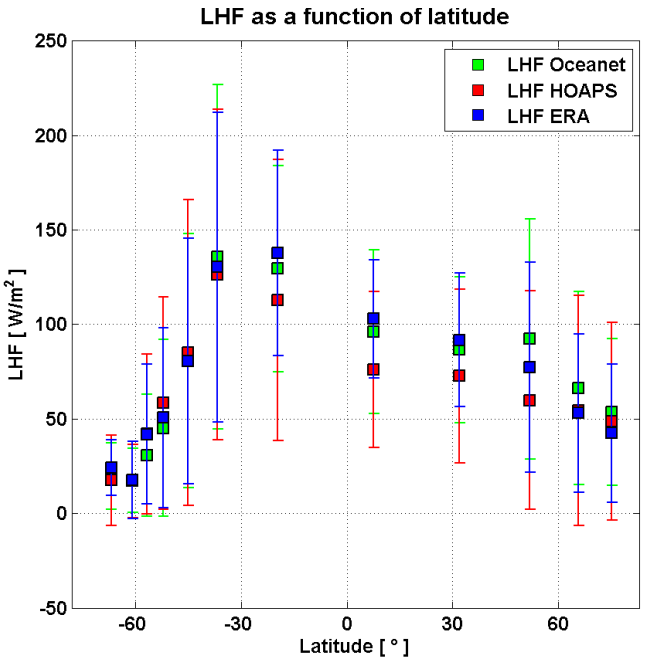

Fig. 4.3: LHF data products as a function of latitude. Boxes are based on arithmetic means of 300 individual values, which itself correspond to HOAPS 'events' (compare *Section 3.3*). Vertical bars indicate 1std, respectively. Events involving no HOAPS data availability were subject to prior exclusion. Additionally, events exhibiting negative LHF within the Oceanet- and ERA LHF have been neglected for consistency with the HOAPS dataset, which does not resolve LHF below 0 W/m^2.

Owing to the southern hemispheric absolute maximum, the distribution is consequently slightly asymmetric, as a local second maximum in low northern latitudes is not resolved.

Fig. 4.3 indicates that HOAPS LHF are, in an absolute sense, considerably underestimated within the subtropics and further equatorwards, which has been extensively discussed among LHF intercomparison studies of various satellite- and reanalysis-based flux products focusing on both winter- and summer hemispheres (*Kubota et al.* (2003), *Chou et al.* (2003), compare *Section 5.2.1* for discussion).

Amongst others, this underrepresentation is quantified within *Table 11* , which displays a latitudinal-dependent statistical tabulation of the Oceanet- and HOAPS-based LHF. As is depicted, the mean absolute offset between 20° N/S amounts to $-20.2\ W/m^2$, corresponding to -18.4%. Albeit of being statistical significant, the related correlation coefficient of 0.46 represents a regional minimum.

As is apparent in *Fig. 4.3*, HOAPS LHF are underestimated to a large extend within the entire Atlantic basin. These negative biases between within 40°S-60°N are statistically significant and range between $-10.3\ W/m^2$ (20°-40°S) and as much as $-27.5\ W/m^2$ (40°-60°N). A relation to absolute fluxes yields mean relative deviations of -7.8% and -34.4%, respectively. The basin-scale significant bias of $-7.6\ W/m^2$ (-11.7%) remains rather low, owing to the comprehensive data availability within the (sub-)polar regions (compare *Column 2* in *Table 11* / *Table 12*), which are subject to small absolute LHF (means of $13.2\ W/m^2$ south of 60°S, e.g.).

Southern hemispheric mid-latitudes represent an exception, in as much as the sign of the bias is reversed and HOAPS-based LHF are approximately $6.1\ W/m^2$ larger (12.5%) compared to the Oceanet output.

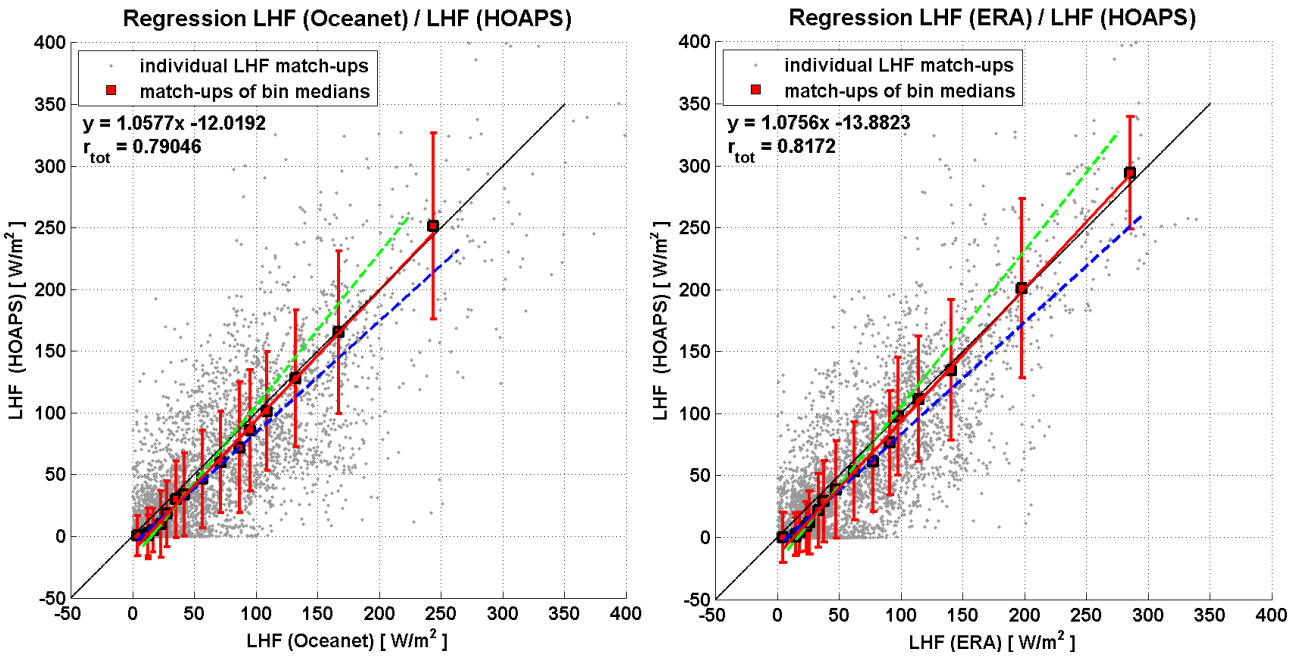

Fig. 4.4: Left: Results of a two-sided orthogonal regression (red line) of Oceanet- and HOAPS-based LHF. Red boxes correspond to median values based on 250 individual HOAPS events, respectively. Exemplarily, blue (green) dashed lines represent the single linear regression lines from Oceanet- to HOAPS LHF (vice versa). Red vertical bars indicate 1 std associated with the HOAPS medians. r_{tot} corresponds to the correlation coefficient when considering all individual LHF pairs (grey dots). The black angle bisector represents the reference of a hypothetical perfect correlation.
Right: Same as left, but two-sided orthogonal regression of HOAPS- and ERA-based LHF.

Fig. 4.4 (left) illustrates the results of a two-sided orthogonal regression (red line) of Oceanet- and HOAPS LHF. As an indication, both green and blue dashed best-fit lines correspond to the individual, one-sided regressions, whereas the black angle bisector constitutes the hypothetical perfect correlation. The latter intersects the best-fit fit close to $200\ W/m^2$, below which mean Oceanet LHF

exceed the respective HOAPS counterpart, which mirrors the systematic LHF underestimation of the HOAPS dataset. Although absolute LHF values are comparably small within the southern polar ocean (compare *Fig. 4.3*), the negative offset of $-12\ W/m^2$ given by the best-fit line reflects that relative deviations may be of high order. As r_{tot} indicates, the regression line explains 62% of the overall variance.

A restriction to transit data analysis (not shown) is associated with an Atlantic mean bias of $-14.5\ W/m^2$ (-14.6%, based on basin-mean HOAPS LHF of $85\ W/m^2$) and indicates similar relative deviations between $40°$S-$60°$N (-10.9% to -30.4%) as well as 10.7% between $40°$-$60°$S. However, a strong positive bias of $22.5\ W/m^2$ is also evident north of $60°$N, which is associated with only one cruise in the vicinity of Iceland (as is indicated by red shadings in *Fig. 4.5* (bottom left)) and is thus not of statistical significance.

To localize hot spots of mean HOAPS LHF and their deviations to the Oceanet reference within the investigation area, *Fig. 4.5* (top) depicts absolute HOAPS-based LHF in a $1°$ x $1°$ resolution, to which *Fig. 4.2* serves as a comparison. Owing to the high resolution, a separation of both hemispheres is performed, which facilitates the recognition of noteworthy features.

Lying the focus on the northern hemisphere (*Fig. 4.5*, top left), LHF maxima exceeding $200\ W/m^2$ are located within the Barents Sea region and in the vicinity of Iceland.

Within southern latitudes (*Fig. 4.5*, top right), several exceptionally high LHF are detected along the transit cruise track to Punta Arenas ($0°$-$20°$S, $35°$-$40°$S) and locally south(-west) of RSA ($25°$-$45°$S), partly exceeding $300\ W/m^2$. These LHF maxima, associated with the west Brazil-Malvinas confluence and the Agulhas retroflection, are locally isolated, associated with large spatial gradients and thus a peak within root-mean-square error (RMSE) between $20°$-$40°$S (compare *Table 11*). Faint colors within the subpolar southern ocean mirror small absolute LHF, similar to findings in context of *Fig. 4.2* (left).

In order to detect geographical locations associated with systematic LHF deviations illustrated in *Fig. 4.3*, *Fig. 4.5* (bottom) illustrates significant biases between Oceanet- and HOAPS-pairs. Overall, these biases account for 42% of all observed deviations and remain negative to 65%, implying a more frequent LHF underestimation of the HOAPS dataset compared to the Oceanet flux algorithm output.

As mirrored in *Fig. 4.3*, biases averaged over the northern hemispheric extratropics tend to be negative (in 76% of all cases) and take on extremes off Norway ($70°$N), locally exceeding $-100\ W/m^2$. Here, HOAPS significantly underestimates LHF, which exceed $200\ W/m^2$ according to Oceanet LHF. Local negative deviations extend further south towards the German coast of the North Sea. Concurrent significant positive maxima of approximately $60\ W/m^2$ are evident close to Iceland, associated with exceptionally high HOAPS-based LHF mentioned in context of *Fig. 4.5* (top). These maxima are however poorly resolved in *Fig. 4.3*, as they are locally confined and masked by the frequent LHF underestimations near the Norwegian coast and further north(-west).

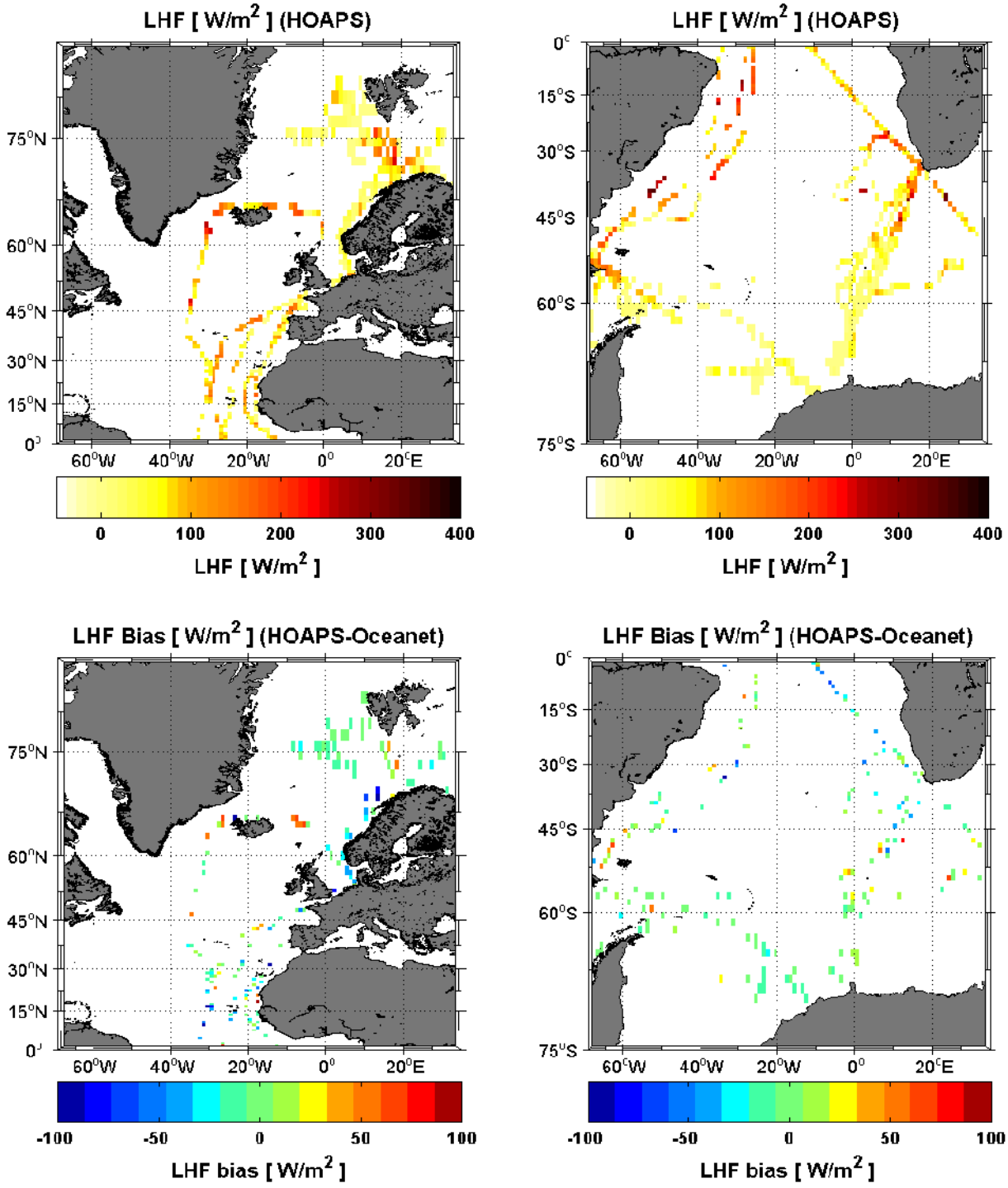

0.9

Fig. 4.5: Top left/right: Map (1° x 1° resolution) of mean HOAPS LHF based on HOAPS 'events' (*Section 3.3*). **Bottom left/right:** Map (1° x 1° resolution) of significant (at the 95% level) biases between Oceanet- and HOAPS-LHF based on HOAPS 'events' (*Section 3.3*). Positive values indicate a flux overestimation of HOAPS.

Hot spots of significant negative biases are also resolved along the transit cruise track (locally exceeding $-50\ W/m^2$ to $-100\ W/m^2$) to Capetown as well as southwest of RSA ($\approx -70\ W/m^2$) (*Fig. 4.5*, bottom right). As suggested by *Fig. 4.3*, the mean bias between (30°S-30°N) maximises in an absolute sense ($-27.9\ W/m^2$, -19.6%).

Overall, negative deviations occur twice as much as their positive counterpart, given Oceanet-LHF exceeding $100\ W/m^2$. Likewise, these biases are almost exclusively negative along the southeastern Atlantic transit cruise track connecting Bremerhaven and Capetown.

In contrast, as is indicated in *Fig. 4.3*, HOAPS overestimates LHF to 66% in a latitudinal band spanning $45°$-$60°$S, causing a mean bias of $9\ W/m^2$. Mean deviations further south tend to be negative (to 75%), albeit not of statistical significance (compare *Table 11*).

The latitudinal bias distribution between the HOAPS- and ERA output (refer to *Appendix, A. 4*, top) closely resembles the pattern shown in *Fig. 4.5* (bottom), including amongst others similar bias magnitudes off Norway and close to Iceland (not shown).

However, a few distinct differences shall be briefly pointed out. As implied by *Fig. 4.3*, ERA tropical LHF exceed those of Oceanet and HOAPS, leading to an even enhanced mean bias of $-24\ W/m^2$ between 20°S-40°N (-25.3%) when comparing HOAPS- to ERA LHF output. These findings are confirmed within *Kubota et al.* (2003), pointing out the unexpectedly large LHF of the ECMWF forecast model in the equatorial region (compare *Section 5.2.1* for discussion).

$region$	$events$	N_{eff}	$\overline{LHF}_O$	std_O	$\overline{LHF}_H$	std_H	$corr$	$bias$	$dev.[\%]$	$RMSE$
$78°S$ - $82°N$	4012	680	64.90	62.85	57.30	64.95	0.80*	-7.62*	-11.73	41.65
$60°S$ - $78°S$	721	78	15.60	16.39	12.68	19.84	0.61*	-2.93	-18.75	16.52
$40°S$ - $60°S$	1095	189	48.35	55.13	54.38	64.54	0.82*	6.02*	12.46	37.65
$20°S$ - $40°S$	428	109	131.74	80.83	121.54	81.08	0.76*	-10.34*	-7.74	56.76
$0°S$ - $20°S$	200	62	125.92	49.16	106.25	70.60	0.71*	-19.91*	-15.62	53.40
$0°N$ - $20°N$	238	55	96.64	45.89	76.66	43.40	0.46*	-20.01*	-20.67	50.78
$20°N$ - $40°N$	262	66	88.04	36.58	72.10	42.12	0.51*	-15.99*	-18.10	42.41
$40°N$ - $60°N$	405	70	80.48	62.28	52.80	58.19	0.77*	-27.54*	-34.40	49.56
$60°N$ - $82°N$	663	72	54.28	45.61	44.67	55.89	0.68*	-9.66	-17.71	42.57

Table 11: As in *Table 9*, but comparing statistical parameters associated with Oceanet- and HOAPS-based LHF. Subscripts 'O' and 'H' refer to Oceanet and HOAPS, respectively. 'x events' indicates that statistics are based on x HOAPS events (*Section 3.3*), similar to 'pairs' in *Table 9*. Medians and std_D have been omitted.

Furthermore, (sub-)polar northern hemispheric LHF biases remain negligible (*Table 12*), in contrast to the intercomparison between Oceanet and HOAPS.

Overall, latitudinally-mean significant biases are exclusively negative, which also represent a difference to results shown in *Table 11*.

region	*events*	N_{eff}	$\overline{LHF}_E$	std_E	$\overline{LHF}_H$	std_H	*corr*	*bias*	*dev.*[%]	*RMSE*
$78°S$ - $82°N$	4014	717	65.57	59.21	57.47	64.81	0.82*	-8.11*	-12.35	38.73
$60°S$ - $78°S$	660	73	19.28	16.33	13.20	20.31	0.53*	-6.09*	-31.55	19.12
$40°S$ - $60°S$	1166	203	52.47	53.04	51.94	63.36	0.81*	-0.54	-1.01	36.78
$20°S$ - $40°S$	427	112	133.01	73.16	122.05	80.55	0.77*	-11.09*	-8.24	54.03
$00°S$ - $20°S$	199	54	129.15	44.96	106.25	70.60	0.83*	-23.22*	-17.73	47.80
$00°N$ - $20°N$	237	57	103.09	33.07	76.66	43.40	0.41*	-26.47*	-25.64	50.16
$20°N$ - $40°N$	261	66	94.18	31.27	72.10	42.12	0.71*	-22.05*	-23.45	36.98
$40°N$ - $60°N$	408	81	69.16	55.17	52.28	58.13	0.84*	-16.94*	-24.41	36.38
$60°N$ - $82°N$	649	73	44.66	38.45	45.54	56.18	0.72*	0.84	1.97	39.25

Table 12: As in *Table 11*, but comparing statistics involving ERA- and HOAPS-LHF, respectively. The subscript 'E' denotes ERA.

Owing to the striking similarity between Oceanet- and ERA output, the basin-wide offset between HOAPS and ERA amounts to $-8.1\ W/m^2$ (-12.4%), which becomes $-16\ W/m^2$ (-16.0%) when the analysis is restricted to transit cruises only (not shown).

Due to the extensive time series, correlation coefficients listed in *Table 11* and *Table 12* are significant to the 99% level and the regression performed above suggests an overall satisfying agreement of all three data sources.

However, the two-dimensional spatial analysis shown above indicates that locally enormous biases characterize the confrontation of HOAPS-LHF to both validation sources. Depending on the geographical region, this impression may even be spatially comprehensive (in contrast to local hot spots off Iceland, e.g.), considering for example area-wide deviations along the transit cruise track to RSA as well as northwest of Norway. As respective offsets differ in magnitude and relative contribution to absolute LHF substantially vary, simple conclusions concerning an overall bias pattern cannot be drawn, which would considerably facilitate a bias correction of the HOAPS dataset and concurrently an overall assessment of its importance as a reliable satellite-based dataset.

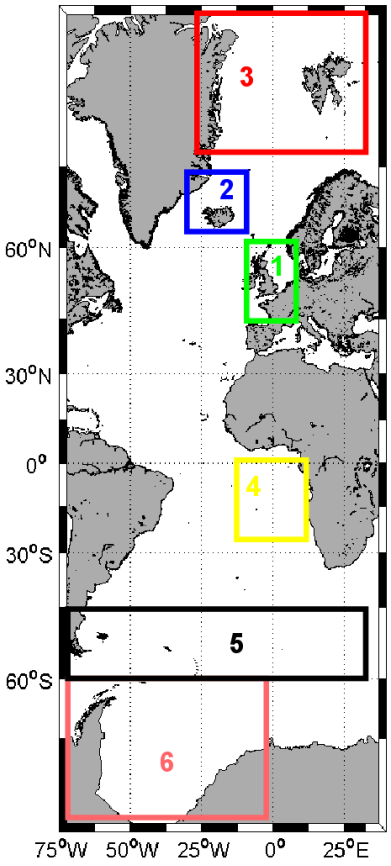

Fig. 4.6: Coloured frames indicate regions, the LHF biases of which are investigated separately with respect to their sources. Refer to text for further details.

The question remains as to why the above-discussed considerable deviations of HOAPS-LHF to corresponding Oceanet- and ERA-output exist.

This problem serves as a motivation to draw the attention to bias fields of several geophysical parameters, on which LHF eventually depends. According to *Eq. 8*, these parameters comprise $\vec{u}$ (directly impacting C_e, see *Eq. 19a*), q_a, and q_s[36]. Furthermore, LHF crucially depends on L_e, which itself is temperature-dependent. Consequently, SST will serve as the fourth parameter, all of which are investigated separately within *Sections* 4.3 - 4.5 as to their different representations within the three data sources.

Apart from differentiating between latitudinal bands, the following thoughts will also focus on geographically confined regions, which according to *Fig. 4.5* (bottom) are partially subject to considerable LHF biases and incorporate polar areas. According to *Table 11* and *Table 12*, these polar LHF biases are not of statistical significance, which will be tested for among the restricted areas.

These bias hotspots comprise the following domains, which are enframed in *Fig. 4.6*:

1. North Sea ($45°$-$60°$N / $5°$W-$10°$E). Map: green.
2. Iceland ($63°$-$68°$N / $8°$-$30°$W). Map: blue.
3. Arctic ($72°$-$82°$N / $25°$W-$35°$E). Map: red.
4. RSA southern transit ($0°$-$25°$S / $10°$W-$15°$E). Map: yellow.
5. Southern mid-latitudes ($45°$-$60°$S). Map: black.
6. Southern polar ocean ($60°$-$78°$S / $0°$-$69°$W). Map: pink.

To decode their origin, these LHF will undergo a separate parameter-based investigation, which will be gradually supplemented. The case studies also aim to demonstrate that regionally confined biases are fraught with uncertainty owing to low D.O.F. and may thus not be significant.

Table 13 lists LHF statistics for the above-listed domains based on a comparison of HOAPS- to Oceanet data.

Reg.	Lat	Lon	$Events$	$\overline{LHF_H}$	$Bias$	$Dev.[\%]$
1	$45-60°N$	$5°W$ - $10°E$	305	42.27	-30.68*	-42.02
2	$63-68°N$	$8-30°W$	32	119.3	18.60	16.27
3	$72-82°N$	$25°W$ - $35°E$	271	39.38	-4.6	-11.26
4	$0-25°S$	$10°W$ - $35°E$	122	71.89	-39.03*	-34.79
5	$45-60°S$	$69°W$ - $35°E$	902	47.24	10.01*	26.88
6	$60-78°S$	$69°W$ - $0°E$	665	12.37	-3.27	-20.90

Table 13: Confrontation of LHF biases between HOAPS and Oceanet within six domains (Reg.) which are indicated in *Fig. 4.6*. Nomenclature as in *Table 11*. Biases are given with respect to Oceanet.

[36]The Oceanet algorithm allows for determining the stability-dependent $\vec{u}$ and q_a at 10 m ASL to allow for direct intercomparisons with HOAPS- and ERA-based parameters (both 10 m ASL)

4.3 Quantification of $\vec{u}$ Biases Between HOAPS, Oceanet, and ERA

Fig. 4.7 illustrates the two-sided orthogonal regressions involving absolute wind speed (10 m ASL) between HOAPS and Oceanet (left) / ERA (right), respectively.

Mean wind speeds remain between $2.2 - 16.2\ m/s$ (Oceanet), $3.0 - 17.0\ m/s$ (HOAPS), and $2.4 - 14.7\ m/s$ (ERA), respectively.

On average, the HOAPS wind speed product slightly underestimates the high wind regime (means exceeding $12\ m/s$) by $0.21\ m/s$ (-1.5%), whereas lighter wind speeds are overrepresented, as indicated by the red best-fit line.

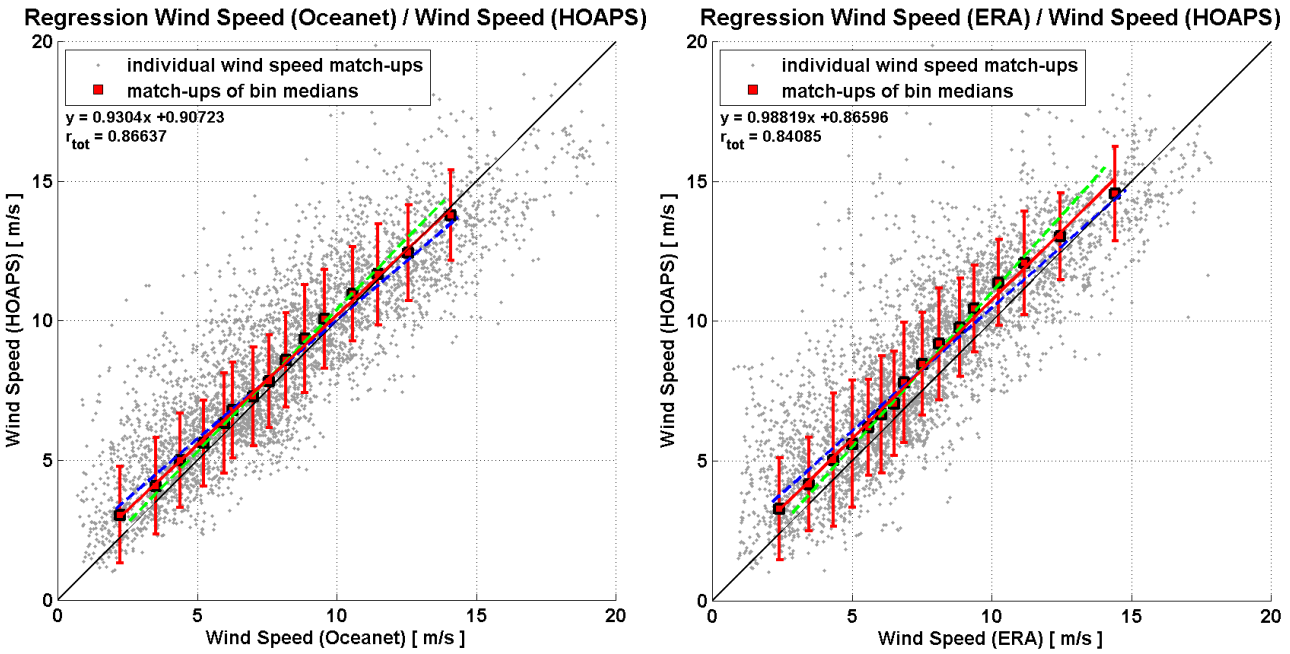

Fig. 4.7: As in *Fig. 4.4*, but showing two-sided orthogonal regression of (**left**) Oceanet- and HOAPS-based $\vec{u}$ (10 m ASL) and (**right**) ERA- and HOAPS-based $\vec{u}$ (10 m ASL).

The transition between over- and underrepresentation shifts to $8\ m/s$ when restricting the analysis to transit cruises only (not shown), which is linked to an Atlantic mean bias reduction by a factor of 3.9, suggesting that most significant biases are to be located within the (sub-)polar ocean basins. The mean relative deviation of 18% below $5\ m/s$ is considerable, yet only corresponds to an average bias of $0.69\ m/s$. *Fig. 4.7* (right) indicates that a comparison of HOAPS- to ERA-based wind speeds even enhances the systematic deviation, as suggested by the slope and offset of the best-fit line. Consequently, a mean positive offset of $0.87\ m/s$ results, associated with elevated relative deviations in low wind regimes. Similar to Oceanet, a confinement to transit data reduces the mean offset, resulting in a basin-scale bias reduction by a factor of 2.9 (not shown).

The positive wind speed bias associated with HOAPS is reflected in *Fig. 4.8*, showing the latitudinal distribution of all three wind speed products. The two-dimensional wind distribution following HOAPS is shown in *Fig. 4.9* (top), serving as a reference to locate individual features in space. Irrespective of the data source, *Fig. 4.8* indicates that mean maxima exceeding $8 - 10\ m/s$ are located in

the cyclone-active mid-latitudes and subpolar regions of both hemispheres, being more pronounced in the winter hemisphere (compare *Andersson et al.* (2011), *Fig. 1* (right) therein). On an annual basis, these maxima are best resolved within the southern latitudes ('roaring 40's', 'furious 50's') . Amongst others, *Fig. 4.9* (top) illustrates these maxima to be present off the Norwegian coast, towards Iceland as well as close to the northeastern coast of Greenland. Furthermore, dark green shadings indicate highest southern hemispheric mean wind speeds isolated within a broad belt south of $40°$S and towards the Antarctic continent. Characteristic wind speed minima ranging between $5-7\ m/s$, associated with the subtropical calms, are subject to least interannual variability (*Andersson et al.* (2011)), as is also resolved in *Fig. 4.8*.

Averages of $\vec{u}$ close to $5\ m/s$, on the other hand, are not only confined to (sub-)tropical regions, but local minima are also observed within the polar oceans (see *Fig. 4.9* (top)).

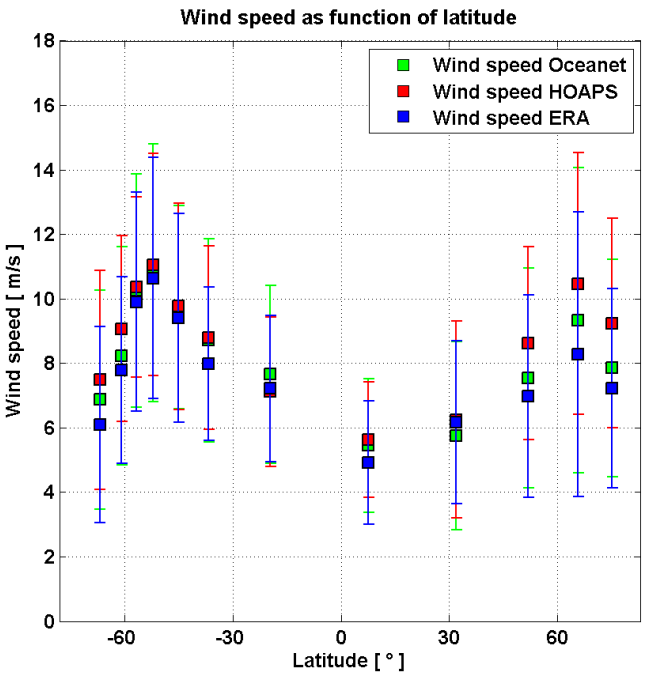

Fig. 4.8: As in *Fig. 4.3*, but showing wind speed products (10 m ASL) as a function of latitude.

As suggested by *Fig. 4.7*, HOAPS wind speeds tend to exceed the Oceanet- and ERA-based values on average, which is especially evident within the northern hemispheric mid-latitudes and further north as well as in southern subpolar regions, accompanied by considerable standard deviations of up to $4\ m/s$. 31% of all biases associated with HOAPS-based $\vec{u}$ are statistically significant when compared to Oceanet wind speeds, as indicated by the illustration of significant offsets in *Fig. 4.9* (bottom). These regions are subject to lowest correlation coefficients, which range between statistically significant 0.42-0.59 (compare *Table 14* for detailed latitude-dependent bias considerations). Numerous coastal areas, namely local regions off Antarctica, northeastern Greenland, Svalbard, and to a smaller extent off coastal Norway and the Antarctic Peninsula exhibit extraordinarily large biases exceeding $15\ m/s$ (to be discussed within *Section 5.2.2*), which are also resolved in bias considerations involving ERA winds (*Appendix, A. 4*, bottom). Biases north of $70°$N average to $2.5\ m/s$ (25% of regional mean) and are positive in 79% of all events.

A separate statistical analysis suggests a mean bias of $1.7-3.1\ m/s$ ($2.1-3.8\ m/s$) north of $40°$N when compared to Oceanet (ERA), representing a relative deviation of 23.6% -39.6% (30.8% -55.1%), respectively. On the basin scale, relative bias maxima are highest within the southern polar ocean (south of $60°$S), owing to small absolute $\vec{u}$. Yet, relative biases are relatively large, reaching percental deviations as large as 49.3% (Oceanet) and 72.5% (ERA) off Antarctica, respectively (compare *Table 14* and *Table 15*). Standard deviations of HOAPS wind speeds within this latitudinal band exceed $7\ m/s$ (i.e. 62% of the respective mean $\vec{u}$).

To the contrary, *Table 14* and *Fig. 4.9* clarify that wind speed biases are limited in the lower wind speed regimes within $40°$ of the equator. Disregarding the northern tropics between $0°$-$20°$N[37], merely small absolute and percental deviations are apparent, the mean of which is not statistically significant ($0.05\ m/s$ to Oceanet (1.3%), $0.13\ m/s$ to ERA (1.8%)). Negligible biases are prevailing in the southern mid-latitudes as well (considering transit data only, not shown), which are subject to high Oceanet- and ERA- based wind speeds. Deviations within the latter also remain small when considering the total dataset (3.4% (Oceanet), 6.9% (ERA)), as the intersection of the best-fit line with the perfect correlation reference (*Fig. 4.7*) implies for these wind speed ranges.

The basin average suggests a positive bias of $1.75\ m/s$ (21.9%) and $2.30\ m/s$ (30.7%) compared to Oceanet- and ERA data and corresponding statistically significant correlation coefficients are 0.58 (Oceanet) and 0.52 (ERA).

A restriction to transit-only cruises excludes error-prone (sub-)polar regimes, considerably improving the overall agreement between the wind speed products. This is not only indicated by elevated correlation coefficients (Oceanet: 0.78; ERA: 0.75), but is also manifested in a reduced, albeit statistically significant Atlantic bias of $0.46\ m/s$ ($0.79\ m/s$), i.e. 6.0% (11.0%) (Oceanet and ERA, respectively).

Table 14 and *Table 15* comprise a comprehensive statistical confrontation of HOAPS-based $\vec{u}$ to Oceanet- and ERA output.

To evaluate the strength of the linear relationship between LHF and prevailing wind speeds, *Fig. 4.10* shows regressions between $\vec{u}$ and respective LHF for all three data products.

All correlation coefficients are statistically significant at the 99% level. Analogous coefficients imply that the explained variance of the LHF fit to $\vec{u}$ ranges between 53% (Oceanet), 86% (ERA), and 90% (HOAPS). HOAPS LHF exhibits the strongest wind speed increase with concurrent strengthening of mean winds (roughly $6.7\ W/m^2$ increase per m/s). This implies that low wind speed regimes between 2-8 m/s favour a HOAPS-based mean flux underestimation of $-18.2\ W/m^2$ ($-16.6\ W/m^2$) compared to Oceanet (ERA) (as is also indicated for (sub-)tropical regions within *Table 11* and *Table 12*), which steadily decreases and eventually results in a respective slight overestimation for strong wind speeds exceeding $14\ m/s$.

As the best-fit lines indicate, Oceanet- and ERA-based LHF exhibit a strong similarity concerning their wind speed dependency. Strong Oceanet-based LHF outliers, however, are evident and reach an overall maximum of $76.9\ W/m^2$ at wind speeds ranging between $7 - 8\ m/s$.

Corresponding HOAPS- (ERA-) based mean LHF are lower by a factor of 2.29 (1.65), respectively. A restriction to transit cruises only yields lower relative deviations (not shown), albeit mean absolute deviations of approximately $-35\ W/m^2$ remain when comparing HOAPS- to Oceanet-based

[37] Here, Oceanet systematically yields wind speeds that are on average 11% larger than the ERA counterpart, resulting in a statistically significant positive bias of $0.60\ m/s$.

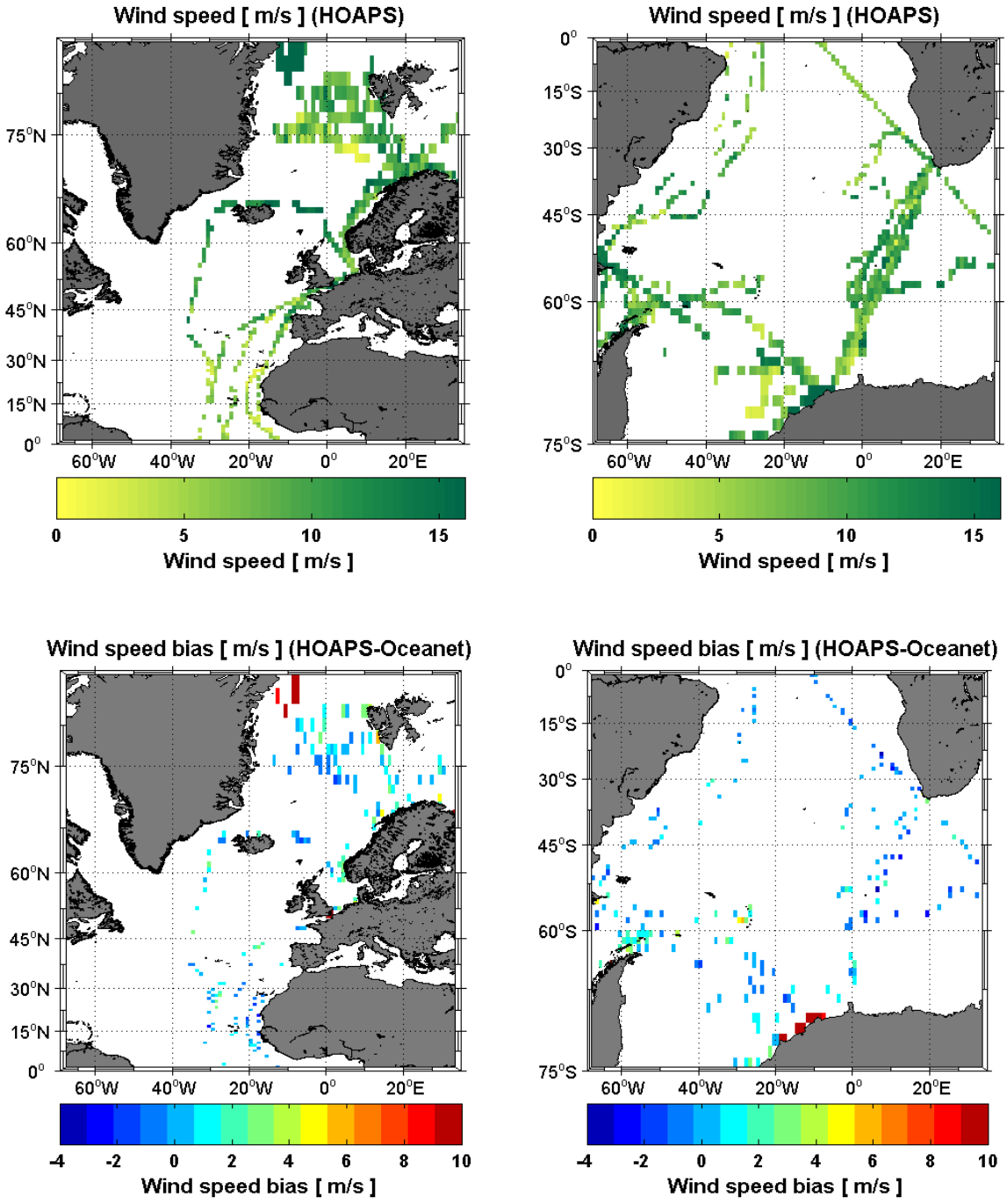

Fig. 4.9: Top left/right: Map ($1° \times 1°$ resolution) of mean HOAPS wind speed (10 m ASL) based on HOAPS 'events' (*Section 3.3*).
Bottom left/right: Map ($1° \times 1°$ resolution) of significant (at the 95% level) biases between Oceanet- and HOAPS wind speed (10 m ASL) based on HOAPS 'events' (*Section 3.3*). Positive values indicate a wind speed overestimation of HOAPS.

$region$	$events$	N_{eff}	$\overline{\vec{u}}_O$	std_O	$\overline{\vec{u}}_H$	std_H	$corr$	$bias$	$dev.[\%]$	$RMSE$
78°S - 82°N	4879	756	8.01	3.93	9.76	5.38	0.58*	1.75*	21.86	4.79
60°S - 78°S	1202	125	7.65	4.25	11.43	7.41	0.59*	3.78*	49.36	7.07
40°S - 60°S	1175	196	10.10	3.63	10.45	3.45	0.78*	0.35*	3.43	2.36
20°S - 40°S	431	109	8.50	3.20	8.37	2.84	0.83*	-0.13	-1.51	1.82
0°S - 20°S	199	62	6.48	1.98	6.24	1.92	0.77*	-0.24	-3.68	1.34
0°N - 20°N	238	56	5.49	2.03	5.73	1.69	0.73*	0.24	4.21	1.42
20°N - 40°N	265	68	5.40	2.41	5.74	2.41	0.74*	0.33	6.27	1.77
40°N - 60°N	457	80	7.16	3.49	8.85	3.90	0.66*	1.70*	23.59	3.49
60°N - 82°N	905	97	7.75	4.09	10.82	5.84	0.42*	3.06*	39.51	6.34

Table 14: As in *Table 11*, but comparing statistical parameters associated with Oceanet- and HOAPS-based $\vec{u}$ (10 m ASL).

$region$	$events$	N_{eff}	$\overline{\vec{u}}_E$	std_E	$\overline{\vec{u}}_H$	std_H	$corr$	$bias$	$dev.[\%]$	$RMSE$
78°S - 82°N	4861	804	7.47	3.57	9.77	5.41	0.52*	2.30*	30.71	5.21
60°S - 78°S	1110	117	6.73	3.61	11.61	7.67	0.54*	4.88*	72.53	8.11
40°S - 60°S	1246	212	9.72	3.50	10.39	3.51	0.76*	0.67*	6.87	2.52
20°S - 40°S	434	117	7.90	2.43	8.42	2.85	0.77*	0.53*	6.64	1.90
0°S - 20°S	199	54	6.01	1.78	6.24	1.92	0.66*	0.22	3.76	1.54
0°N - 20°N	238	57	4.89	1.90	5.73	1.69	0.52*	0.84*	17.04	1.96
20°N - 40°N	265	68	5.74	2.05	5.74	2.41	0.79*	0.00	0.05	1.50
40°N - 60°N	461	92	6.73	3.17	8.80	3.89	0.61*	2.08*	30.77	3.80
60°N - 82°N	901	98	6.98	3.70	10.82	5.86	0.40*	3.84*	55.10	6.73

Table 15: As in *Table 12*, but comparing ERA- to HOAPS-based $\vec{u}$ (10 m ASL).

Reg.	Lat	Lon	$Events$	$\overline{LHF_H}$	$Bias$	$Dev.[\%]$	$Events$	$\overline{\vec{u}_H}$	$Bias$	$Dev.[\%]$
1	$45-60°N$	$5°W$ - $10°E$	305	42.27	-30.68*	-42.02	358	8.74	1.86*	26.99
2	$63-68°N$	$8-30°W$	32	119.3	18.60	16.27	32	13.27	0.84	7.02
3	$72-82°N$	$25°W$ - $35°E$	271	39.38	-4.6	-11.26	477	11.13	4.31*	62.97
4	$0-25°S$	$10°W$ - $35°E$	122	71.89	-39.03*	-34.79	122	6.32	-1.08*	-14.22
5	$45-60°S$	$69°W$ - $35°E$	902	47.24	10.01*	26.88	983	10.69	0.39	3.83
6	$60-78°S$	$69°W$ - $0°E$	665	12.37	-3.27	-20.90	1147	11.62	3.95*	51.58

Table 16: Identical to *Table 13*, but extended by $\vec{u}$ biases (10 m ASL) between HOAPS and Oceanet within the six regions (Reg.), which are indicated in *Fig. 4.6*.

LHF. The latter suggests that the northern mid-latitudes up to $60°$N represent the potential source for this discrepancy, where according to *Table 11* and *Table 14*, relative LHF deviations of -27.5% and mean positive wind speed biases of 23.6% are evident with mean Oceanet-based winds of the order of $7.2\ m/s$. As highest mean wind speeds do not resolve Oceanet-based LHF of greater magnitude than observed between $7-8\ m/s$, one may argue that an LHF saturation occurs with increasing $\vec{u}$,

which does not account for both HOAPS- and ERA LHF (compare *Fig. 4.10*).

Referring to *Eq. 8*, one would presume anomalously negative LHF biases to be associated with respective negative wind speed deviations (and vice versa). A comparison of *Fig. 4.5* (bottom right) and *Fig. 4.9* (bottom right) partially confirms this, in as much as small negative LHF biases within *Region 4* go along with slight HOAPS-based wind speed underestimations. Similar findings hold for the region southwest of RSA, characterized by significant negative biases and concurrent mostly negative wind speed deviations.

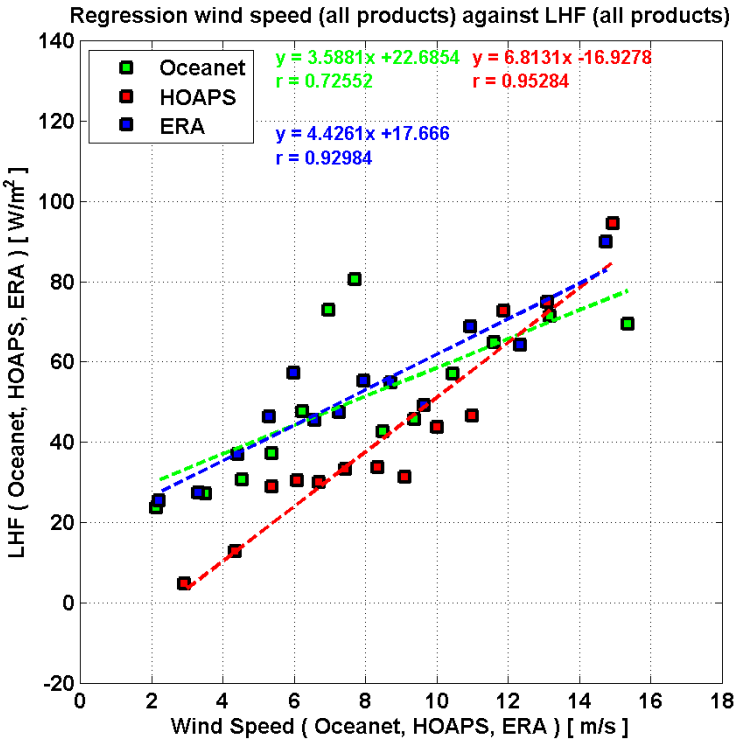

Fig. 4.10: All LHF products as a function of respective wind speed products (10 m ASL). Boxes are based on arithmetic means of 300 individual values, which itself correspond to 'HOAPS-events' (*Section 3.3*). Events based on negative LHF within the ERA- and Oceanet LHF have been neglected for consistency with the HOAPS dataset.

However, negative LHF biases between the North Sea and northern Norway as well as north of 70°N (*Regions 1* and *3*) are linked to positive wind speed anomalies (compare *Fig. 4.9*).

Region 6 represents the opposite case, in as much as negative LHF coexist with statistically significant positive wind biases. The latter implies that HOAPS-based over- (under-) estimations of $\vec{u}$ are outplayed by concurrent negative (positive) specific humidity biases, eventually producing LHF biases below (above) 0 W/m^2. *Table 16* shows a supplemented version of *Table 13*, presenting LHF- and simultaneous wind speed biases between HOAPS and Oceanet restricted to the six regional cases shown in *Fig. 4.6*. Albeit absolute wind speeds are overestimated within the HOAPS data records (on the whole), corresponding LHF tend to be below the flux algorithm- and reanalysis-based values (compare *Section 4.2*). The subsequent humidity bias analysis aims to quantify the impact of regional specific humidity deviations on resulting patterns of significant LHF offsets.

4.4 Quantification of q_a Biases Between HOAPS, Oceanet, and ERA

Fig. 4.11 shows the distribution of specific humidity q_a of all three data products as a function of latitude. The distribution is symmetric about the equator, i.e. mean q_a range between $2.9 - 4.1\ g/kg$ within the polar oceans and $16.0 - 17.2\ g/kg$ in tropical latitudes.

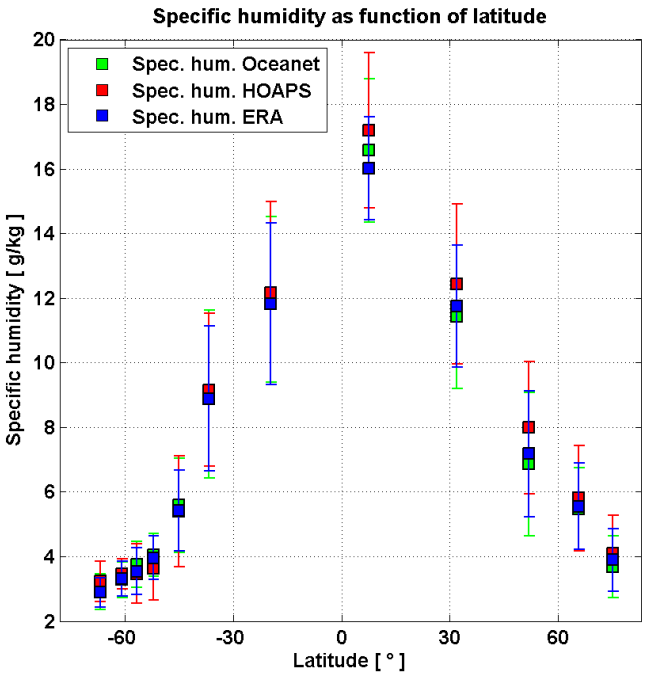

Fig. 4.11: As in *Fig. 4.3*, but illustrating specific humidities products (10 m ASL) as a function of latitude.

The mid-latitudes are subject to strong increases towards $0°$ latitude (compare transition from green to blue shading between $30°$-$50°$N/S in *Fig. 4.13* (top), exemplarily illustrating mean HOAPS q_a), associated with a simultaneous spatial surface temperature gradient, as indicated by *Eq. 1*. Apart from southern hemispheric mid-latitudes, HOAPS overestimates q_a, as is also indicated by the basin-scale mean q_a of $6.19\ g/kg$ (Oceanet, 8.8%), $6.20\ g/kg$ (ERA, 9.0%), and $6.76\ g/kg$ (HOAPS) (compare *Table 18 / Table 19*).

A comparison to Oceanet- (ERA-) based q_a indicates largest, statistically significant deviations of $0.76\ g/kg$ ($0.77\ g/kg$) ($60°$-$78°$S), $1.26\ g/kg$ ($0.97\ g/kg$) ($40°$-$60°$N), and $0.85\ g/kg$ ($0.72\ g/kg$) ($60°$-$82°$N), each of which are associated with relative deviations of 25.4% (26.4%), 17.2% (12.6%), and 19.9% (16.4%).

As indicated above, minor, albeit statistically significant negative biases compared to Oceanet are restricted to $40°$-$60°$S, amounting to $-0.14\ g/kg$ (-3.1%). This is different when considering ERA, the bias to which is exclusively positive within the pre-defined latitudinal ranges. Comparing HOAPS- to Oceanet- (ERA-based) q_a, (sub-)tropical biases ($0°$-$40°$ N/S) average to $0.53\ g/kg$ ($0.70\ g/kg$), equating 4.1% (5.1%), of which only the northern hemispheric part is statistically significant at a mean relative deviation of 6.3% (6.7%).

The statistically significant basin-scale mean bias associated with Oceanet (ERA) amounts to $0.54\ g/kg$ ($0.56\ g/kg$), corresponding to 8.8% (9.0%) of relative anomaly. The basin scale correlation of 0.95 (ERA: 0.96) is statistically significant at the 99% level.

Fig. 4.12 illustrates the q_a - regression of HOAPS and Oceanet (left) / ERA (right). Both correlation coefficients are statistically significant at the 99% level. As discussed above and indicated in *Table 18* and *Table 19*, *Fig. 4.12* mirrors the overestimation of HOAPS q_a within the slope of the best-fit line. The offset grows linearly with increasing q_a, causing mean biases to exceed $1\ g/kg$ given a background specific humidity of $15\ g/kg$ or more.

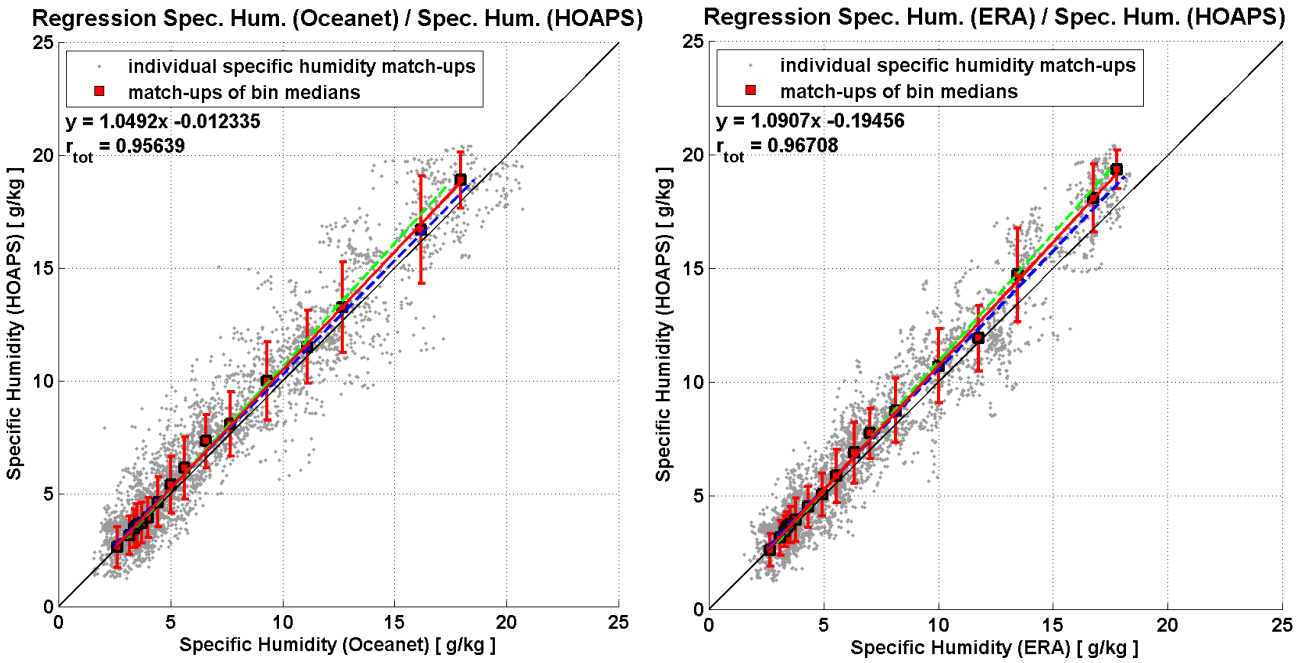

Fig. 4.12: As in *Fig. 4.4*, but showing two-sided orthogonal regression of (**left**) Oceanet- and HOAPS-based q_a (10 m ASL) and (**right**) ERA- and HOAPS-based q_a (10 m ASL).

Fig. 4.13 (bottom) shows the geographical distribution of statistically significant q_a biases to the Oceanet reference, which amount to 36% of all grid box biases (refer to *Appendix, A. 5* for the comparison of ERA and HOAPS).

As indicated in *Fig. 4.13* (bottom), numerous positive biases are evident north of $50°$N (77% positive, maxima exceed $3.5\ g/kg$ between France and Norway as well as off Greenland), more precisely northwest of the Norwegian coast as far as between Svalbard and Greenland.

Cumulative overestimations of specific humidity are also located off the Antarctic continent and - peninsula, where 88% of significant biases are positive south of $60°$S. In contrast, as suggested by *Fig. 4.11*, 70% of observed biases within the southern mid-latitudes ($45°$-$60°$S) are negative ($-0.12\ g/kg$). Amongst others, locally strong negative biases are observed east/west of Iceland as well as off Uruguay.

Compared to Oceanet (ERA), a restriction to transit cruises only (not shown) yields an overall bias of $0.50\ g/kg$ ($0.59\ g/kg$) (i.e. 4.6% (5.6%)), based on the HOAPS Atlantic mean of $11.28\ g/kg$.

As expressed by *Eq. 8*, HOAPS likely underestimates LHF given a concurrent specific humidity overrepresentation[38] (and vice versa). *Table 17* depicts the expansion of the case studies within *Regions 1 - 6* to specific humidity considerations (bottom left) and invariably confirms this relationship between LHF and q_a, as is reflected in opposite bias signs, respectively. Based on these insights, the strongly negative significant LHF biases within *Region 1* are likely to be caused by an overrepresentation of q_a, the latter of which can also be concluded for *Region 3* and *6*. Significant LHF

[38] As LHF is proportional to $(q_s - q_a)$, where $q_a \leq q_s$, the air-sea humidity difference tends to be smaller and concurrently also LHF when considering HOAPS.

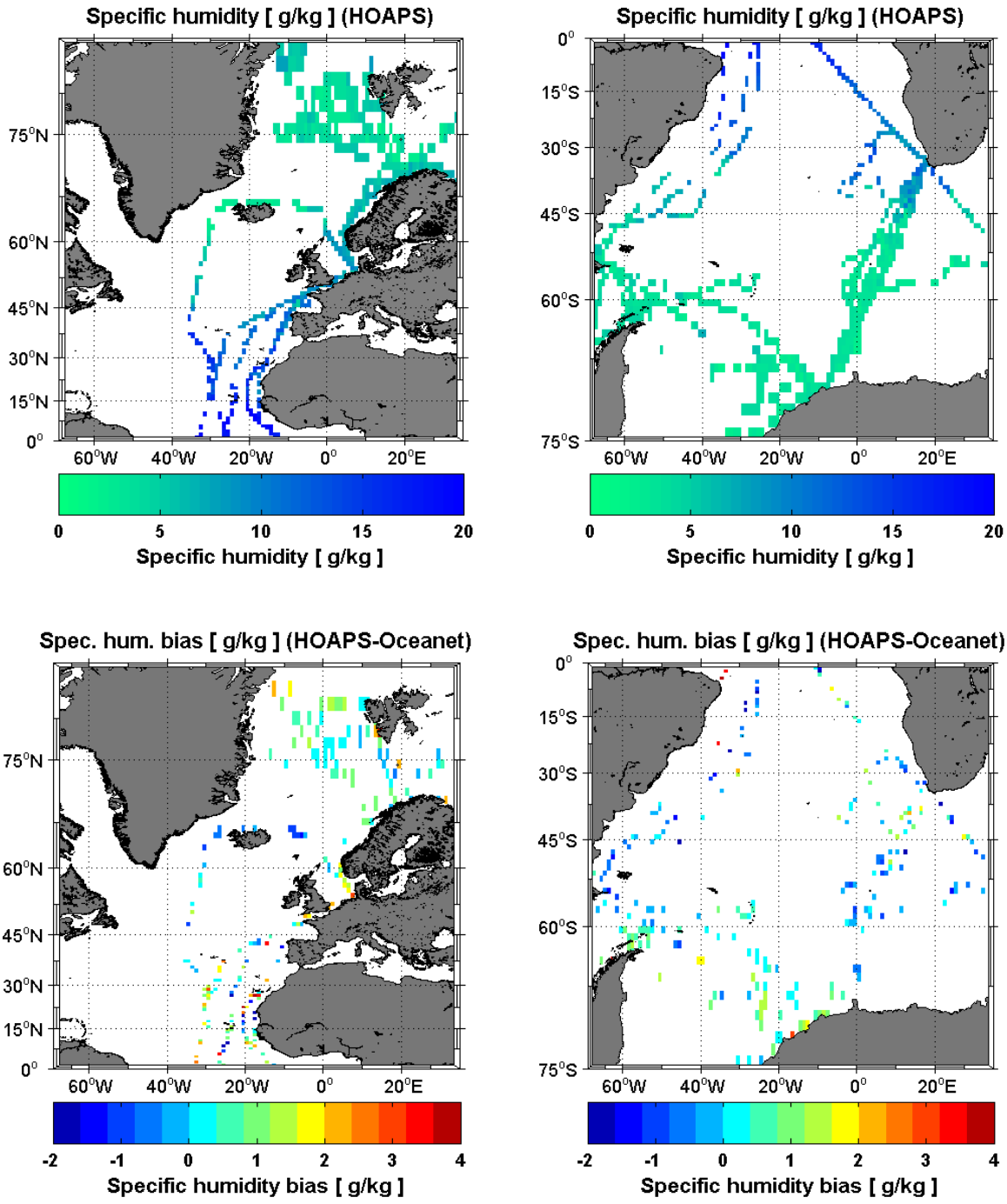

Fig. 4.13: Top left/right: Map ($1° \times 1°$ resolution) of mean HOAPS specific humidity q_a (10 m ASL) based on HOAPS 'events' (*Section 3.3*).
Bottom left/right: Map ($1° \times 1°$ resolution) of significant (at the 95% level) biases between Oceanet- and HOAPS q_a (10 m ASL) based on HOAPS 'events' (*Section 3.3*). Positive values indicate a q_a overestimation of HOAPS.

underestimations within *Region 4* may be attributed to both an underrepresentation of $\vec{u}$ as well as a coexisting positive offset in q_a.

Reg.	Lat	Lon	$Events$	$\overline{LHF_H}$	$Bias$	$Dev.[\%]$	$Events$	$\overline{\vec{u}_H}$	$Bias$	$Dev.[\%]$
1	$45-60°N$	$5°W$ - $10°E$	305	42.27	-30.68*	-42.02	358	8.74	1.86*	26.99
2	$63-68°N$	$8-30°W$	32	119.3	18.60	16.27	32	13.27	0.84	7.02
3	$72-82°N$	$25°W$ - $35°E$	271	39.38	-4.6	-11.26	477	11.13	4.31*	62.97
4	$0-25°S$	$10°W$ - $35°E$	122	71.89	-39.03*	-34.79	122	6.32	-1.08*	-14.22
5	$45-60°S$	$69°W$ - $35°E$	902	47.24	10.01*	26.88	983	10.69	0.39	3.83
6	$60-78°S$	$69°W$ - $0°E$	665	12.37	-3.27	-20.90	1147	11.62	3.95*	51.58
Reg.	Lat	Lon	$Events$	$\overline{q_{aH}}$	$Bias$	$Dev.[\%]$	$Events$	$\overline{(q_a-q_s)_H}$	$Bias$	$Dev.[\%]$
1	$45-60°N$	$5°W$ - $10°E$	358	8.23	1.38*	20.00	305	1.24	-1.48*	-54.31
2	$63-68°N$	$8-30°W$	32	2.82	-0.92	-24.36	32	2.44	0.57	27.62
3	$72-82°N$	$25°W$ - $35°E$	477	4.41	1.15*	35.16	271	0.80	-0.61*	-43.35
4	$0-25°S$	$10°W$ - $35°E$	122	12.72	0.62*	5.21	122	3.16	-0.94*	-22.55
5	$45-60°S$	$69°W$ - $35°E$	983	3.90	-0.23*	-5.58	903	1.07	0.14*	15.21
6	$60-78°S$	$69°W$ - $0°E$	1147	3.77	0.79*	26.66	667	0.14	-0.60*	-80.97

Table 17: Identical to *Table 16*, but extended by q_a- (10 m ASL) and $q_s - q_a$ biases between HOAPS and Oceanet within the six regions (Reg.), which are indicated in *Fig. 4.6*.

$region$	$events$	N_{eff}	$\overline{q_{a,O}}$	std_O	$\overline{q_{a,H}}$	std_H	$corr$	$bias$	$dev.[\%]$	$RMSE$
$78°S$ - $82°N$	4879	756	6.19	4.20	6.74	4.30	0.95*	0.54*	8.76	1.47
$60°S$ - $78°S$	1202	125	2.98	0.57	3.74	0.87	0.15	0.76*	25.42	1.23
$40°S$ - $60°S$	1175	196	4.51	1.41	4.37	1.70	0.86*	-0.14*	-3.09	0.89
$20°S$ - $40°S$	431	109	9.61	2.44	9.74	2.45	0.77*	0.13	1.35	1.65
$0°S$ - $20°S$	199	62	14.46	2.58	14.81	2.85	0.71*	0.34	2.46	2.11
$0°N$ - $20°N$	238	56	16.60	2.33	17.20	2.46	0.75*	0.59*	3.58	1.80
$20°N$ - $40°N$	265	67	11.79	1.98	12.84	2.33	0.63*	1.06*	8.93	2.15
$40°N$ - $60°N$	457	80	7.26	2.35	8.52	2.17	0.82*	1.26*	17.24	1.86
$60°N$ - $82°N$	905	97	4.25	1.51	5.09	1.69	0.69*	0.85*	19.92	1.52

Table 18: As in *Table 11*, but comparing statistical parameters associated with Oceanet- and HOAPS-based q_a (10 m ASL).

Fig. 4.14 displays all LHF data products as a function of their specific humidities. Overall, the linear relationships are positive, suggesting highest mean LHF to occur for elevated specific humidities, as is the case in (sub-)tropics. Furthermore, the considerably smaller slope of the regression line associated with HOAPS implies a weaker dependency of HOAPS LHF on q_a (r is solely significant at the 95% level and the explained variance remains low with 23.6%, in contrast to both Oceanet and ERA, the best-fit lines of which resolve explained variances of 68% and 84%, respectively.

Fig. 4.14 clearly illustrates the overall LHF underrepresentation on the part of HOAPS, abandoning the considerable mean overestimation for smallest specific humidities. The latter comprise 300 individual measurements, which were mostly obtained within the polar oceans (71% (22%) south

region	*events*	N_{eff}	$\overline{q_{a,E}}$	std_E	$\overline{q_{a,H}}$	std_H	*corr*	*bias*	*dev.*[%]	*RMSE*
78° S - 82° N	4861	804	6.20	4.06	6.76	4.31	0.96*	0.57*	9.16	1.35
60° S - 78° S	1110	117	2.94	0.52	3.70	0.87	0.18	0.77*	26.17	1.21
40° S - 60° S	1246	212	4.37	1.35	4.41	1.70	0.84*	0.03	0.73	0.93
20° S - 40° S	434	117	9.44	2.13	9.72	2.43	0.83*	0.28*	2.99	1.39
0° S - 20° S	199	54	14.24	2.40	14.81	2.85	0.82*	0.68*	4.90	1.78
0° N - 20° N	238	57	16.61	1.66	17.20	2.46	0.81*	1.21*	7.53	1.91
20° N - 40° N	265	68	12.32	1.70	12.84	2.33	0.69*	0.81*	6.60	1.87
40° N - 60° N	461	92	7.57	2.12	8.54	2.17	0.85*	0.98*	12.80	1.54
60° N - 82° N	901	98	4.38	1.50	5.10	1.71	0.71*	0.72*	16.44	1.44

Table 19: As in *Table 12*, but comparing ERA- to HOAPS-based q_a (10 m ASL).

(north) of 60°S (60°N)).

A separate analysis reveals that large HOAPS-based LHF (along with smallest q_a) are located close to northern Norway, surrounding Iceland as well as between Punta Arenas and the Antarctic Peninsula (compare red shadings in *Fig. 4.5* (bottom)). According to HOAPS, the mean wind speed exceeded 11.6 m/s (5.9% and 13.5% larger than concurrent mean Oceanet- and ERA wind speeds), which may to some extend explain the strong positive LHF bias.

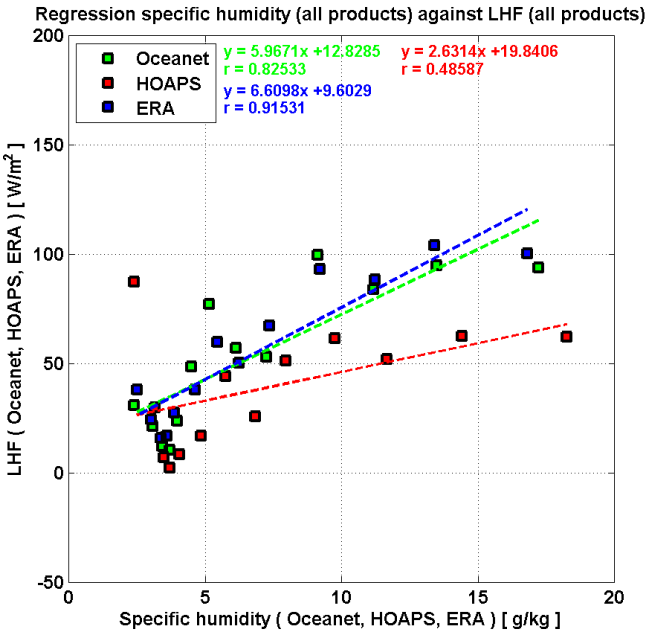

Fig. 4.14: As in *Fig. 4.10*, but illustrating all LHF products as a function of their respective q_a products (10 m ASL).

Whereas the best-fit lines closely describe the linear relationship for q_a below 7 g/kg, mean LHF do not tend to increase with higher specific humidities, as indicated by the coloured squares in *Fig. 4.14*.

This saturation behaviour accounts for the fact that highest LHF are not observed within the tropics, where q_a maximises (compare *Fig. 4.13* (top)), but rather within mid-latitudes, which are subject to strong gradients of q_a.

A consideration of the difference between surface saturation specific humidity (q_s) and q_a, confirms the significant underestimation of humidity parameters within HOAPS. Similar to q_a itself, $q_s - q_a$ tends to be largest in lower latitudes (along with elevated SST), where both individual physical parameters maximise. According to Oceanet (HOAPS), their latitudinal means range between 0.74 g/kg (0.16 g/kg) [60°-78°S] and 5.24 g/kg (4.20 g/kg) [0°-20° N/S]. Local absolute maxima of $q_s - q_a$ within the subtropics exceed 10 g/kg.

Comparing HOAPS- to Oceanet-based $q_s - q_a$, a mean significant correlation coefficient of 0.77 and a mean basin-scale bias of $-0.56\ g/kg$ is observed (HOAPS mean: $1.78\ g/kg$, corresponding to a relative deviation of -24.3%). As for q_s considerations only, mean biases remain negative throughout the basin, with the exception of the southern mid-latitudes (non-significant bias of $0.03\ g/kg$). Considerable offsets of $-0.57\ g/kg$ (-78%), $-1.40\ g/kg$ (-48.1%), and $-0.66\ g/kg$ (-41.0%) are resolved within 60°-78°S, 40°-60°N, and 60°-82°N, respectively.

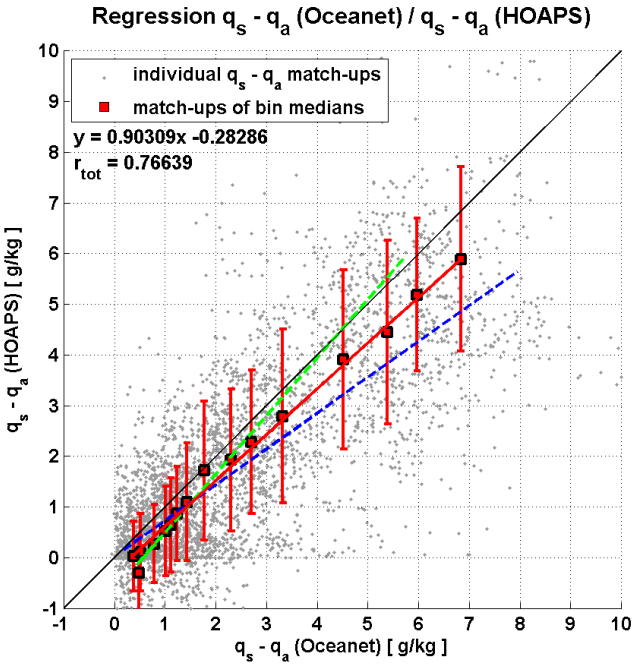

Fig. 4.15: As in *Fig. 4.4*, but showing two-sided orthogonal regression of Oceanet- and HOAPS-based $q_s - q_a$. .

Significant biases are again located within the northern polar ocean, close to Iceland, along the Norwegian coast as far as Great Britain, and within the southern hemispheric extratropics (largely negative south of 60°S) (not shown). Strong absolute underestimations of $q_s - q_a$ are especially resolved within 0°-30°N (81% of significant biases are negative) with a mean bias of $-1.25\ g/kg$ (not shown).

region	*events*	N_{eff}	$\overline{(q_s - q_a)_O}$	std_O	$\overline{(q_s - q_a)_H}$	std_H	*corr*	*bias*	*dev.*[%]	*RMSE*
78°*S* - 82°*N*	4022	682	2.35	2.12	1.78	2.02	0.77*	-0.56*	-24.02	1.51
60°*S* - 78°*S*	722	78	0.74	0.56	0.16	0.66	0.39*	-0.57*	-78.03	0.89
40°*S* - 60°*S*	1095	189	1.25	1.25	1.28	1.37	0.73*	0.03	2.49	0.97
20°*S* - 40°*S*	427	109	4.08	2.19	3.85	1.92	0.66*	-0.23	-5.57	1.73
0°*S* - 20°*S*	199	62	5.45	1.69	4.59	2.25	0.46*	-0.88*	-15.83	2.27
0°*N* - 20°*N*	237	55	5.02	1.86	3.81	1.59	0.39*	-1.22*	-24.26	2.28
20°*N* - 40°*N*	261	66	4.77	1.81	3.58	1.84	0.45*	-1.18*	-24.86	2.25
40°*N* - 60°*N*	404	70	2.91	1.71	1.51	1.64	0.65*	-1.40*	-48.15	1.98
60°*N* - 82°*N*	670	73	1.61	0.89	0.95	1.26	0.55*	-0.66*	-40.98	1.26

Table 20: As in *Table 11*, but comparing statistical parameters associated with Oceanet- and HOAPS-based $q_s - q_a$.

These statistically significant offsets are also documented within *Fig. 4.15*, which illustrates the two-sided orthogonal regression of $q_s - q_a$ between Oceanet- and HOAPS-based data. The slope of the best-fit line is considerably smaller than one, indicating a large underestimation of the HOAPS humidity difference (mean: $-0.52\ g/kg$), especially towards the tropics (the mean bias for $q_s - q_a$ exceeding $3\ g/kg$ becomes $0.75\ g/kg$ (-14.4%)).

Considering transit cruises only, the mean basin-scale bias amounts to -0.74 (-19.0%), where the

Atlantic HOAPS mean is given by $3.16\ g/kg$. Southern mid-latitudes exhibit an increasingly positive bias of $0.24\ g/kg$ (yet not statistically significant), corresponding to 15.3%. Northern latitudes remain statistically significantly underestimated with a mean bias of $-1.22\ g/kg$ (-24.3%), $-1.18\ g/kg$ (-24.8%), and $-1.14\ g/kg$ (-40.5%) within 0°-20°N, 20°-40°N, and 40°-60°N, respectively.

Drawing the attention back to the the case studies, $q_s - q_a$ amended to *Table 17* (bottom right) resolves a contrarious behaviour compared to q_a, in as much as positive biases of q_a go along with negative $q_s - q_a$ biases (and vice versa), since $q_a \leq q_s$. The latter serves to explain observed negative LHF offsets within *Regions 1*, *3*, *4*, and *6*, whereas the reversed relationship gives rise to positive LHF biases within southern mid-latitudes (*Region 5*).

For conclusion of specific humidity considerations, *Table 20* shows a statistical comparison involving Oceanet- and HOAPS-based $q_s - q_a$[39].

4.5 Quantification of SST Biases Between HOAPS, Oceanet, and ERA

Regression analysis of HOAPS- and Oceanet-based SST (not shown) yields a statistically significant correlation coefficient exceeding 0.999, where the negative offset of the best-fit line is given by -0.11 °C (not shown) indicating that HOAPS tends to slightly underestimate SST. The basin-scale HOAPS-mean is given by 10.27 °C, the respective bias equals to -0.05 °C (compare *Table 21*), which is statistically not significant. Mean SST-maxima are confined to the tropics (25.58 °C, $0° - 20$ °N/S) and minima restricted to the southern polar ocean (-0.06 °C, south of 60 °S). Apart from subtropical latitudes on both hemispheres, where biases are significantly positive[40] (0.16 °C / 0.21 °C ($20 - 40$°N/S, respectively)), biases are negative and amount to maxima of -0.18 °C within the southern polar ocean, where 81% of all significant deviations are below 0 °C. In contrast, biases north of $72°N$ are characterized by strong regional gradients, ranging between -1 °C and $+1$ °C. The analogous mean bias of -0.05 °C is statistically not significant.

To the contrary, a comparison of ERA- and HOAPS-based SST (see *Table 22*) exhibits a statistically significant basin-scale bias of -0.19 °C (-1.8%), which is partly reflected in the best-fit offset of -0.34 °C. Overall, deviations are larger compared to those associated with Oceanet reaching -0.5 °C (-1.85%, $0° - 20$°N) to as much as -0.57 °C (south of 60°S).

Explicit conclusions as to the link between SST- and LHF biases within *Regions 1-6* cannot be drawn. Significant SST biases compared to Oceanet are restricted to *Regions 5-6* (-0.09 °C / -0.19 °C), which are associated with a considerable positive LHF bias ($10\ W/m^2$, 26.9%) / negligible negative LHF bias ($-3.3\ W/m^2$, -20.9%).

[39] A comparison of HOAPS- to ERA-output is not accounted for, as the ERA reanalysis product does not include q_s data.

[40] Locally, biases exceed 1 °C southwest of RSA. Between $36° - 45$°S, 73% of biases are positive, the mean of which is given by 0.09 °C.

$region$	$events$	N_{eff}	$\overline{SST_O}$	std_O	$\overline{SST_H}$	std_H	$corr$	$bias$	$dev.[\%]$	$RMSE$
78°S - 82°N	4041	684	10.31	9.04	10.27	9.09	0.997*	-0.05	-0.41	0.70
60°S - 78°S	733	79	0.12	0.73	-0.06	0.75	0.823*	-0.18*	-147.17	0.48
40°S - 60°S	1099	189	5.38	4.64	5.32	4.65	0.986*	-0.07	-1.14	0.79
20°S - 40°S	427	109	18.92	2.31	19.14	2.12	0.945*	0.21*	1.15	0.79
0°S - 20°S	199	62	24.91	2.84	24.88	2.72	0.991*	-0.06	-0.15	0.40
0°N - 20°N	237	55	26.42	2.24	26.27	2.16	0.965*	-0.15	-0.56	0.61
20°N - 40°N	261	66	21.99	2.30	22.14	2.50	0.979*	0.16*	0.66	0.55
40°N - 60°N	406	70	14.39	2.85	14.30	2.79	0.986*	-0.08	-0.63	0.47
60°N - 82°N	672	74	6.96	3.35	6.91	3.18	0.960*	-0.04	-0.66	0.94

Table 21: As in *Table 11*, but comparing statistical parameters associated with Oceanet- and HOAPS-based SST.

$region$	$events$	N_{eff}	$\overline{SST_E}$	std_E	$\overline{SST_H}$	std_H	$corr$	$bias$	$dev.[\%]$	$RMSE$
78°S - 82°N	4044	722	10.55	8.92	10.35	9.03	0.996*	-0.19*	-1.82	0.82
60°S - 78°S	672	74	0.52	0.65	-0.05	0.75	0.779*	-0.57*	-108.99	0.74
40°S - 60°S	1172	203	5.56	4.41	5.31	4.63	0.991*	-0.25*	-4.48	0.70
20°S - 40°S	427	114	19.09	2.07	19.13	2.13	0.924*	0.03	0.21	0.82
0°S - 20°S	199	54	24.82	3.03	24.88	2.72	0.824*	0.03	0.22	1.72
0°N - 20°N	237	57	26.77	2.16	26.27	2.16	0.976*	-0.50*	-1.85	0.69
20°N - 40°N	261	66	22.26	2.35	22.14	2.50	0.984*	-0.11	-0.53	0.47
40°N - 60°N	410	82	14.33	2.84	14.30	2.79	0.976*	-0.02	-0.21	0.62
60°N - 82°N	659	74	6.90	3.23	6.94	3.18	0.960*	0.05	0.58	0.91

Table 22: As in *Table 12*, but comparing ERA- to HOAPS-based SST.

4.6 Concluding Remarks on Bias Analysis

In terms of latitudinal means, HOAPS-based LHF resolve significant biases between $60°$S-$60°$N ($40°$S-$60°$N) compared to the Oceanet- (ERA-) counterpart. Bias analyses within *Section 4.2 - 4.5* indicate differences in terms of their triggering associated with $\vec{u}$, q_a, $q_s - q_a$, and SST.

In summary, the significant negative biases ranging from $20°$S-$60°$N, encompassing *Regions 1* and *4*, may be traced back to q_a overestimation of HOAPS, which (in comparison to Oceanet) goes along with a concurrent underestimation of $q_s - q_a$. The q_a impact can be considered as especially influential between $40°$-$60°$N (additionally $0°$-$20°$N compared to ERA), where it masks concurrent significant positive biases in $\vec{u}$. Negative LHF biases within $20°$-$40°$S can be attributed to a HOAPS-based SST underestimation, which in the case of the Oceanet reference outperforms the persisting wind speed bias of opposite sign.

Southern Ocean extratropics (*Region 5*) represent an exception (in comparison to Oceanet only), as the main driver for the observed positive LHF bias is a concurrent positive deviation in $\vec{u}$, masking the anomalously low background q_a.

Despite considerable (sub-)polar significant LHF biases, as illustrated in *Fig. 4.5* (bottom), they remain non-significant on latitudinal ranges, which includes *Regions 2*, *3*, and *6*. One the one hand, this is associated with inconsistent bias signs along latitudinal sections (e.g. along $65°$N). On the other hand, it results from a sparse data density, especially in context of *Region 2*. This highlights the importance of the applied significance analysis and recalls that locally large systematic deviations are fraught with uncertainty as to their reliability.

However, owing to a large data availability poleward of $60°$ N/S, the results underpin the strength of the HOAPS dataset and thus its underlying bulk flux algorithm (*Fairall et al.* (2003)) to deliver satisfying LHF estimates within the high-latitudinal ocean.

5 Error Analysis and Discussion

Differences of LHF estimates among the datasets, as observed in the former chapter, may be traced back to numerous reasons. Primarily, they result from either differences in the applied bulk flux parameterization schemes (*Kubota et al.* (2003), *Brunke and Zeng* (2002)) or are associated with diverging bulk flux parameters serving as algorithm input (*Kubota et al.* (2003), *Bourras* (2006)).

Both aspects and further considerations are discussed in the following subchapters.

5.1 Differing Parameterizations

Addressing bulk flux algorithm uncertainties, *Brunke and Zeng* (2002) suggest essential parameterizations, which may contribute to considerable differences among the calculated fluxes. On a global scale, these are considered to have a smaller impact on LHF deviations compared to the effect of varying bulk flux parameters underlying the datasets. The tropics, however, tend to be vulnerable, where deviations may exceed $15\ W/m^2$, solely due to the application of different bulk flux algorithms.

The algorithm uncertainties comprise the representation of the surface wave spectrum, the roughness length formulation, the choice of the von Kármán constant, the consideration of the convective gustiness, the effect of the q_a reduction due to salinity, and the turbulent exchange coefficient formulation. Additionally, the handling of light and strong winds as well as atmospheric (in-) stabilities are sources of errors.

Whereas the surface roughness on sea is lower than over land, it considerably varies, as it depends on the wave field, which itself is a function of the absolute wind speed, upstream fetch (i.e. the distance to the coast) as well as water depths. Its representation within bulk flux algorithms is expressed by the velocity roughness length z_0 (compare *Eq. 14*), which constitutes the sum of the surface roughness length for gravity waves (*Charnock* (1955)) and that of a smoothed surface (*Liu et al.* (1979)). The latter may be more complex in case one considers capillary waves (*Brunke and Zeng* (2002))[41], as is not the case among the parameterizations within this study. Although applied roughness length parameterizations were developed for open ocean conditions, the same algorithms are also applied in coastal waters. The latter implies that resulting LHF close to shorelines, e.g. within the English Channel and off Norway, Svalbard, and Greenland are subject to uncertainty, associated with substantial spatial roughness length gradients. *Bumke et al.* (1998) demonstrate this by means of changing ageostrophic ratios[42] as a function of distance to the coast. The authors conclude that the 'impacting' distance crucially depends on the wind direction, namely on- and offshore winds as well as those parallel to the coastline.

[41] *Brunke and Zeng* (2002) argue that bulk flux algorithms explicitly including a capillary wave dependency tend to consistently resolve higher wind speeds. Furthermore, the effect may cause positive LHF biases in case of stable atmospheric stratification.

[42] ratio of observed surface $\vec{u}$ (reduced to 10 m ASL, assuming a logarithmic wind profile) to analyzed geostrophic $\vec{u}$.

The impact of varying z_0 on resulting LHF crucially depends on the considered wind speed ranges. *Zeng et al.* (1998) argue that both weak wind conditions ($\leq 2\ m/s$), which favour stable stratification, as well as strong wind speeds, often associated with an atmospheric stratification close to neutral ($\zeta \approx 0$), are susceptible to the choice of z_0.

Numerous suggestions have been made for the Charnock parameter α (*Charnock* (1955)), which constitutes a part of the z_0 representation and can be linked to gross characterizations of the sea state, such as age and the slope of the dominant wave length. Values between 0.011 (*Smith* (1988), applied within Coare2.5) and 0.035 (e.g. *Garratt* (1992)) exist in literature. Whereas *Chou et al.* (2003) apply a constant of 0.014, *Taylor and Yelland* (2001) argue that α increases linearly from 0.011 to 0.017 for winds ranging between $6 - 26\ m/s$.

A wind speed dependent increase of α also serves as a basis for the HOAPS LHF calculation as well as the Oceanet algorithm applied within this work, both employing a linear increase of α from 0.011 to 0.018 between $10-18\ m/s$, based on data of *Hare et al.* (1999), amongst others (*Fairall et al.* (2003), compare *Fig.11* therein). Due to a lack of information, α is considered as being constant for even higher wind speeds. According to *Fairall et al.* (2003), one should keep in mind that the value of α remains controversial for wind speeds exceeding $10\ m/s$, introducing a source of uncertainty in the LHF outputs.

In contrast to Oceanet- and HOAPS LHF, α underlying ERA is based on *Eq. 14* and incorporates a constant Charnock Parameter of 0.018 (compare *ECMWF* (2006), p. 34), which implies that α is overrepresented in more than 99% compared to Oceanet and HOAPS and thus continuously simulates near-coastal conditions (see note on ageostrophic components above). The relative deviation of α in reference to the one applied by Oceanet and HOAPS is especially distinct in low-wind regimes. As a larger roughness length z_0 goes along with a larger transfer coefficient C_e, LHF resolves a systematic positive bias, which may partly explain the highest absolute LHF values resolved by ERA within the (sub-)tropics as indicated by *Fig. 4.3*, for example. The implication of *Brunke and Zeng* (2002), suggesting the ECMWF forecast model to systematically overestimate wind stress due to the underlying elevated z_0 is also mirrored in continuously lower ECMWF $\vec{u}$ within this study (compare e.g. *Fig. 4.8*).

Given varying representations of z_0 among different parameterizations, moisture- and heat roughness lengths, z_{0q} and z_{0T}, may also deviate, eventually impacting the LHF output. The latter two may either be identical to z_0 or depend on z_0, the latter being the case for the Oceanet- and Coare-algorithm, on which HOAPS is based. Both algorithms have in common that $z_{0q} = z_{0T}$ (as suggested by *Large and Pond* (1982)). In contrast, ERA is based on three different roughness lengths (*Beljaars* (1994)), where $z_{0q} \geq z_{0T}$ (see *ECMWF* (2006), p. 34). Following an investigation of transfer coefficient uncertainties among Coare2.5 and algorithms of *Zhang and McPhaden* (1995) and *Beljaars* (1995) under light wind conditions, *Chang and Grossman* (1999) argue that the impact on the bias of the transfer coefficients C_q and C_h is confined to 3-4% (despite large deviations of z_{0q} and z_{0T} among the algorithms), which may eventually produce a LHF bias error of 6-8%. This bias may not be as substantial within this work, as is suggested by the excellent agreement between Oceanet-based- and

in-situ ID LHF (Bumke, pers. comm., June 2013).

All roughness lengths eventually impact the derived values (10 m ASL) of stability-dependent temperature, specific humidity, and absolute wind speed, the source-dependent biases of which have been partly investigated within *Section 4*. Hence, observed deviations may be traced back to different roughness length parameterizations.

Slightly different representations of the turbulent exchange coefficients C_d, C_h, and C_e among the algorithms, which are functions of wind speed and the dynamic stability of the air (*Liu et al.* (1979), *Bourras* (2006)), may account for deviations within the LHF outputs. Within the framework of a satellite- and reanalysis intercomparison study of weekly and monthly LHF estimates between 1996-1997, *Bentamy et al.* (2003) proposes that C_e underlying the ECMWF forecast model, which is based on *Beljaars* (1994), exceeds that of HOAPS, which (in their case) may explain more than $10\ W/m^2$ of their observed positive LHF bias. *Zeng et al.* (1998) confirm that these applied C_e are too high.

Schulz et al. (1997) demonstrate the importance of stability scheme implementations in context of LHF estimates and show that the latter may vary considerably under little winds and stable conditions, where the assumption of a constant air-sea temperature difference (i.e. $T_s - T_a$) of 1K fails. This assumption often underlies satellite products, as T_a is often not known, implying a stability-independent C_e. Mean wind speeds of $\approx 5\ m/s$ and SST 5K below the overlying air, as frequently observed within upwelling regions, would for example cause a 'true' C_e, which is 50% below the applied one. On the other hand, highly unstable conditions associated with cold air outbreaks would reduce this error to roughly 10%, assuming moderate wind speeds of $10\ m/s$. Generally, strong wind conditions favour stratifications close to neutral ($\zeta \approx 0$), causing the computation of LHF to be primarily affected by the choice of C_e (*Zeng et al.* (1998)). This, however, may not be linked to the sea-air temperature difference, which nearly vanishes in the latter case, reducing the respective error in C_e to 2%. *Zeng et al.* (1998) concludes that the above-described examples are rare extremes, implying that the overall error of C_e is confined to several percent.

A comparison of several neutral exchange coefficients as a function of equivalent neutral wind speed (U_{10n}) based on TOGA COARE AND TOGA TAO[43] data is given in *Zeng et al.* (1998) (*Fig.8* therein). Results suggest the means of C_{qn} and C_{Tn} to take on values of $1.13 \cdot 10^{-3}$ for wind speeds ranging between $4 - 18\ m/s$, which is consistent with findings of *Smith* (1989) ($1.2 \cdot 10^{-3}$) and *Garratt* (1992) ($1.1 \cdot 10^{-3}$). Transfer coefficients based on wind speeds outlying this range are subject to considerable uncertainty, as also stated by *Bentamy et al.* (2003) in context of error considerations of C_e underlying satellite-based LHF. Nevertheless, large deviations among the individual algorithms are evident (*Zeng et al.* (1998), *Fig. 8a / b* therein). Respective mean values of ($1.13 \cdot 10^{-3}$) and ($1.198 \cdot 10^{-3}$) based on the Oceanet algorithm are found for c_{qn} and c_{Tn} (compare $C_{e,10n}$ and $C_{h,10n}$ in

[43]Data obtained within the framework of the Tropical Atmosphere Ocean (TAO) project, based on a moored array of 70 buoys which encompasses the whole tropical Pacific between $137°E$ - 95°W and 8°S - 9°S.

Eq. 19). However, the underlying relationship of the neutral transfer coefficients to U_{10n} is of linear nature, in contrast to results presented by *Zeng et al.* (1998) (*Fig. 8a / b* therein). In contrast to c_{qn} and c_{Tn}, c_{dn} tends to be in closer agreement (*Zeng et al.* (1998), *Fig. 8c* therein).

Zeng et al. (1998) argue that the observed neutral transfer coefficients may be modified by several percent, if the salinity effect (see further below) is not accounted for (as is the case for ERA data) as well as when measurements are obtained in shallow instead of deep waters. As *Eq. 8* indicates, this would directly impact the magnitude of LHF.

To account for actual wave conditions within coastal regions, *Taylor and Yelland* (2001) came up with a revised representation of z_0 (not explicitly depending on α), accounting for the height and steepness of the dominant waves. Although the respective formula is suggested to predict the neutral drag coefficient c_{dn} well over lakes and open ocean (*Taylor and Yelland* (2001)), *Fairall et al.* (2003) argue that consensus is still lacking as to its accuracy. Nevertheless, the Coare-based LHF shown in *Table 9*, *Table 10*, and *Fig. 4.2* (right) include this dependency on wave properties and may only account for minor discrepancies compared to Oceanet output (compare *Fig. 4.2*, left).

The impact of a variable von Kármán constant κ, which is proportional to the transfer coefficients and thus to LHF, can be ruled out within this work, as all underlying bulk flux algorithms refer to the most common choice of $\kappa = 0.4$ (*Hogstrom* (1988)). If deviations of κ were given, considerable LHF changes would have to be expected, as investigated within a satellite-based LHF intercomparison performed by *Chou et al.* (2003). A confrontation of zonal averages over global oceans (1992-1993) revealed an LHF overestimation of 11% therein when comparing GSSTF1 to GSSTF2[44] output, where respective κ where set to 0.45 and 0.4, respectively.

As the mean wind speed approaches calm conditions ($\leq 2\ m/s$, $\rightarrow 0\ m/s$), it has been shown that, in contrast to what one would expect from *Eq. 8*, LHF does not vanish. By means of eddy correlation measurements within the western equatorial Pacific, *Bradley et al.* (1991) have demonstrated that mean LHF become $\approx 25\ W/m^2$, which are caused by boundary layer eddies that transfer heat and moisture under unstable conditions. Based on the three underlying datasets of this work, LHF ranges between $15 - 17\ W/m^2$ under identical boundary conditions[45], confirming the findings of *Bradley et al.* (1991). The convective exchange is accounted for by adding a gustiness parameter $\beta*$ (e.g. *Zeng et al.* (1998)). Whereas this was not included within earlier versions of Coare and thus HOAPS (compare *Brunke and Zeng* (2002), *Table 1* therein), all datasets underlying this work account for this auxiliary term and hence LHF deviations among the datasets cannot be traced back to a different handling of gustiness parameterizations.

[44] Version 1 and 2 of the Goddard Satellite-based Surface Turbulent Fluxes (GSSTF), based on SSM/I radiances.

[45] This applies to 3.3%, 0.6%, and 3.7% of all Oceanet-, HOAPS-, and ERA wind speeds (10 m ASL), respectively.

As introduced in *Section 2.1 Kraus and Businger* (1994) demonstrate the dependency of q_s on oceanic salinity contents, the latter which reduces q_s by $\approx 2\%$. This depression may have considerable impacts on the air-sea humidity difference $q_s - q_a$, being most pronounced within tropical latitudes, where $q_s - q_a$ maximises. Both Oceanet- and HOAPS-based algorithms account for the salinity correction, whereas the ECMWF forecast model does not consider the effect. It can thus be concluded that the positively biased tropical LHF resolved by ERA (as indicated by *Fig. 4.3*), may to a great extend be associated with the omission of this correction term. *Brunke and Zeng* (2002) argue that this bias may become especially important for high wind speeds or stable conditions, the latter being subject to large algorithm deviations in general (*Chang and Grossman* (1999)). *Sud and Walker* (1997) quantified the bias based on TOGA TAO data and found deviations of $q_s - q_a$ of the order of $0.44\ g/kg$ (22% of the mean air-sea humidity difference) during wind speeds exceeding $14\ m/s$, eventually producing relative LHF- and evaporation biases of up to 10%. Conversely, a q_s-reduction by 2% lead to negligible LHF differences among the algorithms. Although restricted to the tropical Pacific, their results are thought to also apply to respective Atlantic latitudes.

5.2 Differences in Bulk Flux Input Parameters

5.2.1 LHF Considerations

As deduced in *Section 4.2*, HOAPS LHF are to a vast extend underestimated in comparison to respective Oceanet- and ERA-output. This conclusion has already been drawn within previous studies and been extensively discussed to date.

Compared with other satellite- and reanalysis based products, (*Kubota et al.* (2003)) have demonstrated that HOAPS LHF remain considerably smaller in lower latitudes[46], confirming the findings within this work. More specific, meridional profiles resolve HOAPS LHF remaining $20 - 50\ W/m^2$ (seasonally dependent) below those originating from the ECMWF forecast model in low latitudes (*Kubota et al.* (2003), *Fig. 5* therein), causing equatorial HOAPS-based LHF to be the smallest of all flux datasets.

The negative bias inherent to HOAPS LHF may, however, not be generalized. As also evident from *Table 11* and *Table 12*, *Liu et al.* (2011) point out that HOAPS LHF are higher within the Antarctic Circumpolar Current (ACC) region by up to $20 - 30\ W/m^2$ compared to several other flux sources[47]. This considerable bias cannot be confirmed within this work, which solely resolves a non-significant bias of $4.8\ W/m^2$ (8.8%) between HOAPS- and ERA-based LHF within $40°$-$60°$S (restricted to transit cruises).

Chou et al. (2003) performed a multi-year validation study of GSSTF2-based LHF based on ten ship-based measurement campaigns conducted within the tropics and mid-latitudes between 1991-

[46]The LHF comparison is performed among HOAPS, GSSTF, J-OFURO, ECMWF, NCEP1 reanalysis, and the da Silva observational dataset (*da Silva et al.* (1994)) between 1992-1994.

[47]Results are based on an intercomparison study of LHF data between 1989-2005, comprising output of HOAPS-3, NOCS2, NCEP2- and ERA-40 reanalysis, and OAFLUX.

1999. Amongst others, their analysis highlights zonal LHF averages between GSSTF2 and HOAPS during 1992-1993, which indicate a bias of $20 - 50\ W/m^2$ centered around $10°$ N/S (compare also *Chou et al.* (2004)). Again, this emphasizes the HOAPS-based LHF underestimation in tropical latitudes, which, according to *Chou et al.* (2003), is most likely due to different bulk flux inputs, as C_e deviations remain negligible.

Brunke and Zeng (2002) found HOAPS-based LHF to be underestimated by $\approx 30\ W/m^2$ during 1992-1993, compared to LHF obtained from TAO buoy measurements within the tropical Pacific. This is consistent with results of *Chou et al.* (2004) and the bias magnitudes are similar to respective mean deviations between HOAPS and Oceanet / ERA within this work, respectively (compare *Table 11* and *Table 12*). Expanding the focus to global oceans between 60°S-60°N, their average HOAPS-based LHF becomes $88.5\ W/m^2$ (*Brunke and Zeng* (2002)). This value is similar to results presented in *Section 4.2*, which suggest a mean HOAPS LHF of $83.9\ W/m^2$ within this latitudinal range (considering transits only). Furthermore, *Brunke and Zeng* (2002) conclude that the absolute difference of HOAPS- to GSSTF2 LHF maximises within 20°S-20°N, resulting in a bias of $-37\ W/m^2$ (-30.4%). The authors furthermore derive the monthly mean LHF difference between HOAPS and GEOS-1[48] to be $-16\ W/m^2$ and presume that it exists due to differences in the bulk input variables, which considerably differ during individual months. This anomalously large susceptibility of HOAPS-based LHF to seasonal variability has been subject to discussion among a Southern Ocean LHF intercomparison study (1988-2000) involving satellite- and reanalysis products[49] performed by *Yu et al.* (2011). Yet, this thought cannot be followed within this work, as the collocated data is latitudinally dependent restricted to specific seasons.

The large-scale LHF underestimation of HOAPS has given rise to discussions within literature as to its reliability compared to other satellite-based flux data. In summary, a lack of consensus exists concerning the representativeness of GSSTF2 versus HOAPS LHF output. Whereas *Chou et al.* (2004) argue that, based on comparison to high-quality observations, HOAPS resolves less realistic flux output, *Liu et al.* (2011) state that HOAPS LHF output may be considered as the most realistic[50]. The latter is also concluded by *Bourras* (2006)[51], who favours its application over the global oceans in contrast to J-OFURO and GSSTF2, amongst others.

Apart from a well-documented negative LHF bias associated with HOAPS, the ECMWF forecast model has been subject to discussions concerning its low latitudinal LHF overestimation. To name but one, *Brunke and Zeng* (2002) focused on the tropical ECMWF forecast model LHF bias by testing numerous bulk flux algorithms over the TAO array. Their *Fig. 2a/d* indicate a systematic ECMWF

[48] Reanalysis product of the Goddard Space Flight Center's Earth Observing System.

[49] GSSTF2, HOAPS-3, J-OFURO, ERA-40, and NCEP-2 LHF data.

[50] Both *Chou et al.* (2004) and *Liu et al.* (2011) refer to HOAPS-2 within their argumentation. Despite minor differences between HOAPS-2 and HOAPS-3, the overall negative LHF bias is inherent to both versions.

[51] Based on an intercomparison study of five LHF products within the tropical Pacific and mid-latitudes of the North Atlantic.

overestimation (compared to Coare2.5, amongst others) under all possible atmospheric stability conditions. Based on results of a satellite- and reanalysis intercomparison study restricted to 1996-1997, *Bentamy et al.* (2003) conclude that ECMWF forecast model LHF are overestimated by roughly 20% with regard to satellite[52] values. Results within *Section 4.2* confirm this, as a mean negative bias of $-16.5\ W/m^2$ arises when comparing HOAPS- to ERA LHF output (restricted to transit data only). *Bentamy et al.* (2003) presume this bias to originate from uncertainties in relating surface layer fields of the model to surface fluxes using a bulk formula.

In general, it should be noted that ECMWF forecast model output is fraught with uncertainty in latitudes, where only sparse in-situ observations exist. To a large extend, this accounts for the Southern Ocean region, where the density of assimilated data[53] remains low (*Kubota et al.* (2003)).

Rouault et al. (2003) investigated LHF discrepancies between ERA-40 reanalysis- and in-situ data in the vicinity of the Agulhas Current (Agulhas retroflection) in late April 1995 and found large discrepancies, owing to a considerable LHF underestimation (more than 25%) of ERA-40 LHF due to a negative SST bias of $2\ °C$. They concluded that ERA-40 inadequately captures the spatial representation of the warm core (width of 80-100 km) of the current and thus underestimates LHF. The authors assume this poor SST representation to originate from concurrent high cloud coverages, reducing the accuracy of AVHRR-based SST estimation This feature is also evident when comparing HOAPS- to ERA-LHF within the region of consideration ($38°$-$44°$S, $15°$-$35°$N) (not shown), yielding a positive LHF bias of $9.4\ W/m^2$.

5.2.2 Wind Speed Considerations

HOAPS near-surface wind speed biases have been subject to discussions within previous work. Some studies conclude that $\vec{u}$ represents the bulk flux parameter having the most essential impact on the LHF outcome (*Kubota et al.* (2003), amongst others).

However, this statement is mostly contradictory to the results within this work. Although LHF biases comparing HOAPS to Oceanet and ERA exceed an absolute mean of $20\ W/m^2$ (compare *Table 11* and *Table 12*) within the tropical Atlantic, concurrent wind speed biases to Oceanet (*Table 14*) and ERA (*Table 15*) remain low and to a great extend statistically non-significant. In comparison to ERA, HOAPS even overestimates $\vec{u}$ invariably. Furthermore, bias signs among LHF and $\vec{u}$ are also opposing within mid-latitudes and polewards (compare e.g. *Regions 1*, *3*, and *6*). These observations suggest bulk wind speeds to be less decisive in terms of concurrent LHF deviations.

[52] data obtained from European Remote Sensing (ERS) satellite scatterometer (*Version 2*), NASA scatterometer NSCAT, and SSM/I.

[53] This involves *RV Polarstern* data as well, as it represents an official meteorological station of the *German Weather Service*. Owing to this, *RV Polarstern*- and ERA data cannot be considered as entirely independent (see e.g. *Dee et al.* (2011)).

Among a LHF- and wind speed uncertainty intercomparison study of satellite products, *Bentamy et al.* (2003) stress the impact of bulk wind speed deviations on the resulting LHF. The authors exemplarily illustrate that a LHF bias of $10\ W/m^2$ results for SST ≤ 10 °C, if a bias of $1\ m/s$ in $\vec{u}$ is prescribed. These considerations may become important within (sub-)polar latitudes and could be the cause for local LHF biases shown in *Fig. 4.5* (bottom), which go along with biases in $\vec{u}$ of the same sign. Higher SST, as within the tropics, imply an even stronger impact of $\vec{u}$ on LHF, the bias of which may exceed $20\ W/m^2$ (as observed within this work, see *Table 11* and *Table 12*) for a wind speed bias of merely $1\ m/s$ (*Bentamy et al.* (2003)).

As *Section 4.3* suggests, HOAPS biases are not exclusively positive compared to the validation datasets. The latitudinal dependency of HOAPS-based $\vec{u}$ and its role in terms of LHF has been deduced by *Kubota et al.* (2003) in comparison to other satellite products. Based on a considerably negative LHF bias between HOAPS and J-OFURO observed within the tropics, the authors conclude that this offset is reduced by 50% within 20°S-20°N if one recalculates J-OFURO LHF based on HOAPS wind speeds (*Fig. 6* therein). Further intercomparison studies have revealed that HOAPS wind speeds tend to be larger in extratropics ($30 - 60°$ on each hemisphere (e.g. up to $2.0\ m/s$ compared to GSSTF2 in case of *Chou et al.* (2003)), centered around $50°$ N/S) than those of other satellite products. In contrast, the bias sign is reversed within (sub-)tropical latitudes between 30°S-30°N (up to $-2.0\ m/s$).

These conclusions somewhat resemble the findings within *Section 4.3*, replacing the compared satellite products by Oceanet- and ERA wind speed data, respectively. Here, extratropical biases of $\vec{u}$ are considerable, whereas tropical latitudes are subject to wind speeds of similar magnitude, the bias of which tends to be non-significant. Overall, meridional means of HOAPS-based $\vec{u}$ derived in *Section 4.3* exclusively exceed those listed by *Chou et al.* (2003) (*Table 3* therein) by $0.2\ m/s$ (20°S-20°N) to $0.9\ m/s$ (20°-60°S), reinforcing the reasoning of *Chou et al.* (2003) concerning an overrepresentation of $\vec{u}$ within HOAPS.

Aiming to elucidate the causes of wind speed biases among different flux products, *Winterfeldt et al.* (2010) explored the wind speed discrepancy along with one-hour means of HOAPS- to QuikSCAT[54]-, buoy-, and ship-based wind speeds between 1998-2002 within the Eastern North Atlantic and the North Sea (*Fig. 1* therein, similar to *Region 1* in *Fig. 4.6*). The authors argue that the mean HOAPS-based overrepresentation of $\vec{u}$ amounts to $0.9\ m/s$ (RMSE $\approx 2.3\ m/s$) compared to buoy winds, independent of the strictness of collocation criteria. Similarly, *Fig. 4.9* (bottom) indicates significant positive biases to Oceanet (and to ERA, see *Appendix, A. 4* (bottom)) within this region, which reach significant $1.9\ m/s$ on average (*Table 16*). Respective RMSE between 40°-60°N amount to $3.5\ m/s$ (transit data only: $4.0\ m/s$) and thus considerably outperform the error suggested

[54]NASA Quick Scatterometer, which measures surface winds speeds and -directions.

by *Winterfeldt et al.* (2010). However, mid- to high latitudinal oceans are subject to strongest mean wind speeds (compare *Fig. 4.8*), which favour high and gusty seas accompanied by a reduction of the anemometer accuracy installed on measurement platforms (*Gilhousen* (1987)). *Winterfeldt et al.* (2010) suggest that the RMSE may take on 20%[55] of measured $\vec{u}$, which would considerably impact the LHF outcome for $\vec{u} \geq 10\ m/s$. In 33% of all hourly measurements derived from *RV Polarstern* south (north) of $40°$S ($40°$N), the latter mean wind speed was exceeded, strengthening the importance of the inaccuracy considerations of wind speed measurements within high ranges.

It is presumed that the vicinity of shorelines exhibits a complicating impact on the HOAPS wind speed retrievals. In contrast to calm, deep seas, the transition of roughness lengths and the impact of friction within these shallow waters (associated with ageostrophic wind components during prevailing offshore winds) introduce considerable uncertainties.

These considerations may explain the large positive biases between France, Germany, and Norway, to focus on *Region 1*. On the basis of the uniquely strong positive wind speed biases associated with HOAPS between $40°$-$60°$N (relative deviations of 23.6% (30.8%) to Oceanet (ERA)), one may thus question the statement of *Winterfeldt et al.* (2010) that the HOAPS wind speed retrieval performs equally well in near-coastal and open ocean domains.

However, the coastal impact is unlikely to have the potential to cause such large near-coastal biases of $8.4 - 21.4\ m/s$ as observed off Greenland and Antarctica (*Fig. 4.9* (bottom) and *Appendix, A. 4* (bottom) in comparison to ERA). As these are also resolved when comparing HOAPS- to ERA-based $\vec{u}$ (see *Appendix, A. 4*, bottom), the HOAPS wind speed retrieval may be considered as the primary error source.

The latter regions were subject to a separate investigation, which revealed mean HOAPS-based wind speeds of $\approx 25\ m/s$, whereas both Oceanet- and ERA counterparts detected moderate wind speeds close to $10\ m/s$. Substantial ship- and reanalysis based biases may be ruled out, as the dark red shadings off Greenland in *Fig. 4.9* (bottom) exclusively rely on a continuous, multi-hour time series obtained in the second half of August 1997 (*RV Polarstern* campaign *ARK-XIII-3*, compare *Fig. 5.1*, left). The latter argumentation also holds for the cases off Antarctica (not shown), where 73% of all contributing data within the grid boxes of interest are part of continuous multi-hour to multi-day sub time series.

Instead, the vicinity of the seasonal ice edge most likely triggered the enormous deviations among HOAPS to the validation datasets (compare *Dee et al.* (2011) for general remarks on this). According to *Andersson et al.* (2011), grid boxes among the Pathfinder Version 5.0 SST dataset are flagged as ice-covered (which is coupled to an inhibition of the HOAPS-based LHF retrieval), in case the average sea ice fraction exceeds 15% for five successive days. This, however, implies that either the sea

[55] this value is proposed for *Ems* and *DeBu* (Bundesamt für Seeschifffahrt und Hydrographie (BSH)). Compare *Fig. 1* in *Winterfeldt et al.* (2010).

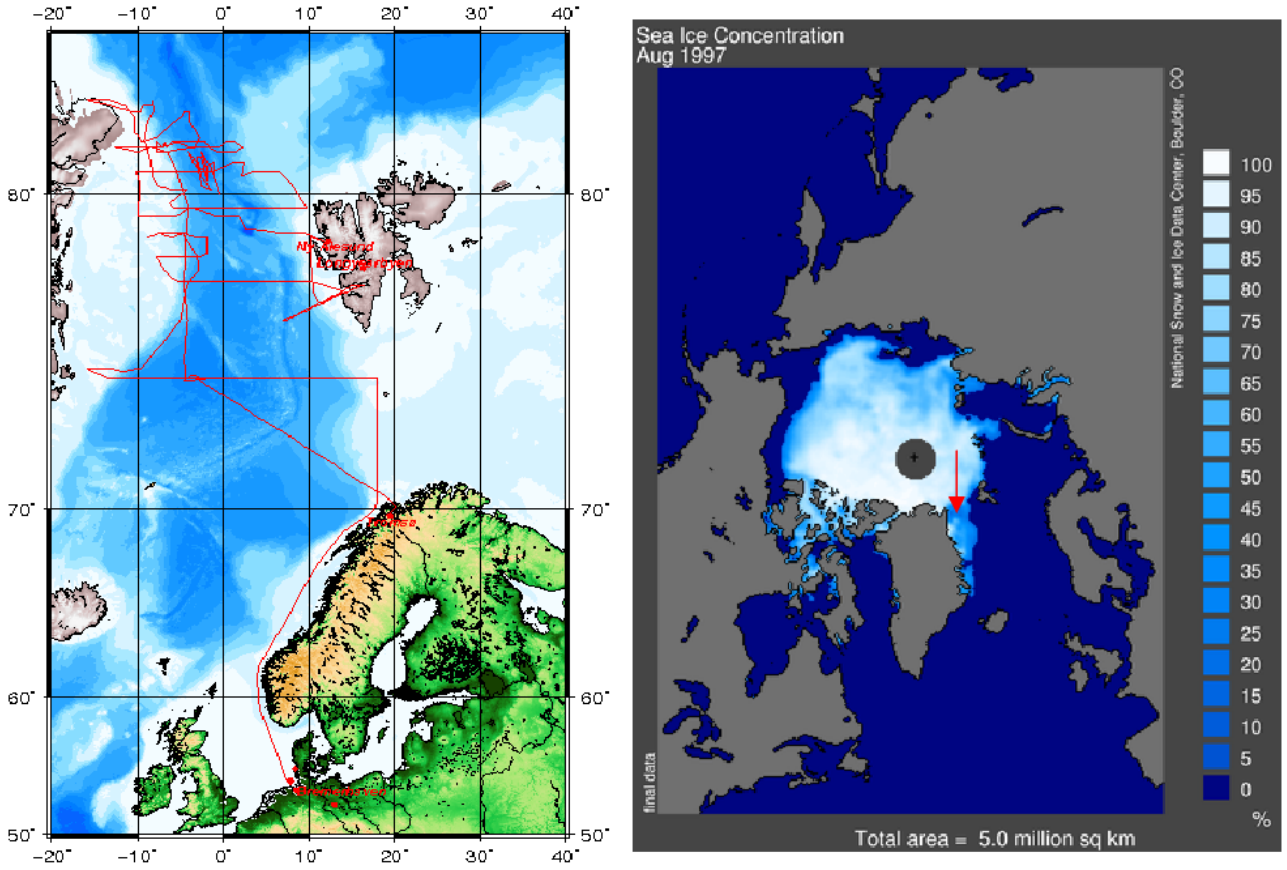

Fig. 5.1: Left: Cruise track of *RV Polarstern* during *ARK-XIII-3*. Adapted and modified from the *AWI Pangaea Database*. **Right:** Average sea ice coverage [%] during August 1997. The red error indicates the position of RV Polarstern, which is associated with immense wind speed biases as shown in *Fig. 4.9* (bottom left). Adapted and modified from the National Snow and Ice Data Center, Boulder, CO, USA.

ice fraction in the vicinity of *RV Polarstern* may have been considerably larger than the average, or collocation criteria were configured too generously within this region surrounded by strong spatial gradients in sea ice coverage. As *Fig. 5.1* (right) exemplarily depicts, noticeable sea ice concentrations were enclosing *RV Polarstern* in August 1997, the concentrations of which exceeded 80% to the north. Thus, it is suggested that the considerable wind speed biases originate from the perturbing influence of the sea ice. Same conclusions may be drawn for the biases off the Antarctic continent (not shown).

To the contrary, biases near 75°N / 0°E and within the ACC region remain negative within this work. *Winterfeldt et al.* (2010) identified a saturation of highest HOAPS wind speed percentiles, in as much as mean wind speeds exceeding $15\ m/s$ were underrepresented compared to buoy measurements (*Fig. 5*a therein). This transition to negative biases is also evident above $12\ m/s$ compared to Oceanet $\vec{u}$ (compare *Fig. 4.7*, left) and may explain the blue patches evident in high latitudes of both hemispheres (*Fig. 4.9* (bottom)). According to the authors, this is characteristic for HOAPS-based $\vec{u}$ and may be traced back to foam and wave crest blow-off in rough seas. It may additionally be introduced by the footprint, which may be larger than isolated areas of high winds, evoking an

underrepresentation of peak wind speeds within the HOAPS dataset.

In context of evaluating HOAPS-based surface fresh water flux components, *Andersson et al.* (2011) performed a comprehensive global ocean bias analysis of the individual climatological means of bulk input parameters between 1992-2005, amongst others encompassing ERA data. The authors identified several distinct features which are also evident among the results presented in *Section 4.3*. These comprise an overall HOAPS-based overestimation of $\vec{u}$ by up to $1.5\ m/s$. Furthermore, ship-based NOCS data (*Berry and Kent* (2009)) tends to significantly underestimate wind speeds at high latitudes, more specific by $3.5 - 4\ m/s$ south of $40°$S. *Table 14* suggests biases of similar magnitude for the Southern Ocean when comparing Oceanet- to HOAPS $\vec{u}$. Whereas *Andersson et al.* (2011) argue that the NOCS underestimation originates from a sparse data sampling density, the latter cannot be concluded for the Oceanet algorithm input, as 57% of all hourly observed data was obtained south of $40°$S.

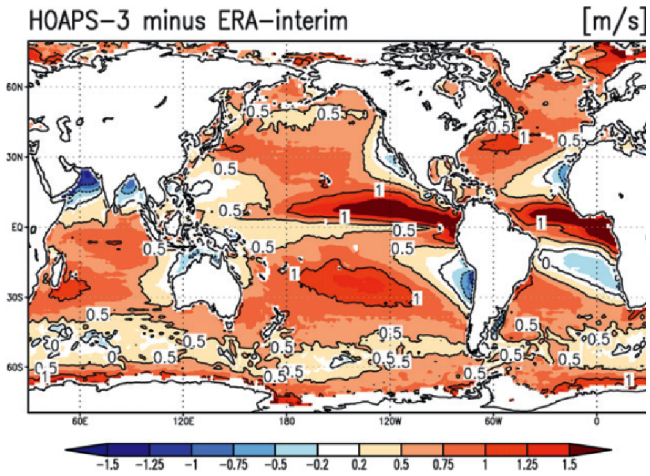

Fig. 5.2: Difference of the 1992-2005 climate mean HOAPS-3 wind speed and ERA. Adapted from *Andersson et al.* (2011).

In contrast, results of *Andersson et al.* (2011) resolve negative biases of up to $-1.0\ m/s$ between RSA and Brazil as well as off Cape Verde along the African Coast (compare *Fig. 5.2*). Comparable values of $\pm\ 0.5\ m/s$ between both sources are resolved within the ACC latitudes, which are slightly exceeded within this work (mean bias of $0.67\ m/s$).

Similar to findings illustrated in *Fig. 4.8* and *Table 15*, ERA remain lowest among all data sources[56]. According to *Andersson et al.* (2011), the global mean bias compared to HOAPS equals to $-0.6\ m/s$[57], which is close to estimates presented in *Section 4.3* based on transit data only ($-0.79\ m/s$), yet considerably smaller when considering all measurements ($-2.3\ m/s$). Comparison studies of satellite- and reanalysis-based wind speeds performed by *Meissner et al.* (2001) and *Monahan* (2006) conclude similar negative wind speed biases of ERA reanalysis data as *Andersson et al.* (2011). The former suggest the standard deviation of differences among SSM/I and ECMWF reanalysis to be $2.1\ m/s$ when considering all collocated data, which is similar to transit data results given in *Section 4.3*, yet only 45% when considering all cruises within this work. The latter goes back to the fact that the basin-scale mean of HOAPS $\vec{u}$ amounts to $9.77\ m/s$ (transit only: $7.95\ m/s$) (ERA: $7.47\ m/s$ (transit only: $7.17\ m/s$)), whereas the mean of SSM/I retrieved wind speeds suggested by *Meissner et al.* (2001) is given by

[56] Amongst HOAPS-3 and ERA, these also comprise NOC- (National Oceanography Centre Southampton, *Berry and Kent* (2009)) and IFREMER (Institut Francais de Recherche pour l'Exploration de la Mer, *Bentamy et al.* (2003)) data.

[57] This is close to estimates performed by *Bentamy et al.* (2003), who suggest a positive wind speed bias of $0.48\ m/s$ when comparing SSM/I- to ECMWF forecast model estimates of $\vec{u}$.

only $7.3\ m/s$.

Andersson et al. (2011) propose the Atlantic mean bias between HOAPS and ERA, which equals to 30.7% (11.0% for transit data only) following *Section 4.3*, to partly originate from different principles applied for wind speed retrieval. Whereas reanalysis models simulate the actual wind speeds at 10 m ASL, SSM/I-based wind speeds are derived indirectly from surface wind stress data, which is recalculated to equivalent neutral stability wind speeds at 10 m ASL.

However, the sparse in-situ measurements, which constitute a significant part of the data assimilation scheme of ERA, may partly account for locally different $\vec{u}$ (*Meissner et al.* (2001)) and may explain the significant wind speed bias to HOAPS of $-4.88\ m/s$ ($-3.84\ m/s$) south (north) of $60°$S ($60°$N), corresponding to relative deviations of -72.5% (-55.1%).

Additionally, deviations between HOAPS and ERA wind speeds are associated with boundary conditions of the sea surface state as previously described by *Quilfen et al.* (2000) among an intercomparison of different satellite-based wind speed data.

In contrast to satellite retrievals, ERA presumes a static sea surface, which may lead to a systematic misrepresentation of $\vec{u}$ in regions of strong, confined surface ocean currents, which propagate along the prevailing wind direction. The latter has been investigated by *Meissner et al.* (2001) among a 10-year intercomparison study of SSM/I and reanalyses wind speed retrievals from 1987-1997[58]. Results indicate that both reanalyses products significantly overestimate $\vec{u}$ with respect to SSM/I output (up to $3\ m/s$) along upwelling regions off Mauritania and Namibia (compare *Plate 1 / Plate 2* therein), where both oceanic currents (Canary Current to the north, Benguela Current to the south) and prevailing winds propagate equatorwards along the coastline (depending on season). This mechanism may account for the negative biases within the Eastern Subtropical Atlantic illustrated in *Fig. 5.2*. *Fig. 5.3* exemplarily illustrates the current-wind-relationship referring to buoy- and scatterometer measurements, which may be replaced by Oceanet (or ERA) and HOAPS, respectively.

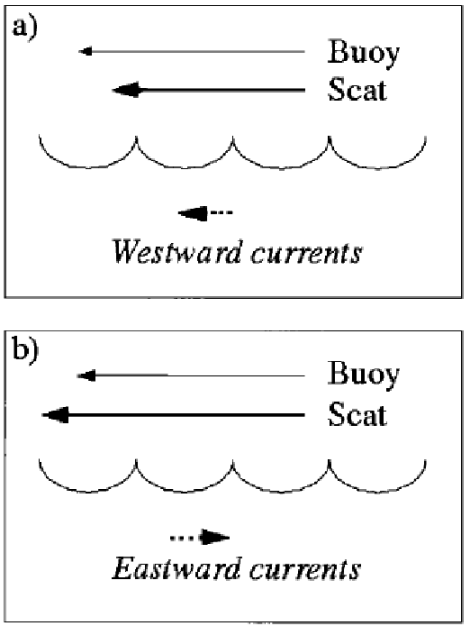

Fig. 5.3: Schematic of the buoy wind vectors, scatterometer vectors, and ocean current for (a) currents aligned with the winds and (b) currents opposing the winds. Adapted from *Kelly et al.* (2001).

The supplemental contribution to the formation of surface gravity waves have an additional perturbing effect (*Meissner et al.* (2001)), further enhancing the existing offset. Based on *Section 4.3*, a bias analysis between HOAPS and ERA indicates several, yet confined significant negative biases

[58]F-11 SSM/I were compared to NCEP/NCAR reanalysis- and ECMWF forecast model output.

off Mauretania (see *Appendix, A. 4*, bottom), but not off Namibia[59]. Focusing on three transit cruises, the cruise tracks of which lay close to Mauretania[60], an overall negative bias of $-0.75\ m/s$ results, strengthening the hypothesis of *Meissner et al.* (2001). The authors not only emphasize the impact of surface currents themselves on the wind speed retrieval, but also anomalous SST associated with upwelling events, why may lead to inaccuracies of the radiative transfer model function for T_B, eventually exerting an impact on the SSM/I retrievals and hence the satellite-based $\vec{u}$.

Furthermore, (*Fig. 4.9*, bottom) indicates that wind speed biases between HOAPS and Oceanet are exclusively negative within the southern hemispheric (sub-)tropics, exhibiting absolute maxima off Namibia. As the Oceanet algorithm also assumes a current velocity of $0\ m/s$, winds may be overrepresented within Oceanet in this region, explaining part of the observed significant bias of $-1.1\ m/s$ in *Region 4* (*Table 16*).

In case of meridionally orientated mean wind speeds, *Meissner et al.* (2001) (*Fig. 6*, bottom therein) points out the existence of elevated biases of $0.7\ m/s$ between HOAPS and ECMWF during the descending compared to the ascending counterpart of the SSM/I orbit. As exemplarily discussed for subtropical southern latitudes off the Namibian coast, where prevailing winds blow northwards, it is suggested that the bias is elevated during upwind conditions, as apparent during the morning descend. This agrees with previous analysis reported by *Wentz* (1997) and may explain the significant overestimation of HOAPS-based $\vec{u}$ compared to the validation datasets among *Section 4.3*. If respective HOAPS-S data had differentiated between morning / evening overpasses, wind speed biases may have locally been considerably lower.

As the wind speed retrieval is inhibited under strong precipitation events[61], regions of frequent precipitating weather systems, such as the ITCZ and the Southern Ocean, are subject to higher uncertainties within the HOAPS-based wind speeds (*Andersson et al.* (2010)). The precipitation effect comprises $\approx$ 10-15% of all pixels within the respective areas (*Andersson et al.* (2010)). Whereas the ICTZ impact is negligible ($0.6 - 1.0\%$ of all data underlying *Section 4.3* would be affected), the uncertainty inherent to southern extratropical latitudinal $\vec{u}$ cannot be excluded and needs further consideration.

[59] although two cruises were conducted during late boreal autumn and winter, the seasons of which exhibit highest biases in $\vec{u}$ according to *Meissner et al.* (2001). A higher measurement density within *Region 4* may have resolved the conclusions suggested by *Meissner et al.* (2001). In this context, *Liu et al.* (1998) discovered ECMWF winds to be missing the continental influence off Namibia, resulting in large deviations within the zonal wind components between ECMWF forecasts model output and NSCAT data. They conclude this to be caused by sharp gradients, which are typically smoothed over by forecast products such as the ECMWF-based data.

[60] ANT-13/1, ANT-14/4, and ANT-15/1.

[61] The liquid- and ice phase in clouds and precipitation considerably changes the atmospheric radiative properties within the micro wave spectrum, which executes a direct impact on the radiometer signal (*Andersson et al.* (2010)).

5.2.3 Specific Humidity- and SST Considerations

As *Section 4.2* overall reveals significantly negative LHF biases, but *Section 4.3* significantly positive wind speed biases with respect to HOAPS, a large contribution to the former within this work is likely to originate from considerable specific humidity discrepancies and/or air-sea humidity differences. Identical conclusions are drawn by *Andersson et al.* (2011) for tropical latitudes, who argue that large-scale deviations of LHF and thus evaporation estimates among HOAPS and ERA are associated with differences in q_a, whereas bulk-$\vec{u}$ and q_s are considered to be of secondary order. Their findings are confirmed within this work, resolving significant positive biases of $0.53\ g/kg$ ($0.70\ g/kg$) compared to Oceanet (ERA) between $20°$S-$20°$N, complying with 4.1% (5.1%). Likewise, *Yu et al.* (2011) discovered differences in Southern Ocean spatial LHF distributions to not appear to be linked to wind speed deviations among satellite- and reanalysis products[62], but moreover to temperature- and humidity differences between surface and atmosphere.

In addition, *Bentamy et al.* (2003) identified the main source of deviations between satellite and ECMWF LHF to be associated as well with biases of q_a. Assuming prevailing q_a anomalies of $1.8\ g/kg$ (as observed in regions where ECMWF-based LHF considerably exceed those of SSM/I), the authors exemplarily conclude that LHF biases are of the order of $-50\ W/m^2$, assuming SST and $\vec{u}$ to be 16 °C and $11\ m/s$, respectively. An investigation between HOAPS and ERA within this work (presuming a positive q_a bias $\geq 1\ g/kg$) even exceeds this LHF bias magnitude, which reaches $-74.8\ W/m^2$, and identifies these regions to be located close to $40°$ N/S and $3°$-$14°$W. Alternatively, the LHF bias due to a q_a bias of $1\ g/kg$ exceeds $-20\ W/m^2$, assuming wind speeds of $\geq 7\ m/s$. Focusing on $40°$-$60°$N, where the prerequisites conditions are fulfilled, yields a mean LHF bias of $-34.0\ W/m^2$ ($-16.9\ W/m^2$) between HOAPS and Oceanet (ERA) within this work.

Multiple intercomparison studies have recently investigated the q_a anomaly inherent to the HOAPS data source. Consensus is reached on the observation that near-surface specific humidity exhibits a positive bias within the tropical latitudes (*Andersson et al.* (2011), *Jost et al.* (2002), e.g.), as is also consolidated in *Fig. 4.11*, *Table 18*, and *Table 19*.

Comparing monthly mean q_a originating from HOAPS to GSSTF2 and other satellite-based products between 1992-1993, *Chou et al.* (2003) discovered a wet bias of $0.4 - 1.3\ g/kg$ over global oceans, which maximises to $1 - 1.3\ g/kg$ between $15°$S-$15°$N and conclude a HOAPS-based overrepresentation of q_a to be apparent, as it outperforms the already anomalously high values given by GSSTF2. The bias magnitude resembles that of HOAPS in comparison to ERA (Oceanet), which reaches significant $0.89\ g/kg$ ($0.47\ g/kg$) between $20°$S-$20°$N.

As biases of q_s generally remain considerably smaller (owing to the high accuracy of AVHRR SST retrieval, on which q_s depends), HOAPS-based $q_s - q_a$ remain below those of GSSTF2 by $0.5 - 1\ g/kg$ in the areas equatorward of $20°$ N/S. This is consistent with findings of *Brunke and Zeng* (2002),

[62] HOAPS-3, GSSTF2, J-OFURO, NCEP-2, and ERA-40.

suggesting the HOAPS-based $q_s - q_a$ to be underestimated by $0.5 - 1\ g/kg$ during 1992-1993 in comparison to TAO buoy data within the equatorial Pacific.

Chou et al. (2003) further specify the tropical overestimation of HOAPS q_a to be a crucial cause for the observed negative LHF bias of $37\ W/m^2$ to GSSTF2. The latter may also be concluded in context of comparing HOAPS to the validation datasets within *Section 4.4*, although the presented HOAPS-based latitudinal means in *Chou et al.* (2003) (*Table 5* therein) remain lower within this work by 0-10%. Yet, LHF biases indicated in *Table 11* and *Table 12* are considerable, owing to comparatively small q_s compared to findings in *Chou et al.* (2003) (*Table 5* therein), where $q_s - q_a$ within this work is on average 5-24% larger.

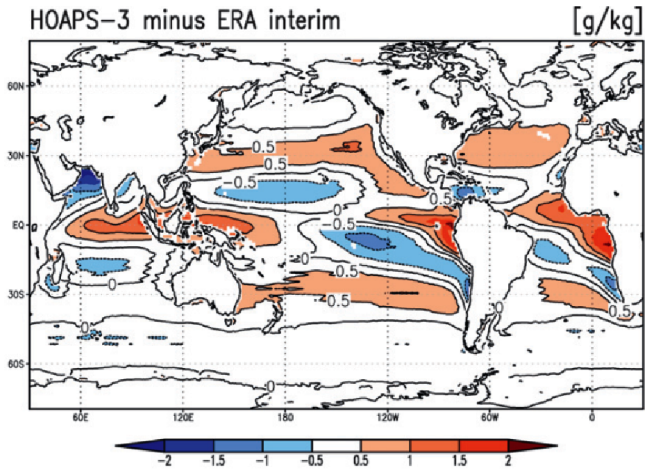

Fig. 5.4: Difference of the 1992-2005 climate mean HOAPS-3 near-surface specific humidity and ERA. Adapted from *Andersson et al.* (2011).

In the context of low wind regimes, *Bentamy et al.* (2003) recall that $q_s - q_a$ only represents an approximation of the neutral equivalent humidity difference. In light wind conditions, where the atmospheric stratification is either strongly stable (upwelling regimes) or unstable (ITCZ), this may introduce regional biases in air-sea humidity differences and thus LHF. On climatological scales, this effect may be negligible, apart from the fact that near-neutral stratifications are dominant on a basin-wide scale. However, as the underlying work does not allow for the establishment of a comprehensive climatological data basis, this statement of *Bentamy et al.* (2003) may not hold for comparisons involving HOAPS pixel-scan resolution data.

In contrast, *Jost et al.* (2002) identify negative biases of q_a within the Southern Ocean (down to $-1.0\ g/kg$ with respect to the SOC[63] climatology), which, coupled to anomalously strong wind speeds yields positive anomalies of LHF. This is confirmed within this work, as indicated by the significant negative bias in q_a ($-0.23\ g/kg$) and the concurrent significant bias in LHF ($10.01\ W/m^2$) shown in *Region 5* (*Table 17*). As $q_s - q_a$ is significantly positive ($0.14\ g/kg$), the Atlantic sector of the Southern Ocean may be seen as a region of excessive evaporation (*Andersson et al.* (2011)), which distinguishes it from much of the remaining southern basin. According to *Liu et al.* (2011), this bias may become even more important in future, as interannual trends between 1989-2005 within the ACC region indicate pronounced positive trends of HOAPS-based $\vec{u}$ and $q_s - q_a$ (associated with positive trends of LHF observed within the early 1990's), whereas ERA-40 reanalysis data exhibits opposite trends within the Central Southern Atlantic.

[63] Southampton Oceanography Centre

Regional analysis is performed by *Andersson et al.* (2011), who lie the focus on the considerable positive bias of q_a between HOAPS and ERA along the Atlantic eastern boundary (also resolved within this work, see *Appendix, A. 5*), which locally exceeds $2\ g/kg$ (20%) in the climatological mean, as is illustrated in *Fig. 5.4*.

Albeit SST deviations remain small among different datasets compared to respective q_a anomalies on a climatological scale, the positive q_a bias is supplemented by a negative SST anomaly in the (sub-)tropical eastern Atlantic (*Andersson et al.* (2011)), which dampens q_s and eventually causes even larger negative LHF compared to the latitudinal mean. This HOAPS SST bias, which is (especially) resolved within this work along 0°-20°N (-0.5 °C, compare *Table 22*) has recently been subject to discussion. The authors suspect it to origin from shortcomings in the AVHRR dataset, as high aerosol loadings, originating from the arid desert areas on the African continent, hinder the proper error correction within the SST retrieval algorithm.

The sensitivity of LHF to SST biases may be substantial (*Bentamy et al.* (2003)). Prescribing a SST bias of 1 °C (SST ≥ 10 °C) and assuming $\vec{u} \geq 7\ m/s$, LHF deviations typically exceed $10\ W/m^2$. This approximation is by far overstepped when considering the latitudinal range of 0°-20°N and a confrontation of HOAPS and ERA within this work. As the former underestimates SST by 0.5 °C ($\overline{SST_H}$: 26.3 °C), a negative LHF bias of $26.5\ W/m^2$ (25.6%) results.

Jost et al. (2002) already pursued the issue of SST biases associated with AVHRR data during an early spring measurement campaign along the West Spitsbergen Current, inferring considerable negative SST biases, which reduced q_s and eventually LHF[64]. It is concluded that undetected low-level or thin cirrus clouds favour the formation of substantial cold biases in the derived SST. In general, the latter may be even enhanced during the dark season in high latitudes, which force the application of error-prone night-time cloud detection schemes.

Andersson et al. (2011) suggest a global mean q_a bias of $0.13\ g/kg$, which is evaluated as a substantial improvement compared to results published in *Chou et al.* (2004) and *Brunke and Zeng* (2002). However, the bias corresponds to only 22% of the basin-scale bias shown in *Table 19* ($0.57\ g/kg$), the latter possibly owing to the confined time period considered. This strengthens the hypothesis that LHF biases underlying this work are to a large extend generated by systematic q_a deviations.

5.3 Concluding Remarks on the Applied Methodology

Decorrelation time- and length scales (Γ, Υ) were derived in *Section 3.2*, on the basis of which the collocation of HOAPS- to Oceanet and ERA data was performed. Although final collocation criteria were chosen to be strict, in as much as the bulk flux parameter exhibiting the smallest decorrela-

[64] compared to bulk flux measurements obtained on *RV Valdivia* and the bulk flux algorithm application of *Smith* (1988).

tion scales (i.e. $\vec{u}$) served as the reference for all other parameters, one could argue that significant LHF biases shown in *Fig. 4.5* (bottom), *Table 11*, and *Table 12* partly originate from a too generous treatment of permitted temporal and spatial distances. Following a sensitivity analysis similar to *Winterfeldt et al.* (2010) (compare *Table IV* therein), this potential bias source was examined within this study. Here, all possible combinations of decorrelation time- and length scales were tested on LHF RMSE and -bias, where the former [min] were chosen to be [30, 60, 90, 120, 150, 180] and the latter [km] were set to [20, 40, 60]. Confronting HOAPS- and Oceanet- (ERA-) based LHF, results indicate an overall RMSE range of $25.9 - 27.4\ W/m^2$ ($25.1 - 26.9\ W/m^2$) as well as biases between $-5.0\ W/m^2$ and $-7.1\ W/m^2$ ($-4.8\ W/m^2$ and $-7.1\ W/m^2$). The bias ratio of most generous ($150\text{min} \leq \Gamma \leq 180\text{min}$, $40\text{ km} \leq \Upsilon \leq 60\text{ km}$) and most restrictive ($\Gamma \leq 30\text{min}$, $\Upsilon \leq 20\text{ km}$) criteria remains even ≤ 1, implying a bias reduction of 10% (13%). Hence, the chosen collocation thresholds within *Section 3.2* are unlikely to account for significant biases observed in *Section 4.2*.

The RMSE- and bias independency of Υ is likely due to the coarse spatial resolution of HOAPS (*Winterfeldt et al.* (2010)), the footprint of which is ≈ 50 km and thus hardly smaller than the most liberal Υ of 60 km.

A technical memorandum by *Kaallberg* (2011) addresses the issue of ERA accumulated fields, as their forecasts are prone to spin-up problems, which may influence the quality of short-term LHF forecasts. Thus, a decision has to be made as to which forecast step to apply. To approach this concern, the regression illustrated in *Fig. 4.4* (right) was re-performed (not shown), restricted to ERA forecast steps of three, six, nine, and twelve hours, respectively. As noteworthy regressional improvements could not be diagnosed, the spin-up difficulty may be ruled out in context of reducing the reanalysis-based LHF accuracy.

Within this study, three different data products were averaged in time and space for validation purposes. However, the original resolutions of data obtained from *RV Polarstern*, HOAPS, and ERA considerably differ in their temporal and spatial resolution. *Kubota et al.* (2003) suggests that differences in LHF estimates may partly be a consequence of this data manipulation. This specifically applies to the four-point averaging procedure performed within *Section 2.3*. Due to spatial averaging, the latter approach smoothes out local maxima or minima, which eventually underestimates largest and overestimates smallest LHF, as also resolved within the extremes of *Fig. 4.4* (right, see squares). *Meissner et al.* (2001) further argue that the reanalysis match-ups do not provide real measurements, inhibiting the effort to quantify the accuracy of the reanalysis-based parameters on the basis of derived standard deviations. However, this potential bias source is minimized within this work, as weighted instead of arithmetic means are derived. Despite strong spatial LHF gradients, as e.g. observed off RSA and south of Svalbard (*Fig. 4.5*, top), their occurrence remains rare, suggesting the four point averaging procedure to represent the most accurate approach to account for the considerable resolution differences among ERA- and HOAPS / Oceanet datasets.

The validation analysis performed within *Section 4* relies on HOAPS events, i.e. on arithmetic means of individual HOAPS-pixels, which fulfils the collocation criteria to one hourly-mean ship and ERA data. These averages may have locally caused low-biased LHF, as 11.8% of applied pixels suggest $LHF = 0\,W/m^2$, owing to exclusively concurrent $q_s - q_a = 0\,g/kg$. The cause for this frequent equality of air-sea humidity difference, which to 87% occurs within (sub-)polar oceans south (north) of $50°$S ($50°$N), is not known and needs further investigation within future analysis. The average of concurrent Oceanet-based LHF equals to $13\,W/m^2$, suggesting difficulties within the HOAPS-based specific humidity retrieval in an environment of very low LHF.

A general remark applies to the uncertainty of measurements of bulk flux parameters on *RV Polarstern* within strongly stable atmospheric stratification. These environments favour shallow planetary boundary layers, the vertical extend of which may remain below the measurement heights of $\vec{u}$ and RH. *Businger et al.* (1971) recall that strictly speaking, MOS-Theory is not applicable in these cases, as the bulk flux equations remain invalid. However, these critical cases are strongly confined in time and space (along upwelling regimes or wintertime stationary temperature inversions) and may thus account for negligible uncertainties in the bulk flux algorithm outputs. As for the in-situ data, bulk parameters cannot be inferred in substantially lower heights owing to considerable flow distortions on research vessels, the impact of which might exceed the concerns of *Businger et al.* (1971) by far.

6 Conclusions and Outlook

Having discussed potential uncertainty sources among the parameterizations and bulk input parameters within *Section 5*, the question remains as to the relative importance of both factors.

To qualitatively solve this issue, *Fig. 6.1* illustrates ratios of all bulk input parameters contributing to *Eq. 8*, where

$$\rho \ [kg/m^3] = \frac{100 \cdot SLP}{287.05 \cdot T_{v,10m}} \tag{28a}$$

$$T_{v,10m} \ [K] = (1 + 0.001 \cdot 0.608 q_{10m}) \cdot (SAT_{10m} + 273.15) \tag{28b}$$

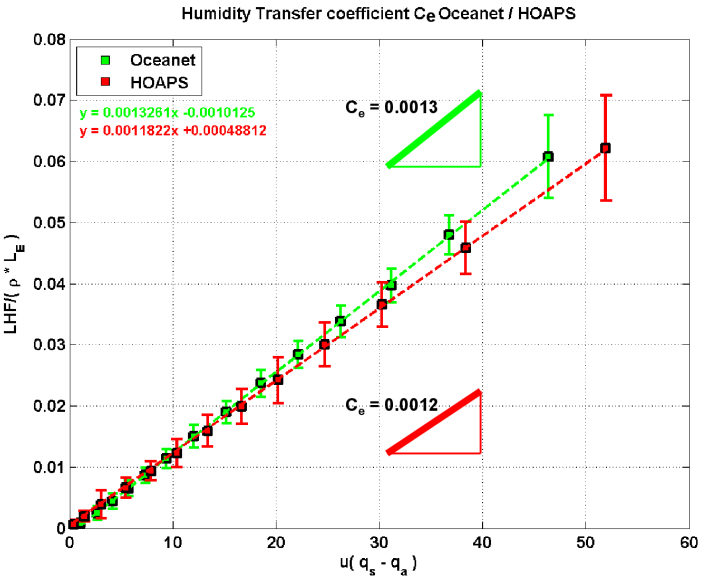

Fig. 6.1: Ratio of bulk input parameters to the LHF equation (8). Here, (8) is solved for C_e, which is represented by the slopes of the red (HOAPS) and green (Oceanet) linear fit, respectively. ERA is excluded, as no q_s data is available.

T_v corresponds to the virtual potential temperature. The minor SST-dependency of L_E included in *Fig. 31* has been neglected, implying it to be constant ($L_E = 2500kJ/mol$).

As indicated by *Eq. 8* and illustrated in *Fig. 6.1*, the slopes of the best-fit lines display the respective parameterization-based exchange coefficients C_e. Although the Oceanet-based value (0.0013) slightly exceeds the counterpart of HOAPS (0.0012), both lie within the uncertainty range of transfer coefficients for humidity. Keeping in mind that LHF originating from HOAPS and Oceanet result from two independent bulk flux algorithms, this result is fairly desirable.

Hence, it becomes obvious that the significant LHF biases of HOAPS in comparison to its in-situ validation dataset are predominantly due to deviations among the bulk input parameters, whereas considerable parameterization deficiencies can be ruled out. *Section 4* identified HOAPS-based q_a to be the most significant biased bulk parameter, which confirms findings of previous studies discussed within *Section 5.2.3*.

As brought up in *Section 1*, biased LHF ultimately excite error-prone evaporation estimates, the latter which may be expressed as

$$E\ [mm/h] = \frac{LHF}{L_E \cdot \rho_0}, \tag{29}$$

where ρ_0 is the freshwater density as a function of temperature.

E constitutes one of the components establishing the freshwater cycle, which is supplemented by precipitation estimates P. Their climatological field is illustrated in *Fig. 6.2*, which brings out the familiar pattern of precipitation deficits over the subtropical oceans and respective excesses within the ITCZ region. Accounting for all major ocean basins, HOAPS suggests a mean net transport of freshwater from the global ice-free ocean to the atmosphere of 0.73 mm/day (*Andersson et al.* (2011)), which is mostly[65] compensated by continental run-off for a closure of the freshwater balance. However, *Andersson et al.* (2011) argue that the continental compensation remains in the order of 0.33 mm/d, implying a HOAPS freshwater imbalance of $\approx$ 0.4 mm/day to date (10-15% of the individual global estimates of E and P). Although this mismatch has been reduced by $\approx$ 47% in comparison to HOAPS-2 due to the implementation of a revised precipitation algorithm[66], it exceeds the statistical uncertainty of the global mean freshwater flux time series (*Andersson et al.* (2011)).

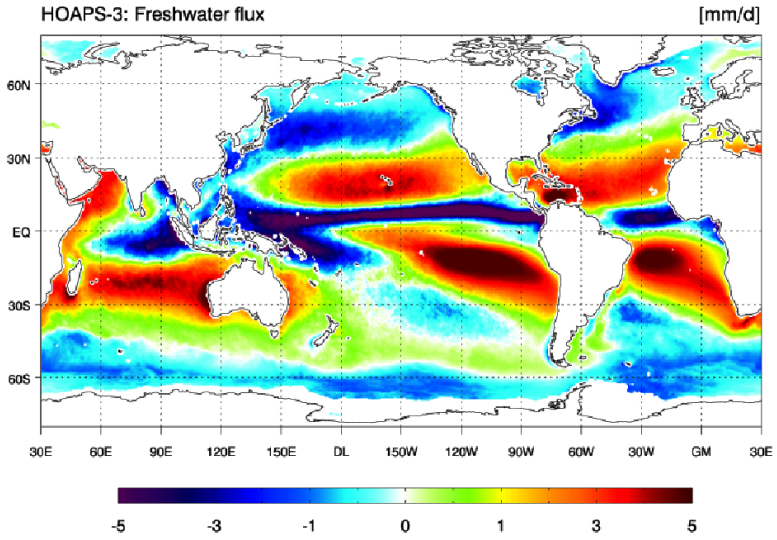

Fig. 6.2: Climatological mean field of HOAPS-3 freshwater flux $E-P$ for 1988-2005. Positive values indicate an evaporation excess. Adapted from *Andersson et al.* (2010).

Future work aims to include investigations of HOAPS-based scan-oriented precipitation estimates to validate the high-resolution freshwater cycle $E-P$. Its accurate representation cannot be overstressed when carrying out local and global trend analysis, as it controls the thermohaline circulation. Contemplable bias sources within both LHF (eventually E) and P need to be further constrained and quantified, preferentially in light of the significant q_a biases within HOAPS. Respective investigations based on the most recent HOAPS dataset, HOAPS3-2[67], may offer valuable clues as to the relative importance of individual bias sources.

Satellite-based techniques to retrieve SAT may need to be optimized, in as much as latitudinally-adjusted relative humidities and air-sea temperature differences would procure a SAT- and conse-

[65] annual ice melt and ground water flow only account for $\approx$ 10% of the river discharge (*Burnett et al.* (2001)).

[66] The climatological mean precipitation estimates of HOAPS-2 were substantially lower, compare *Andersson et al.* (2011).

[67] Electronic publication, *doi:10.5676/EUM_SAF_CM/HOAPS/V001*.

quently stratification- and LHF bias reduction. Overall, an extensive assessment of long-term stability issues inherent to the satellite-based climatology remains an essential task within future validation studies (*Andersson et al.* (2011)).

Aiming to corroborate the presented validation results, more high-quality observations are of need to eventually support bulk flux algorithm improvements. The inclusion of buoy data would provide a basis for relying on a higher in-situ data density and thus to substantiate regional strengths and weaknesses of HOAPS. This especially applies to the considerably biased (sub-)tropical regions, which remain undersampled within this work.

In addition to the suggested improvements for the in-situ data acquisition, budget closure deficits are inherent to the components of the ERA freshwater cycle. Its representation remains challenging, as precipitation estimates are produced by the forecast model, whereas respective input parameters originate from data assimilation (*Dee et al.* (2011)). This implies that imbalances in the analysed fields may cause substantial forecast variations. Excessive tropical precipitation biases still contribute to an incorrect spatial distribution to date (*Andersson et al.* (2011)), putting the ERA freshwater budget closure at risk[68].

Highlighting the recent considerable improvements of the HOAPS' hydrological budget representation and its promising performance in comparison to numerous other satellite-based flux products[69], the HOAPS climatology has the growing potential to provide consistent and homogeneous fields of evaporation (including LHF), precipitation, and thus the resulting freshwater flux. Its unique spatial and temporal resolution will continue to allow for monitoring surface fluxes from space with increasing accuracy, serving as a valuable verification source of coupled AOGCM's.

[68] However, the remaining ERA-based $E - P$ imbalances of 0.2 mm/day are smaller than the satellite-based estimates (*Andersson et al.* (2011)).

[69] see also conclusions for mid- and high latitudes within *Klepp et al.* (2010).

References

Andersson, A., K. Fennig, C. Klepp, S. Bakan, H. Grassl, and J. Schulz (2010), The Hamburg Ocean Atmosphere Parameters and Fluxes from Satellite Data HOAPS-3, *Earth Syst. Sci. Data*, *2*, 215–234.

Andersson, A., C. Klepp, K. Fennig, S. Bakan, H. Grassl, and J. Schulz (2011), Evaluation of HOAPS-3 Ocean Surface Freshwater Flux Components, *Journal of Applied Meteorology and Climatology*, *50*, 379–398.

Andersson, E., and H. Järvinen (1999), Variational quality control, *Q. J. R. Meteorol. Soc.*, *125*, 697–722.

Arntz, W., and J. Gutt (1997), The expedition ANTARKTIS XIII/3 (EASIZ I) of "Polarstern" to the eastern Weddell Sea in 1996, *Reports on Polar Research*, *249*, 1–148.

Arya, S. P. (2001), *Introduction to Micrometeorology*, Holton, J.R., Academic Press.

Augstein, E. (1997), The expedition ARCTIC '96 of RV "Polarstern" (ARK XII) with the Arctic Climate System Study (ACSYS), *Reports on Polar Research*, *234*, 1–54.

Barton, I. J. (1995), Satellite-derived sea surface temperatures: Current status, *J. Geophys. Res.*, *100*, 8777–8790.

Bathmann, U., M. Lucas, and V. Smetacek (1997), Die Expeditionen ANTARKTIS XIII/1-2 des Forschungsschiffes "POLARSTERN" 1995/96, *Reports on Polar Research*, *221*, 1–136.

Baumgartner, A., and E. Reichel (1977), *The World Water Balance*, Elsevier Science.

Beljaars, A. C. M. (1994), The parametrization of surface fluxes in large-scale models under free convection, *Q. J. R. Meteorol. Soc.*, *121*, 255–270.

Beljaars, A. C. M. (1995), The parameterization of surface fluxes in large-scale models under free convection, *Q.J.R. Meteorol. Soc.*, *221*, 255–270.

Beljaars, A. C. M., and A. A. M. Holtslag (1991), Flux Parameterization Over Land surface for Atmospheric Models, *J. Appl. Meteor.*, *30*, 327–341.

Bentamy, A., K. Katsaros, A. M. Mestas-Nuñez, W. M. Drennan, E. B. Forde, and H. Roquet (2003), Satellite Estimates of Wind Speed and Latent Heat Flux over the Global Oceans, *Journal of Climate*, *16*, 637–656.

Berrisford, P., et al. (2011), The ERA-Interim Archive, Version 2.0, *Tech. rep.*, ECMWF, Reading, UK.

Berry, D. I., and E. C. Kent (2009), A new air-sea interaction gridded datdata from ICOADS with uncertainty estimates, *Bull. Amer. Meteor. Soc.*, *90*, 645–656.

Bourras, D. (2006), Comparison of Five Satellite-Derived Latent Heat Flux Products to Moored Buoy Data, *Journal of Climate*, *19*, 6291–6313.

Bradley, E. F., P. A. Coppin, and J. S. Godfrey (1991), Measurement of sensible and latent heat flux in the western equatorial Pacific Ocean, *J. Geophys. Res.*, *96*, 3375–3389.

Bradley, E. F., C. W. Fairall, J. E. Hare, and A. A. Grachev (2000), An Old and Improved Bulk Algorithm for Air-sea Fluxes: COARE 2.6 A, in *Preprints of 14th Symp. on Boundary Layers and Turbulence, Aspen, CO, Am. Meteorol. Soc, 294-296*.

Bretherton, C., M. Widmann, V. P. Dymnikov, J. M. Wallace, and I. Bladé (1999), The Effective Number of Spatial Degrees of Freedom of a Time-Varying Field, *Journal of Climate*, *12*, 1990–2009.

Brunke, M. A., and X. Zeng (2002), Uncertainties in sea surface turbulent flux algorithms and data sets, *Journal of Geoph*, *5*, 1–21.

Buck, A. L. (1981), New Equations for Computing Vapor Pressure and Enhancement Factor, *J. Appl. Meteorol.*, *20*, 1527–1532.

Bumke, K. (2011), The Expedition of the Research Vessel "Polarstern" to the Antarctic in 2010 (ANT-XXVII/1), *Reports on Polar Research*, *628*, 1–82.

Bumke, K., U. Karger, and L. H. H. Niekamp (1998), Evaporation over the Baltic Sea as an Example of a Semi-Enclosed Sea, *Contr. Atmos. Phys.*, *71*, 249–261.

Burnett, W. C., M. Taniguchi, and J. Oberdorfer (2001), Measurement and significance of the direct discharge of groundwater into the coastal zone, *J. Sea Res.*, *46*, 109–116.

Businger, J. A., J. C. Wyngaard, and E. F. Bradley (1971), Flux profile relatrelation in the atmospheric boundary layer, *J. Atmos. Sci.*, *28*, 181–189.

Casey, K. S. (2004), Global AVHRR 4 km SST for 1985-2001, Pathfinder V5.0, *Tech. rep.*, NODC/RSMAS (NOAA National Oceanographic Data Center, Silver Spring, Maryland).

Chang, H., and R. L. Grossman (1999), Evaluation of bulk surface flux algorithms for light wind conditions using data from the Coupled Ocean-Atmosphere Reponse Experiment (COARE, *Q.J.R. Meteorol. Soc.*, *125*, 1551–1588.

Charnock, H. (1955), Wind stress on a water surface, *Q.J.R. Meteorol. Soc.*, *81*, 639.

Chelton, D. B. (1983), Effects of sampling errors in statistical estimation, *Deep Sea Res.*, *30A*, 1083–1103.

Chou, S., E. Nelkin, J. Ardizzone, R. M. Atlas, and C. Shie (2003), Surface Turbulent Heat and Momentum Fluxes over Global oceans Based on the Goddard Satellite Retrievals, Version 2 (GSSTF2), *Journal of Climate*, *16*, 3256–3273.

Chou, S., E. Nelkin, J. Ardizzone, and R. M. Atlas (2004), A Comparison of Latent Heat Fluxes over Global Oceans for Four Flux Products, *Journal of Climate*, *17*, 3973–3989.

Courtier, P., J. Thépaut, and A. Hollingsworth (1994), A strategy for operational implementation of 4D-Var, using an incremental approach, *Q. J. R. Meteorol. Soc.*, *120*, 1367–1388.

Curry, J. A., et al. (2004), SEAFLUX, *Bull. Amer. Meteor. Soc.*, *85*, 409–424.

da Silva, A., A. C. Young, and S. Levitus (1994), *Algorithms and Procedures. Vol. 1, Atlas of Surface Marine Data 1994*, NOAA Atlas NESDIS 6, 83 pp.

Dee, D. P., et al. (2011), The ERA-Interim reanalysis: configuration and performance of the data assimilation system, *Q. J. R. Meteorol. Soc.*, *137*, 553–597.

Douville, H., J.-F. Mahfouf, P. Viterbo, and S. Saarinen (1998), The ECMWF surface analysis: Diagnostics and prospects, *Tech. rep.*, Tech. Memo. No. 258. ECMWF, Reading, UK.

Drennan, W. M., K. K. Kahma, and M. A. Donelan (1999), On momentum flux and velocity spectra over waves, *Boundary-Layer Meteorol.*, *92*, 489–515.

Dyer, A. J. (1967), The turbulent transport of heat and water vapour in an unstable atmosphere, *Quart.*, *93*, 501–508.

Dyer, A. J. (1974), A review of flux-profile Relationships, *Bound.-Layer*, *7*, 363–372.

ECMWF (2006), IFS Documentation (Cy31r1) - Part IV: Physical Processes, *Tech. rep.*, ECMWF, Reading, UK.

Edson, J. B., C. W. Fairall, P. G. Mestayer, and S. E. Larsen (1991), A study of the inertial-dissipation method for computing air-sea fluxes, *J. Geophys. Res.*, *96*, 10,689–10,711.

El Naggar, S. E. D., and A. Macke (2010), The Expedition of the Research Vessel "Polarstern" to the Antarctic in 2009 in (ANT-XXVI/1), *Reports on Polar Research*, *614*, 1–79.

Fahrbach, E., and D. Gerdes (1997), The expedition ANTARKTIS XIII/4-5 of the research vessel "Polarstern" in 1996, *Reports on Polar Research*, *239*, 1–126.

Fairall, C., E. F. Bradley, J. E. Hare, A. A. Grachev, and J. B. Edson (2003), Bulk parameterization of Air-sea Fluxes: Updates and Verification for the COARE Algorithm, *J. Climate*, *16*, 571–591.

Fairall, C. W., E. F. Bradley, D. P. Rogers, J. B. Edson, and G. S. Young (1996), Bulk Parameterization of Air-sea Fluxes for Tropical Ocean-Global Atmosphere Coupled-Ocean Atmosphere Response Experiment, *J. Geophys. Res.-Oceans*, *101*, 3747–3764.

Foken, T. (2008), *Micrometeorology*, Springer-Verlag, Berlin.

Fütterer, D. (1998), The expedition ANTARKTIS-XIV/4 of RV "Polarstern" in 1997, *Reports on Polar Research*, *259*, 1–39.

Garratt, J. R. (1992), *The Atmospheric Boundary Layer*, Cambridge University Press, Cambridge, UK.

Gilhousen, D. (1987), A field evauluation of NCBC moored buoy winds, *J. Atmos. Ocean. Technol.*, *4*, 94–104.

Grachev, A., and C. W. Fairall (1997), Dependence of the Monin-Obukhov satbility parameter on the bulk Richardson number over the ocean, *J. Appl. Meteor.*, *36*, 406–414.

Grachev, A. A., C. W. Fairall, and E. F. Bradley (2000), Convective profile constants revisited, *Boundary Layer Meteorology*, *94*, 495–515.

Graßl, H., V. Jost, R. Kumar, J. Schulz, P. Bauer, and P. Schluessel (2000), The Hamburg Ocean-Atmospherte Parameters and Fluxes from Satellite Data (HOAPS): A Climatological Atlas of Satellite-Derived Air-Sea-Interaction Parameters over the Oceans, *Tech. rep.*, Max-Planck-Institut für Meteorologie, Hamburg, Report No. 312.

Grima, N., A. Bentamy, K. Katsaros, Y. Quilfen, P. Delecluse, and C. Levy (1999), Sensitivity of an oceanic general circulation model forced by satellite wind stress fields, *J. Geophys. Res.*, *104*, 7967–7989.

Hare, J. E., P. O. G. Persson, C. W. Fairall, and J. B. Edson (1999), Behavior of Charnocks relationship for high wind conditions, in *Preprints of 13th Symp. on Boundary Layers and Turbulence, Dallas, TX, Amer. Meteor. Soc., 252-255*.

Hasse, L. (1971), The sea surface temperature deviation and the heat flow at the sea-air interface, *Boundary-Layer Meteorology*, *1 (3)*, 368–379.

Hólm, E. V. (2003), Revision of the ECMWF humidity analysis: Construction of a Gaussian control variable, in *Proceedings of the ECMWF/GEWEX Workshop on Humidity Analysis, 8-11 July 2002*.

Hogstrom, U. (1988), Non-dimensional wind and temperature profiles in the atmospheric surface layer: A re-evaluation, *Bound.-Layer Meteor.*, *42*, 55–78.

Hollinger, J., R. Lo, and G. Poe (1987), Special Sensor Microwave/Imager User's Guide, *Tech. rep.*, Navel Research Laboratory, Washington, D.C., USA.

Jokat, W., and H. Oerter (1997), The expedition ANTARKTIS-XII of RV "Polarstern" in 1995 : report of leg ANT-XII/3, *Reports on Polar Research*, *219*, 1–188.

Jokat, W., and H. Oerter (1998), The expedition ANTARKTIS-XIV of RV "Polarstern" in 1997 : report of Leg ANT-XIV/3, *Reports on Polar Research*, *267*, 1–236.

Jost, V., S. Bakan, and K. Fennig (2002), HOAPS- A new satellite-derived freshwater flux climatology, *Meteorologische Zeitschrift*, *11*, 61–70.

Kaallberg, P. (2011), Forecast drift in ERA-Interim, ERA Report Series 10, *Tech. rep.*, ECMWF, Reading, UK.

Kelly, K. A., S. Dickinson, M. J. McPhaden, and G. C. Johnson (2001), Ocean CCurrent Evident in Satellite Wind Data, *Geophysical Research Letters*, *12*, 2469–2472.

Kilpatrick, K. A., G. P. Podestá, and R. Evans (2001), Overview of the NOAA/NASA Advanced Very High Resolution Radiometer Pathfinder Algorithm for Sea Surface Temperature and Associated Matchup Database, *J. Geophys. Res.-Oceans*, *106*, 9179–9197.

Klepp, C., A. Andersson, and S. Bakan (2008), The HOAPS climatology: evaluation of latent heat flux, *Flux News: Newsletter of the WCRP Working Group on Surface Fluxes 5*, *5*, 30–32.

Klepp, C., K. Bumke, S. Bakan, and P. Bauer (2010), Ground Validation of Oceanic Snowfall in Satellite Climatologies during LOFZY, *Tellus A,*, *62*, 469–480.

Komen, G., L. Cavaleri, M. Donelan, K. Hasselmann, and S. H. P. A. E. M. Janssen (1994), *Dynamics and Modelling of Ocean Waves*, Cambridge University Press: Cambridge, UK.

Krasnopolsky, V. M., L. C. Breaker, and W. H. Gemmill (1995), A Neural Network as a Nonlinear Transfer Function Model for Retrieving Surface Wind Speeds from the Special Sensor Microwave Imager, *J. Geophys. Res.-Oceans*, *100*, 11,033–11,045.

Kraus, E. B., and J. A. Businger (1994), *Atmosphere-Ocean Interaction*, Oxfod University Press, UK.

Krause, G. (1996), The expedition ARKTIS-XI/2 of RV "Polarstern" in 1995, *Reports on Polar Research*, *197*, 1–70.

Krause, G. (1998), The expedition ARKTIS-XIII/3 of RV "Polarstern" in 1997, *Reports on Polar Research*, *262*, 1–93.

Kubota, M. K., A. Kano, H. Muramatsu, and H. Tomita (2003), Intercomparison of various surface latent heat flux fields, *J. Climate*, *16*, 670–678.

Large, W. G., and S. Pond (1982), Sensible and latent heat flux pparameterization over the ocean, *J. Phys. Oceanogr.*, *12*, 464–482.

Leith, C. E. (1973), The standard error of time-average estimates of climatic means, *J. Appl. Meteor.*, *12*, 1066–1069.

Lindau, R. (2001), *Climate Atlas of the Atlantic Ocean - Derived From the Comprehensive Ocean Atmosphere Data Set (COADS)*, Springer-Verlag Berlin, 2001.

Liu, J., T. Xiao, and L. Chen (2011), Intercomparison of Air-Sea Heat Fluxes over the Southern Ocean, *Journal of Climate*, *24*, 1198–1211.

Liu, W. T. (1986), Statistical relation between monthly precipitable water and surface-level humidity over global oceans, *Mon. Wea. Rev.*, *114*, 1591–1602.

Liu, W. T., and T. V. Blanc (1984), The Liu, Katsaros, and Businger (1979) bulk atmospheric flux cocomputation iteration program in FORTRAN and BASIC, *Tech. rep.*, NRL Memo. Rep. 5291, Naval Research Laboratory, Washington D.C., USA.

Liu, W. T., K. B. Katsaros, and J. A. Businger (1979), Bulk parameterization of air-sea exchange of heat and water vapor including the molecular constraints at the interface, *J. Atmos. Sci.*, *36*, 1722–1735.

Liu, W. T., A. Zhang, and J. K. B. Bishop (1994), Evaporation and solar irradiance as regulators of sea surface temeprature in annual and interannual changes, *J. Geophys. Res.*, *99*, 12,623–12,638.

Liu, W. T., W. Tang, and P. S. Polito (1998), NASA scatterometer provides global ocean-surface wind fields with more structures than numerical weather prediction, *Geophysical Re*, *2*, 761–764.

Macke, A. (2009), The expedition of the research vessel "Polarstern" to the Antarctic in 2008 (ANT-XXIV/4), *Reports on Polar Research*, *591*, 1–64.

Magnus, G. (1844), Versuche über die Spannkräfte des Wasserdampfs, *Ann. Phys. Chem.*, *61*, 225–247.

Meissner, T., D. Smith, and F. Wentz (2001), A 10 year intercomparison between collocated Special Sensor Microwave Imager oceanic surface wind speed retrievals and global analyses, *J. Geophys. Res.*, *106*, 731–742.

Monahan, A. H. (2006), The probability distribution of sea surface wind speeds. Part II: DatData intercomparison and seasonal variability, *J. Climate*, *19*, 521–534.

Monin, A. S., and A. M. Obukhov (1954), Basic laws of turbulent mixing in the surface layer of the atmosphere, *Tr. Akad. Nauk SSSR Geofiz. Inst.*, *24*, 163–187.

Obukhov, A. M. (1946), Turbulence in an atmosphere with a non- uniform temperature, *Tr. Inst. Teor. Geofiz. Akad. Nauk. SSSR*, *1*, 95–115.

Panofsky, H., and J. A. Dutton (1984), *Atmospheric Turbulence*, Wiley-Interscience, New York.

Paulson, C. A. (1970), The mathematical representation of wind speed and temperature profiles in the unstable atmospheric surface layer, *J. Appl. Meteorol.*, *9*, 857–861.

Quilfen, Y., A. Bentamy, P. Delecluse, K. Katsaros, and N. Grima (2000), Prediction of sea level anomalies using ocean circulation model forced by scatterometer wind and validation using TOPEX/Poseidon data, *IEEE Trans. Geosci. Remote Sens.*, *38*, 1871–1884.

Rachor, E. (1997), Scientific Cruise Report of the Arctic Expedition ARK-XI/1 of RV "POLARSTERN" in 1995, *Reports on Polar Research*, *226*, 1–336.

Rayner, N. A. (2002), *ECMWF ERA-40 Project Report Series, No. 3*, chap. HadISST1 and the Reynolds et al. analysis, pp. 169–176, ECMWF, Shinfield, Reading, UK.

Reynolds, R. W. (1993), Impact of Mount Pinatubo aerosols on satellite-derived sea surface temperatures, *Journal of Climate*, *6*, 768–774.

Reynolds, R. W., and T. M. Smith (1994), Improved global sea surface temperature using optimum interpolation, *J. Clim.*, *7*, 929–948.

Reynolds, R. W., N. A. Rayner, T. M. Smith, D. C. Stokes, and W. Wang (2002), An Improved In Situ and Satellite SST Analysis for Climate, *J. Climate*, *15*, 1609–1625.

Rouault, M., C. J. C. Reason, J. R. E. Lutjeharms, and A. C. M. Beljaars (2003), Underestimation of Latent and Sensible Heat Fluxes above the Agulhas Current in NCEP and ECMWF Analyses, *Journal of Climate*, *16*, 776–782.

Saunders, P. M. (1967), The temperature of the ocean.atmosphere interfacea, *J. Atmos. Sci.*, *24*, 269–273.

Schlüssel, P., and H. Luthardt (1991), SurfaceWind Speeds Over the North Sea from Special Sensor Microwave/Imager (SSM/I) Observations, *J. Geophys. Res.-Oceans*, *96*, 4845–4853.

Schlüssel, P., L. Schanz, and G. Englisch (1995), Retrieval of latent heat flux and long wave irradiance at the sea surface from SSM/I and AVHRR measurements, *Adv. Space Res.*, *16*, 107–115.

Schulz, J., P. Schlüssel, and H. Grassl (1993), Water vapor in the atmospheric boundary layer over oceans from SSM/I measurements, *Int. J. Remote Sens*, *14*, 2773–2789.

Schulz, J., J. Meywerk, S. Ewald, and P. Schlüssel (1997), Evaluation of satellite-derived latent heat fluxes, *Journal of Climate*, *10*, 2782–2795.

Singh, P., and V. P. Singh (2001), *Snow and Glacier Hydrology*, Kluwer Academic Publishers, Belgium.

Smith, S. D. (1988), Coefficients for sea surface wind stress, heat flux, and wind profiles as a function of wind speed and temperature, *J. Geophys*, *93*, 15,467–15,472.

Smith, S. D. (1989), Water vapor flux at the sea surface, *Bound.-Layer Meteor.*, *47*, 277–293.

Snedecor, G. W., W. G., and Cochran (1989), *Statistical Methods, 8th Ed. Ames*, Iowa State Press.

Spindler, M., W. Hagen, and D. Stübing (1998), Scientific cruise report of the Arctic expedition ARK-XIII/1 of RV "Polarstern" in 1997, *Reports on Polar Research*, *296*, 1–80.

Stein, R., and K. Fahl (1997), Scientific cruise report of the Arctic expedition ARK-XIII/2 of RV "Polarstern" in 1997, *Reports on Polar Research*, *255*, 1–235.

Stogryn, A., C. T. Butler, and T. J. Bartolac (1994), Ocean surface wind retrievals from special sensor microwave imager data with neural networks, *J. Geophys. Res.*, *99*, 981–984.

Strehz, A., K. Bumke, and A. Macke (2009), Development and application of collocation software for buoy, ship, and satellite measurements (KollSat), *Tech. rep.*, Geomar (Helmholtz Centre for Ocean Research), Kiel.

Sud, Y. C., and G. K. Walker (1997), Simulation errors associated with the neglect of oceanic salinity in an atmospheric GCM, *Earth Interactions*, *1*, 1–19.

Taylor, P. K., and M. A. Yelland (2001), The dependence of sea surface roughness on the height and steepness of the waves, *J. Phys. Oceanogr.*, *31*, 572–590.

Trenberth, K. E. (1985), Persistence of Daily Geopotential Heights over the Southern Hemisphere, *Monthly Weather*, *113*, 38–53.

Trenberth, K. E., J. T. Fasullo, and J. Kiehl (2009), Earth's Global Energy Budget, *Bulletin of American Meteorological Society*, *90*, 311–323.

Uppala, S. M., et al. (2005), The ERA-40 re-analysis, *Quart. J. R. Meteorol. Soc.*, *131*, 2961–3012.

Walton, C. C., W. G. Pichel, J. F. Sapper, and D. A. May (1998a), The development and operational application of non-linear algorithms for the measurement of sea surface temperatures with the NOAA polar-orbiting environmental satellites, *J. Geophys. Res.*, *103*, 27,999–28,012.

Webster, P. J., and R. Lukas (1992), TOGA COARE: The coupled ocean atmopshere response experiment, *Bull. Am. Meteorol. Soc.*, *73*, 1377–1416.

Wells, N., and S. King-Hele (1990), Parametrization of tropical ocean heat flux, *Q. J. Roy. Meteor. Soc.*, *116*, 1213–1224.

Wentz, F. J. (1991), Users Manual for SSM/I Antenna Temperature Tapes Revision 1, *Tech. rep.*, Technical Report 120191, Remote Sensing Systems, Santa Rosa, California.

Wentz, F. J. (1997), A well-calibrated ocean algorithm for Special Sensor Microwave/Imager, *J. Geophys. Res.*, *102*, 8703–8718.

Winterfeldt, J., A. Andersson, C. Klepp, S. Bakan, and R. Weisse (2010), Comparison of HOAPS, QuikSCAT, and Buoy Wind Speed in the Eastern North Atlantic and the North Sea, *IEEE Transactions on Geoscience and*, *48*, 338–348.

Woodruff, S. D. (1987), A comprehensive ocean atmosphere data set, *Bulletin of the American Meteorological Society*, *68*, 1239–1250.

Wyngaard, J. C., and O. R. Coté (1990), Scalar ffluxes in the planetray boundary layer: Theory, modeling, and measurement., *Boundary*, *50*, 49–75.

Young, G., D. V. Ledvina, and C. W. Fairall (1992), Influence of precipitating convection on the surface energy budget observed during a Tropical Ocean Global Atmosphere pilot cruise in the tropical western Pacific Ocean, *J GJ. Geophys.*, *97*, 9595–9603.

Yu, L., Z. Zhang, S. Zhong, M. Zhou, Z. Gao, H. Wu, and B. Sun (2011), An inter-comparison of six latent and senisble heat flux prodcuts over the Southern Ocean, *Polar Research*, *30*, 1–27.

Zeng, X., M. Zhao, and R. E. Dickinson (1998), Intercomparison of bulk aerodynamic algorithms for the computation of sea surface fluxes using TOGA COARE and TAO data, *Journal of Climate*, *11*, 2628–2644.

Zenk, W., and S. E. D. E. Naggar (2010), The expedition of the research vessel "Polarstern" to the Antarctic in 2009 (ANT-XXV/5), *Reports on Polar Research*, *603*, 1–62.

Zhang, G. J., and M. J. McPhaden (1995), The relationship between sea surface temeperature and latent heat flux in the equatorial Pacific, *Jounal of Climate*, *8*, 589–605.

Appendix

Atlantic maps within *Section 4* solely focus on the distribution of HOAPS-based LHF, $\vec{u}$, q_a, and respective biases to Oceanet data. Owing to the fact that the ERA-Interim reanalysis also serves as a validation data source to HOAPS within this work, the following five figures illustrate complementary material involving Oceanet and ERA records. The pictured maps comprise two-dimensional parameter distributions of both Oceanet and ERA (*A. 1 - A. 3*) as well as resulting biases when comparing ERA- to HOAPS-based output (*A. 4 - A. 5*).

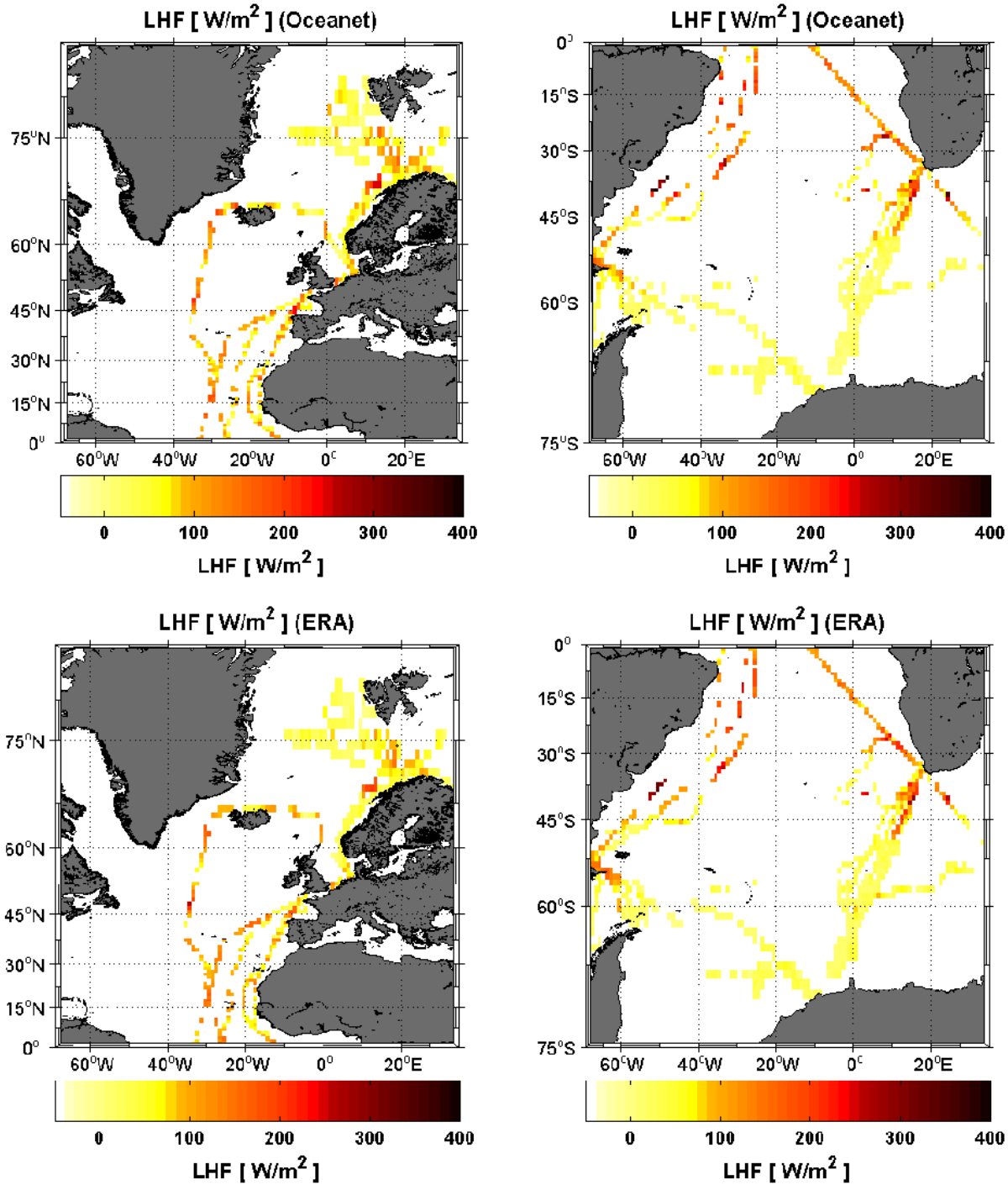

A. 1: As in *Fig. 4.5*, but illustrating mean Oceanet- (**top**) and ERA-based LHF (**bottom**).

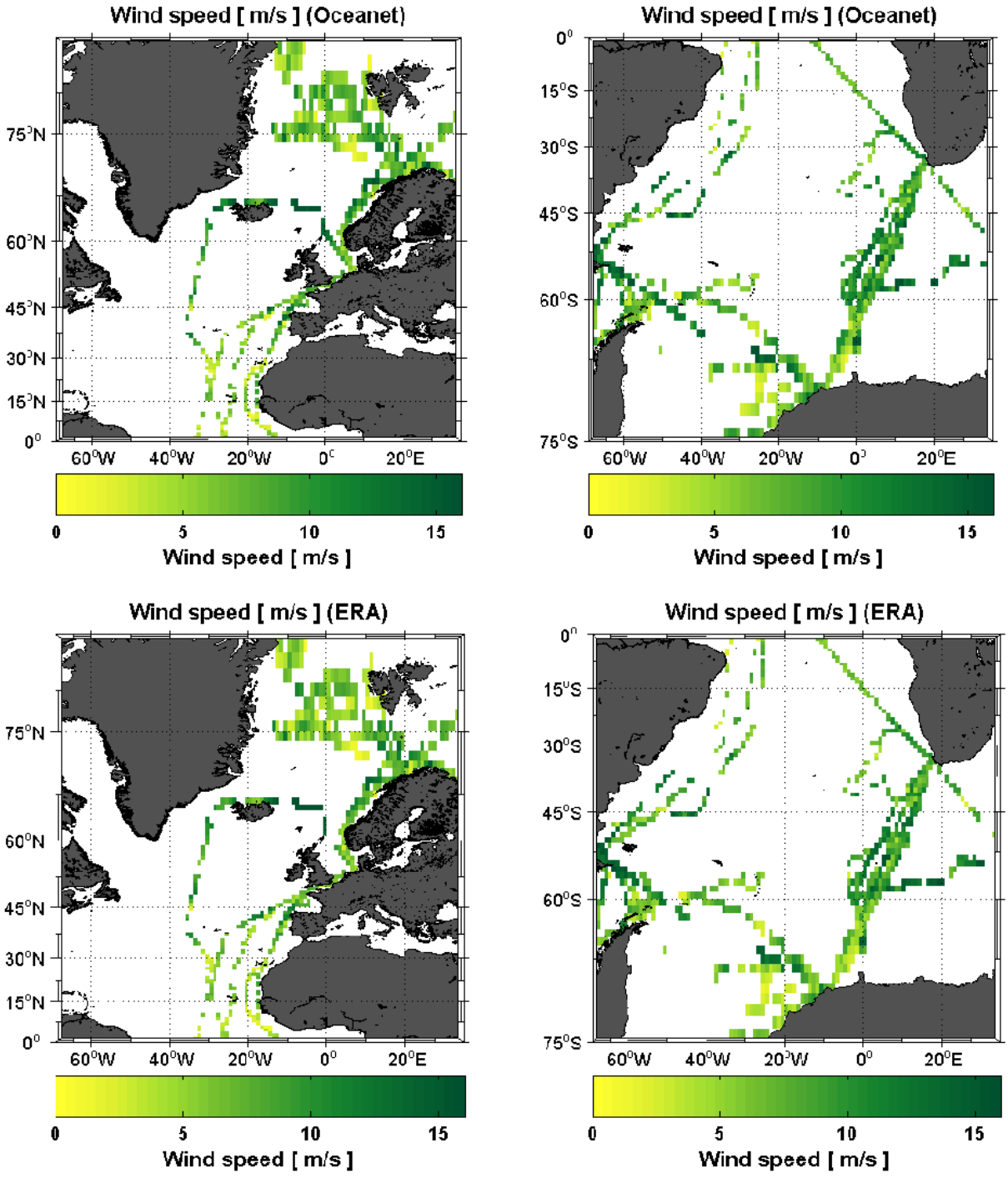

A. 2: As in *Fig. 4.9*, but illustrating mean Oceanet- (**top**) and ERA-based $\vec{u}$ (**bottom**).

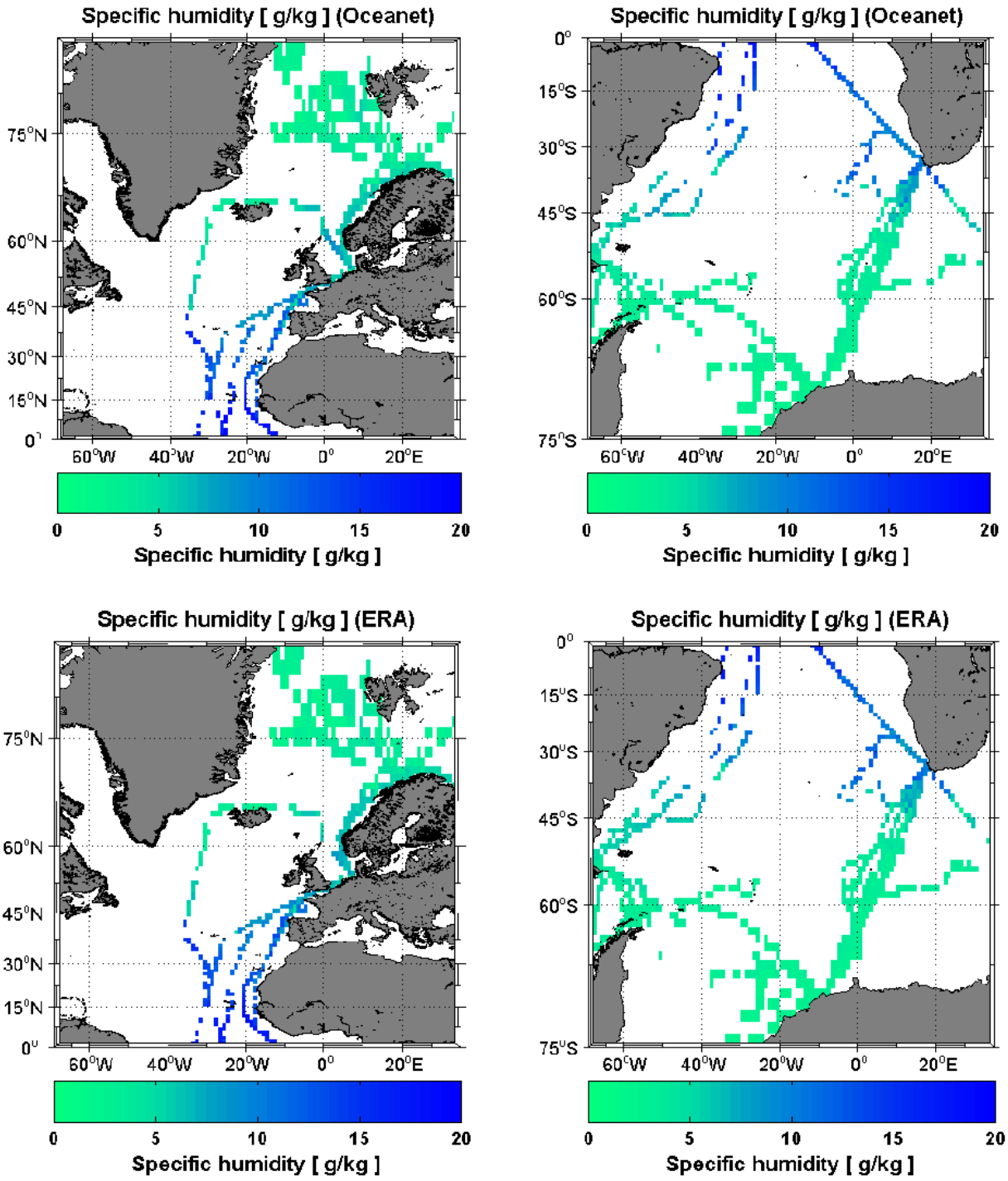

A. 3: As in *Fig. 4.13*, but illustrating mean Oceanet- (**top**) and ERA-based q_a (**bottom**).

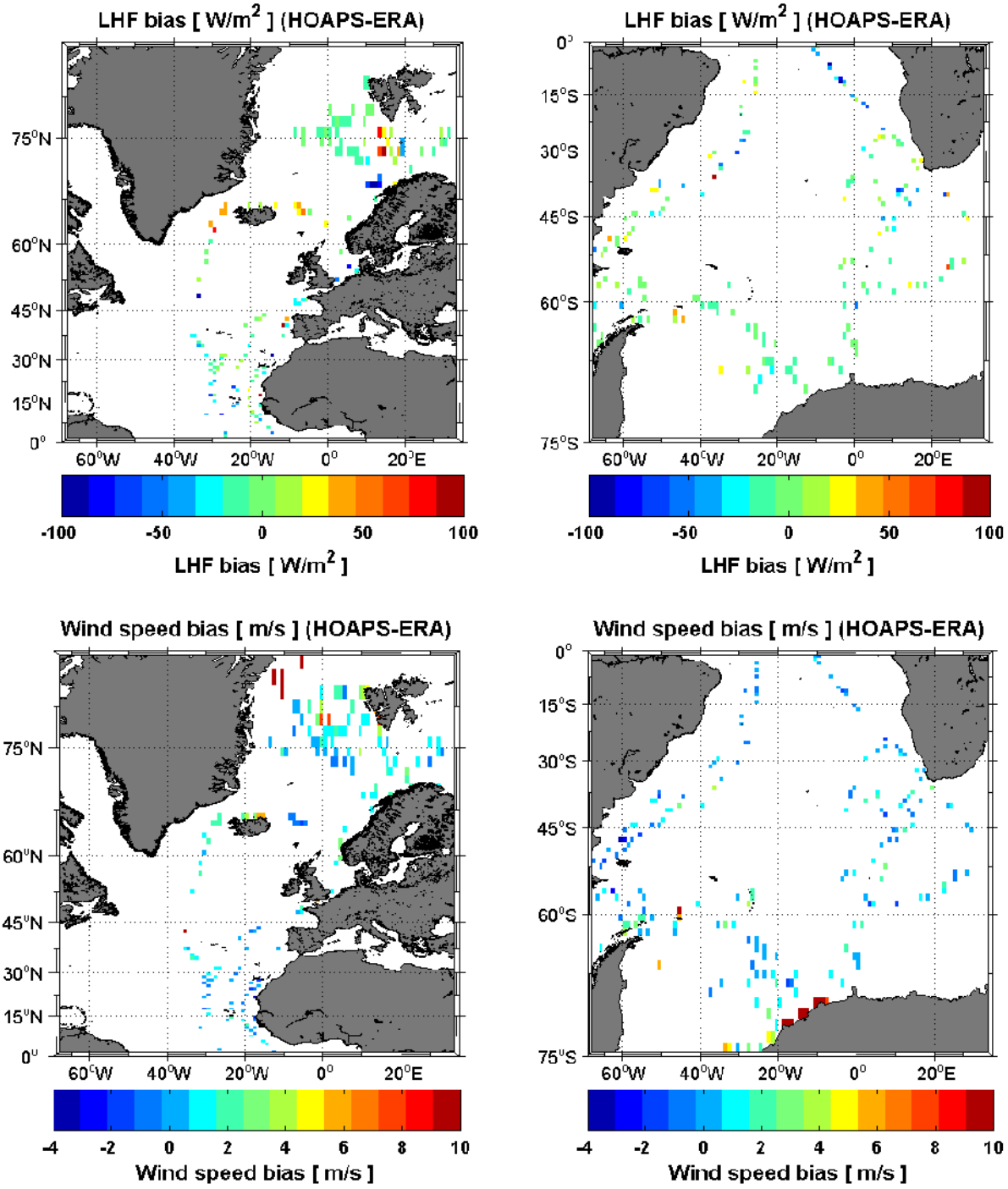

A. 4: As in *Fig. 4.5* (bottom) and *Fig. 4.9* (bottom), but illustrating significant (at the 95% level) biases between ERA- and HOAPS-based LHF (**top**) and $\vec{u}$ (**bottom**).

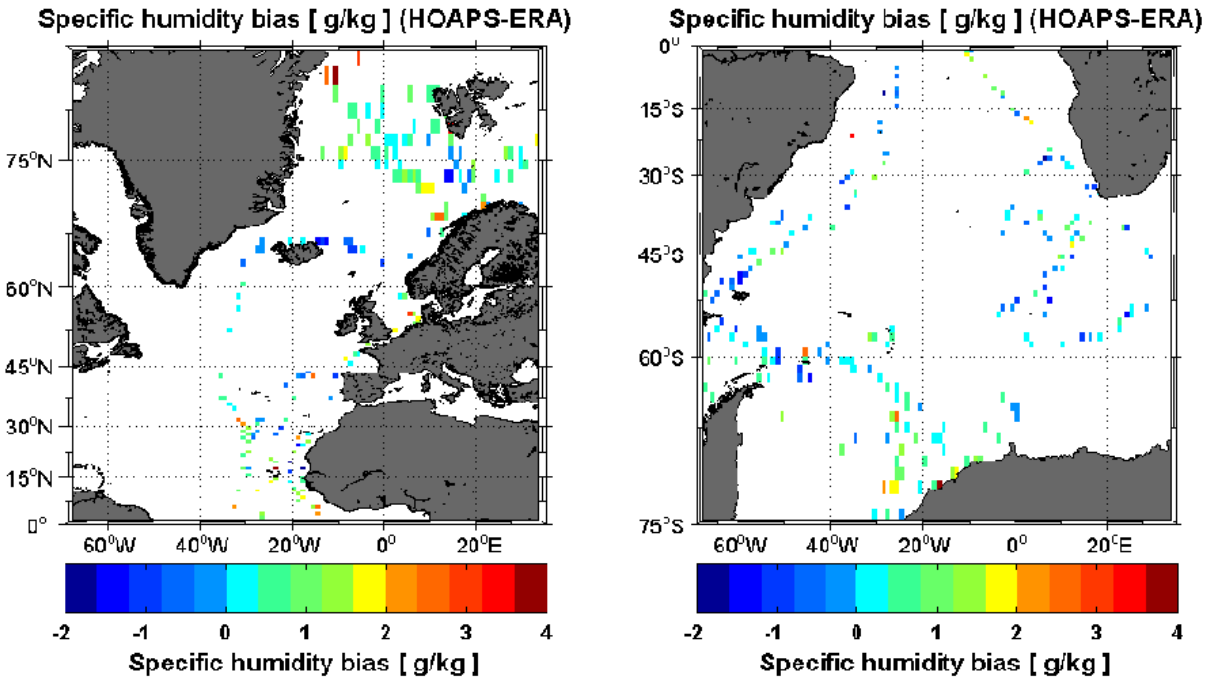

A. 5: As in *Fig. 4.13* (bottom), but illustrating significant (at the 95% level) biases between ERA- and HOAPS-based q_a.

Erklärung

Ich versichere, dass ich die Arbeit selbstständig verfasst und keine anderen als die angegebenen Hilfsmittel benutzt habe. Weiterhin versichere ich, dass diese Arbeit noch nicht als Abschlussarbeit an anderer Stelle vorgelegen hat.

Die eingereichte schriftliche Fassung entspricht der auf dem elektronischen Speichermedium (Name der Datei: 838010).

Ich erkläre mich damit einverstanden, dass ein Exemplar der Abschlussarbeit der Institutsbibliothek zur Verfügung gestellt wird und stimme einer Veröffentlichung der Arbeit zu.

Kiel, den 29.07.2013

_____

Julian Kinzel